Naval Information Warfare Center
PACIFIC

# UAV Urban Channels at 5 GHz Part II: Patch Antenna

**Michael Daly**
**Jeffery Allen**
**John Meloling**

**NIWC Pacific**

**27-Dec-2021**



Naval Information Warfare Center Pacific (NIWC Pacific)
San Diego, CA 92152-5001

# APPROVALS

ALLEN.JEFFERY.C.1231835268

Digitally signed by ALLEN.JEFFERY.C.1231835268
Date: 2022.03.01 07:50:37 -08'00'

DALY.MICHAEL.PATRICK.1394627689

Digitally signed by DALY.MICHAEL.PATRICK.1394627689
Date: 2022.03.01 08:08:43 -08'00'

MCGEE.JODI.B.1050846861

Digitally signed by MCGEE.JODI.B.1050846861
Date: 2022.03.02 17:04:55 -08'00'

# EXECUTIVE SUMMARY

This report is the second in a series *simulating* UAV wireless relays supporting small-unit mobile ground forces deployed in a 3-D digital city. Both reports employ the *Coyote* as the simulated UAV platform but use different antennas on the UAV. The first report put a bottom-mounted *whip* antenna establishing a baseline performance at 500 MHz. This second report employs a bottom-mounted *patch* antenna at 5 GHz. Both reports show the UAV relaying between two street-level nodes has more throughput than the ground-to-ground link. This report shows the UAV loitering over two street-level nodes delivers an average of 332 Mbps at 1 Watt total power while the ground-to-ground link delivers 0.5 Mbps at the same power.

The quality of these simulations depends on the quality of the wireless channel simulations. The wireless channels are simulated by the *Numerical Electromagnetics Code-Basic Scattering Code* (NEC-BSC). This code approximates the 3-D electric field to user-specified accuracy. These wireless channel models encompass the simulated 3-D city, the physics-based multipath propagation, and the electric field patterns around the antennas of both the UAV and the ground units. These coherent, complex-valued channels exhibit non-stationary fading, shadowing, and multipath effects that exceed standard fading models. Given the accuracy of this 3-D solver, the quality of the wireless channel simulations then devolves to the 3-D digital city. At 5 GHz, the wavelength is 60 mm. Simulating an actual city with 60 mm features is impossible. Instead, the 3-D digital city in these reports provides *representative* simulations. The belief is that the relative performance shifts in the simulations approximate relative performance shifts obtained in actual cities. One study that backs this belief is [18].

Although both reports assign specific antennas to the UAV and ground-level receivers at 5 GHz, general observations on the wireless channels of a UAV flying over mobile ground units in a city are possible:

- Antenna patterns affect coverage and fading (Sections 4, 5, 6).
- UAV height and city geometry, particularly building height, governs fading (Sections 5 , 6, 8).
- Channels are well-modeled by the Shadowed Two-Ray Rician fading subject to abrupt switching between fading regimes (Section 5).
- Employing the UAV as a relay simultaneously increases capacity and decreases transmission power, at a cost of employing a spatially varying channel (Section 7, 9).

These observations lead to further extensions of the UAV relay performance. The first extension equips the UAV with multiple antennas and estimates the resulting boost in throughput. Although multiple antennas exploit multipath, the coupling between the antennas on the UAV—*well modeled by NEC-BSC*—sets an upper bound on the multi-antenna gain. Therefore, employing two to four antennas on the UAV with different polarization is the goal of the next report. The second extension tests signal-processing algorithms to handle the multiple fading regimes in the UAV channels while adapting to the spatially varying network of mobile nodes. One component of these algorithms is to learn the periodic fading of a loitering UAV pattern. Another component exploits knowledge of the city's spatial statistics to estimate optimal heights and loitering patterns. The final recommendation is to compare the UAV channels against over-the-air measurements to assess the quality of the simulated performance shifts.

# CONTENTS

**Executive Summary** ..... **iii**

**1. Overview of the UAV Urban Channel Simulations** ..... **1**

**2. Technical Preliminaries** ..... **3**

2.1 Solving the 3-D Wave Equation ..... 3

2.2 Channel Functions ..... 4

2.3 Selected Fading Models ..... 5

**3. The UAV Platform** ..... **10**

3.1 The UAV ..... 10

3.2 Patch Antenna ..... 11

3.3 UAV Antenna Patterns at 5 GHz ..... 12

**4. UAV Coverage to Street-Level Receivers at 5 GHz** ..... **15**

4.1 The Digital City ..... 15

4.2 Coverage as a function of height ..... 18

4.3 Coverage and pattern rotations ..... 21

4.4 Summary ..... 22

**5. UAV Tracks at 5 GHz and 200-MHz Bandwidth** ..... **23**

5.1 Geometry of the Tracks ..... 23

5.2 Track at 50-meter height ..... 24

5.3 Track at 100-meter height ..... 28

5.4 Track at 200-meter height ..... 30

5.5 Summary ..... 33

**6. UAV Spatial Structures at 5 GHz** ..... **34**

6.1 Vertical Slices ..... 34

6.2 Stationary Fading Region ..... 38

6.3 Summary ..... 38

**7. UAV as a Relay** ..... **39**

7.1 Ground-to-Ground Link ..... 39

7.2 Ground-to-UAV Links ..... 40

7.3 A Simple Relay ..... 42

7.4 Summary ..... 43

**8. Path-Loss Modeling** ..... **44**

8.1 COST models ..... 44

8.2 UAV-to-Street models ..... 46

8.3 Summary ..... 49

**9. Circular Tracks** ..... **50**

9.1 Circular Track at 400 meters ..... 50

9.2 No Roll ..... 51

9.3 45° Roll ..... 53
9.4 Summary ..... 54
**10. Extending the UAV Channel Analysis** ..... **55**

# List of Figures


1. UAV relay between street-level radio nodes. ..... 1
2. Edge diffraction [30, Figure 2]. ..... 3
3. Amplitude and phase of Rician fading. ..... 7
4. Amplitude and phase of Two-Ray Rician fading. ..... 7
5. Amplitude and phase of Shadowed Two-Ray Rician fading. ..... 8
6. Amplitude and phase of Two-Ray Shadowed Rician fading. ..... 9
7. Coyote employed for hurricane research; launched from the P-3 in the background [32] (Figure courtesy of NOAA). ..... 10
8. Solid model of the UAV. ..... 11
9. NEC-BSC UAV model and its local $x$-$y$-$z$ coordinate system. ..... 11
10. Electric field components in the local coordinates of the UAV. ..... 12
11. $E_\theta$ pattern for the bottom-mounted patch antenna; zenith angle $\theta$ sweeps from straight up $\theta = 0^\circ$ to straight down $\theta = 180^\circ$. ..... 13
12. $E_\phi$ pattern for the bottom-mounted patch antenna; azimuth angle $\phi$ sweeps from $x$-axis at $\phi = 0^\circ$ toward the $y$-axis at $\phi = 90^\circ$. ..... 13
13. $E_\theta$ pattern for the bottom-mounted patch antenna in the UAV's local coordinate system; Values exceeding $-30$ dB. ..... 14
14. $E_\phi$ pattern for the bottom-mounted patch antenna in the UAV's local coordinate system; Values exceeding $-30$ dB. ..... 14
15. Urban geometry; The "thumbtack" shows the UAV carrying the transmitter hovering 50 meters above the origin. ..... 15
16. Top view of the 3-D simulation; the UAV is located over the origin at varying heights and transmitting into the city. ..... 16
17. Top view showing the street-level coverage area placed two meters above the street. 17
18. Channel coverage at 5 GHz; UAV 50 meters above the origin. ..... 18
19. Channel coverage at 5 GHz; UAV 100 meters above the origin. ..... 19
20. Channel coverage at 5 GHz; UAV 150 meters above the origin. ..... 19
21. Channel coverage at 5 GHz; UAV transmitter is 150 meters above the origin and aligned with the $y$-axis. ..... 20
22. Channel coverage at 5 GHz; UAV transmitter is 200 meters above the origin and rotated $45^\circ$ in azimuth. ..... 21
23. Channel coverage at 5 GHz; UAV transmitter is 200 meters above the origin and rotated $135^\circ$ in azimuth. ..... 22
24. Top view of the UAV's tracks (red line) offset from the $y$-axis by $x_T = 25$ meters; red dot marks the street-level receiver's location. ..... 23
25. The 200-MHz channel; UAV flying the $y$-axis track at 50-meter height broadcasting to the street-level receiver. ..... 24
26. Delay-spread estimate; UAV flying the $y$-axis track at 50-meter height broadcasting to the street-level receiver; Gaussian window with 1-$\mu$s resolution. ..... 25
27. Delay-spread estimate; UAV flying the $y$-axis track at 50-meter height broadcasting to the street-level receiver; Gaussian window with 0.1-$\mu$s resolution. ..... 26
28. Delay-spread estimate; UAV flying the $y$-axis track at 50-meter height broadcasting to the street-level receiver; Gaussian window with 0.01-$\mu$s resolution. ..... 26
29. Narrowband channel at 5-GHz; UAV flying the $y$-axis track at 50-meter height; fading is multi-path interference modulated by shadowing and punctuated by blockage. ..... 27
30. The 200-MHz channel; UAV on the 100-meter track broadcasting to the street-level receiver. ..... 28
31. Delay-spread estimate; UAV flying the $y$-axis track at 100-meter height broadcasting to the street-level receiver; Gaussian window with 0.1-$\mu$s resolution. ..... 29

32. Narrowband channel at 5 GHz; UAV flying the $y$-axis track at 100-meter height; fading is multi-path interference modulated by shadowing and punctuated by blockage. 29
33. The 200-MHz channel; UAV flying the $y$-axis track at 200-meter height broadcasting to the street-level receiver. ..... 30
34. Delay-spread estimate; UAV on the 200-meter track broadcasting to the street-level receiver; Gaussian window with 0.1-$\mu$s resolution. ..... 31
35. Delay-spread estimate; UAV on the 200-meter track broadcasting to the street-level receiver; Gaussian window with 0.01-$\mu$s resolution. ..... 31
36. Narrowband channel of the UAV flying the $y$-axis track at 200-meter height; fading is two-path interference with the deep fade caused by the antenna null. ..... 32
37. Fading on the two strong paths along the 200-meter track. ..... 33
38. Linear shadowing geometry. ..... 34
39. Narrowband channels from the UAV to the street-level receiver; sliced at $x_T = 25$ meters. ..... 35
40. Narrowband UAV channel sliced at $x_T = 25$ m placed in the city; the red stem locates the street-level receiver. ..... 35
41. Narrowband channels from the UAV to the street-level receiver; sliced at $x_T = -50$ meters. ..... 36
42. Narrowband UAV channel sliced at $x_T = -50$ m placed in the city; the red stem locates the street-level receiver. ..... 36
43. Narrowband channels from the UAV to the street-level receiver; sliced at $x_T = -100$ meters. ..... 37
44. Narrowband UAV channel sliced at $x_T = -100$ m placed in the city; the red stem locates the street-level receiver. ..... 37
45. Histograms and Goodness-of-Fit tests of the narrowband UAV channels over the stationary region $200 < y_T < 300$, $100 < z_T < 220$ meters. ..... 38
46. Top view of Node 1 and Node 2. ..... 39
47. Throughput versus power for the Ground-to-Ground link between Node 1 and Node 2; flat urban noise over the 200-MHz bandwidth at 5 GHz. ..... 40
48. Node-to-UAV channels at 5 GHz. ..... 40
49. Weakest Node-to-UAV channels at 5 GHz; UAV flies at 150 m height; aligned with the $y$-axis. ..... 41
50. Histogram of the Weakest Node-to-UAV channels at 5 GHz. ..... 41
51. UAV relay rate at 150 meters altitude; $f_B = 200$ MHz; $p_\Sigma = 10$ W. ..... 42
52. UAV relay rate at 150 meters altitude; $f_B = 200$ MHz; $p_\Sigma = 1$ W. ..... 43
53. COST 231 Walfisch-Ikegami geometry. ..... 45
54. UAV coverage at 5 GHz to street-level receivers as a function of UAV height $z_T = 50$, $150$, and $250$ meters and azimuth $\phi_T = 0°$, $30°$, and $60°$. ..... 46
55. Histograms of the channel gain as a function of UAV height and azimuth; GMM estimates are the solid lines and tabulated on the plots. ..... 47
56. Coverage distributions as a function of UAV height and azimuth; solid lines are the COST 218 Walfisch-Ikegami LoS and non-LoS bounds. ..... 48
57. Circular track and the receiver; the large "thumbtack" marks the location of the street-level receiver. ..... 50
58. Top view of the circular track and the street-level receiver. ..... 51
59. Vertical cross section of the circular track at azimuth $\phi = 180°$ showing the UAV's orientation; $\widehat{\mathbf{x}}$ points out of the paper. ..... 51
60. Channel on the circular track. ..... 52
61. Vertical cross section of the circular track at azimuth $\phi = 180°$ showing the UAV flying with a constant roll of $45°$; $\widehat{\mathbf{x}}$ points out of the paper. ..... 53
62. Channel on the circular track. ..... 53

63. Comparing channels of the UAV flying horizontal to the UAV flying with a $45^{\circ}$ roll..... 54

# List of Tables


1. All second-order reflection and diffraction terms. ..... 4
2. Reflection and diffraction terms to model the electric fields in the 3-D city to 30-dB accuracy. ..... 4
3. Coyote performance and specifications. ..... 10
4. Dielectrics for the 3-D urban simulation at 5 GHz ..... 15
5. Comparing the Ground-to-Ground Channel to the UAV Relay Channel using equal power on up- and down-link; UAV at 150 meters altitude; 5 GHz with a 200-MHz bandwidth. ..... 43
6. COST 231 Hata Parameters. ..... 44
7. COST 231 Walfish-Ikegami Parameters. ..... 45
8. LoS percentage in the GMM. ..... 47
9. LoS power in the GMM ..... 48

# 1. OVERVIEW OF THE UAV URBAN CHANNEL SIMULATIONS

This report simulates ground-to-air wireless channels of a low-flying UAV supporting small-unit mobile ground forces deployed in urban environments. Figure 1 illustrates the UAV relaying between two street-level radios. This report finds that a UAV relay averages 34 dB *less* loss than the ground-to-ground channels between the same street-level radios.

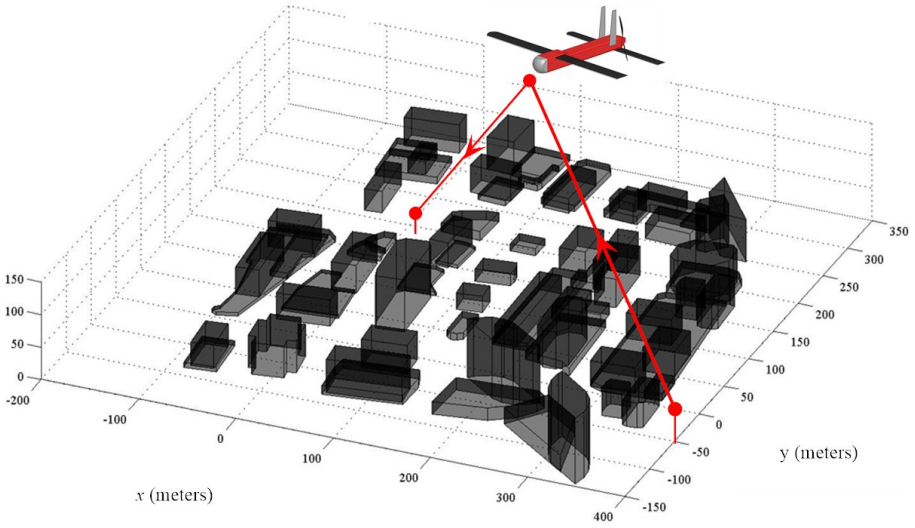


Figure 1. UAV relay between street-level radio nodes.

The UAV relay channel consists of two UAV channels. The UAV channels are measured from the *input terminals* of the UAV's antenna to the *output terminals* of the antennas of the street-level receivers. These channels encompass the UAV's antenna with platform effects, the multipath propagation though the city, and the resulting electric field surrounding the receiver's antenna. The simulations show that the UAV channels are well modeled by multiple *rays* carrying the UAV's signal $s_T(t)$ transmitted from the UAV's location $\mathbf{r}_T$ to the received signal $s_R(t)$ at the street-level receiver located at $\mathbf{r}_R$ as

$$s_R(t) = \sum_{\ell=1}^{L} h_\ell(f_C; \mathbf{r}_T, \mathbf{r}_R) \cdot s_T(t - \tau_\ell), \tag{1}$$

where the $\ell$-th ray *delays* the signal by $\tau_\ell$ and *fades* the signal by $h_\ell(f_C; \mathbf{r}_T, \mathbf{r}_R)$. The multiplication by the fading implies a narrow-band signal at center frequency $f_C$. As the UAV flies through the 3-D space, the time-varying position of the UAV at location $\mathbf{r}_T(t)$ generates time-varying UAV channels:

$$s_R(t) = \sum_{\ell=1}^{L} h_\ell(f_C; \mathbf{r}_T(t), \mathbf{r}_R) \cdot s_T(\tau - \tau_\ell(t)). \tag{2}$$

These time-varying UAV channels are the"objects of discussion" of this report. When these UAV channels form a relay between street-level receivers, these UAV relays increase average throughput is at least ten times ($\times 10$) over ground-level channels in urban noise (Section 7). These simulated gains are limited by the following assumptions:

- Throughput is bounded by the capacity equation,
- Latency is not modeled,
- Interference is not modeled.

Despite these limitations, the simulated gain in the relay channel argues that actual UAV relays will still deliver significant performance over ground-to-ground links. Analysis of throughput as a function of the UAV's channel requires a discussion of UAV, the antennas, the 3-D propagation into the city, and the propagation effects. This analysis is organized as follows:

- Section 2 sets out the technical background: the 3-D propagation code (NEC-BSC), the channel functions, and selected fading models.
- Section 3 describes the UAV, the bottom-mounted patch antenna, and the UAV platform effects.
- Section 4 shows how the UAV "lights" up the city from a fixed position showing the fading caused by the city's geometry and the nulls produced by the patch antenna.
- Section 5 "flies" the UAV along straight-line tracks of varying heights while broadcasting to a fixed, street-level receiver. These simulations show the non-stationary fading along the UAV tracks is caused by the buildings modulating with blockage, shadowing, and delay.
- Section 6 explains the fading along straight-line tracks. By stacking hundreds of these tracks, a vertical "slice" of the channel is produced. These slices show the shadowing and blockage are caused by the city's buildings. As the UAV flies through the blockage patterns, the channel switches across multiple fading regimes.
- Section 7 uses the coverage plots to assess the payoff when the UAV is employed as a relay. When the UAV is loitering over street-level radio nodes, the UAV relay shows substantial throughput over the ground-to-ground link when both systems operate using the transmit power.
- Section 8 undertakes a simple "COST 231" modeling for the UAV flying overhead. The simulations show the COST model bounds the channel gain requiring only rudimentary estimates of the city geometry. These bounds are useful for link budget but cannot model the distribution of the channel gains or the rapid fading.
- Section 9 flies the UAV on a circular track loitering over a street-level radio node. As with the linear tracks, the channel shows heavy blockage and shadowing caused by the city's buildings. The example shows the potential of "loitering" patterns—ground nodes can "learn" this periodic pattern and the switching between fading regimes to boost throughput and reduce RF broadcast power.
- Section 10 summarizes the observations about the UAV channels: how the UAV's antenna pattern determines coverage, how performance is affected by the city's geometry coupled with the UAV's hieght, and the payoff using the UAV as a relay. This section concludes with a collection of tasks supporting network emulation and longer-term tasking assessing the payoffs for UAV channel, especially with respect to stealthy wireless tactical networks.

# 2. TECHNICAL PRELIMINARIES

This report models ground-to-air channels of a low-flying UAV operating over a an urban environment. The first task of channel modeling simulates the UAV's transmissions propagating through the urban environment. This propagation is governed by 3-D wave equation. Section 2.1 reviews a 3-D wave equation solver suitable for kilometer-sized regions. This solver approximates the UAV channels given by Equation 1. The second task of channel modeling extracts the fading of the time-varying channels as the UAV flies over the city from Equation 2. Section 2.2 reviews the formalism of the time-varying channels. The simulated time-varying channels are well-modeled as multi-ray Rician subject to shadowing. Section 2.3 reviews Rician fading and generalizations.

## 2.1 SOLVING THE 3-D WAVE EQUATION

Figure 1 makes explicit that the UAV channels start at the input to the UAV antenna, propagate through the 3-D city, and finish at the output of the receive antenna. The propagation through the 3-D city is governed by the wave equation [20, Chapter 3]. The *Numerical Electromagnetics Code-Basic Scattering Code* (NEC-BSC) computes approximate solutions to the 3-D wave equation in complex environments by reflection and diffraction modeling [29]. The electric field at position $\mathbf{r}$ generated by a transmitter broadcasting at frequency $f$ is the sum of multiple rays interacting with the 3-D environment:

$$\begin{aligned}\mathbf{E}(f;\mathbf{r}) &= \mathbf{E}_{\text{inc}}(f) + \sum_{r\in\mathcal{P}(\mathbf{r})} \mathbf{E}^p(f;\mathbf{q}_r) + \sum_{e\in\mathcal{E}(\mathbf{r})} \mathbf{E}^e(f;\mathbf{q}_e) \\ &+ \sum_{v\in\mathcal{V}(\mathbf{r})} \mathbf{E}^v(f;\mathbf{q}_v) + \text{higher-order terms.} \end{aligned} \tag{3}$$

The *incident* electric field $\mathbf{E}_{\text{inc}}$ is produced by the direct path from the source to position $\mathbf{r}$, provided there is no blockage. The electric fields $\mathbf{E}^p$ denote the *plate reflections*. Each field is generated by a ray traveling from the source, reflecting off a plate at position $\mathbf{q}_r$, and arriving at position $\mathbf{r}$. Each plate reflection models the dielectric of the plate and spreading after reflection. The electric fields $\mathbf{E}^e$ denote the *edge diffractions*. Each field is generated by a ray traveling from the source, diffracting on an edge at position $\mathbf{q}_e$, and arriving at position $\mathbf{r}$. Each edge diffraction models the dielectric of the edge and spreading after diffraction. The edge diffractions correct for discontinuities in the incident and plate-reflected fields. Figure 2 illustrates the diffraction-cone geometry for an edge. The electric fields $\mathbf{E}^v$ denote the *vertex diffractions*. Each field is generated by a ray traveling from the source, diffracting at vertex $\mathbf{q}_v$, and arriving position $\mathbf{r}$. The vertex diffraction terms correct for the discontinuities in the edge-diffracted fields.

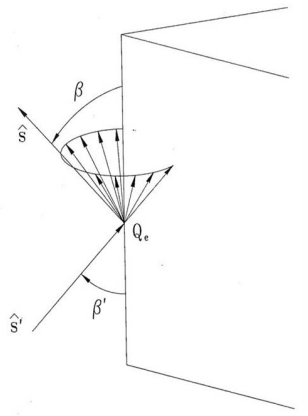


Figure 2. Edge diffraction [30, Figure 2].

Multiple interactions between plates, edges, and vertices are needed for complex environments. Cascading these interactions determine the higher-order interactions. The higher-order terms compensate discontinuities in first-order and other lower-order terms. All the second-order interactions are listed in Table 1.

Table 1. All second-order reflection and diffraction terms.

| | | |
|---|---|---|
| Plate-to-Plate | Edge-to-Plate | Vertex-to-Plate |
| Plate-to-Edge | Edge-to-Edge | Vertex-to-Edge |
| Plate-to-Vertex | Edge-to-vertex | Vertex-to-Vertex |

Third-order terms follow a similar pattern (e.g., Plate-to-Plate-to-Plate, Plate-to-Plate-to-Edge, ...). Complex environments have an infinite number of higher-order interactions. A correct application of NEC-BSC requires that the dominant terms in an environment be determined to guarantee accuracy of the solution. Such a convergence study was undertaken to support the propagation in [18]. Table 2 lists the diffraction terms necessary to approximate the electric field to 30-dB accuracy. The dominant terms were limited to plate and edge interactions.

Table 2. Reflection and diffraction terms to model the electric fields in the 3-D city to 30-dB accuracy.

| Order | Terms |
|---|---|
| 0 | Incident |
| 1 | Plate, Edge |
| 2 | Plate-to-Plate, Edge-to-Plate, Edge-to-Edge |

The reason NEC-BSC propagates using electric field rather than power is the high-quality antenna modeling. These simulations model the UAV's patch antenna to include the effects of the UAV platform. Section 3.3 shows how the UAV platform affects both the vertical and horizontal electric field patterns around the UAV. Consequently, the UAV broadcasts rays through this "antenna+platform" electric field pattern before propagating through the 3-D city and arriving at the receiver's antenna.

The street-level receivers employ a half-wavelength vertical dipole placed two meters above the street. These dipoles intercept the multiple rays arriving with polarization affected by the transmitter's platform and the interactions listed in Table 2. There is no receiver platform—the vertical dipole intercepts the vertical component of the electric field of each incident ray. The complex-valued voltages are coherently summed to model the voltages at the output terminal of the receive antenna that arrive at the same delay (See Equation 3). The coherent sum allows NEC-BSC to model receivers using multiple antennas. Future extensions of this report will assess receivers carrying multiple antennas to exploit polarization and multipath [5] and include receiver platforms effects. However, both this report and the first report compare only the performance shift delivered by *different* antennas carried by the *same* UAV. This comparison eliminates the confounding effects of the receiver platforms from these simulations.

### 2.2 CHANNEL FUNCTIONS

A classic model of the time-varying channel is the *delay spread* function $\{h(t,\tau)\}$ mapping a transmitted signal $s_T(t)$ to a received signal $s_R(t)$ as [11]:

$$s_R(t) = \int_{-\infty}^{\infty} h(t,\tau) s_T(t-\tau) d\tau. \tag{4}$$

A classic model of a delay spread function is adapted from [37, Eq. 14-1-5]:

$$h(t,\tau) = \sum_{\ell=1}^{L} h_\ell(t)\delta(\tau - \tau_\ell). \tag{5}$$

Inserting the delay spread function of Equation 5 into Equation 4 models the received signal $s_R(t)$ as the sum of delayed and faded copies of the transmitted signal $s_T(t)$:

$$s_R(t) = \sum_{\ell=1}^{L} h_\ell(t) s_T(t - \tau_\ell).$$

If the fading processes $\{h_\ell(t)\}$ are wide-sense stationary, uncorrelated, and ergodic [33]:

$$E[|h_\ell(t)|^2] = \lim_{T\to\infty} \frac{1}{T} \int_{-T}^{T} |h_\ell(t)|^2 dt \quad \text{(a.s.)}$$

and the delays $\tau_\ell$ are deterministic, the average power over time in the delay spread function of Equation 5 is the *power-delay profile* [48, page 77]:

$$P_h(\tau) = E[|h(t,\tau)|^2] = \sum_{\ell=1}^{L} E[|h_\ell(t)|^2]\ \delta(\tau - \tau_\ell).$$

This power-delay profile shows the fading power at each delay. If the UAV is moving as in Equation 2, the delay spread function has the form [37, Eq. 14-1-5]:

$$h(t,\tau) = \sum_{\ell=1}^{L} h_\ell(t)\delta(\tau - \tau_\ell(t)). \tag{6}$$

Equation 3 computes each term in this fading model as a function of the UAV's time-varying location $\mathbf{r}_T(t)$: each multpath ray has delay $\tau_\ell(t)$ computable from the ray's length; each fading process $h_\ell(t)$ is computable from the electric field. Averaging the power of the delay spread function of Equation 6 over time produces the *power-delay profile* of the form

$$P_h(\tau) = E[|h(t,\tau)|^2] = \sum_{\ell=1}^{L} E[|h_\ell(t)|^2]\ p_\ell(\tau),$$

where $p_\ell(\tau)$ is the probability density of the random delay $\tau_\ell$, provided the fading processes $\{h_\ell(t)\}$ are uncorrelated, ergodic, and independent of the delay processes $\{\tau_\ell(t)\}$ that also are uncorrelated and ergodic. This power-delay profile shows the fading power spread over the distribution of each delay.

### 2.3 SELECTED FADING MODELS

As the UAV travels along its flight path, the spatially varying channel modulates the transmitted signal. Equation 1 is the narrow-band "multiplicative" or fading noise model. The simulations in the first report and this report show rapid switching between short- and long-term fading leading to the composite fading models.

> **Short-Term Fading [40]:** "[when] the received signal fluctuates deeply in a small local area around the receiver (typically in few wavelengths covered) ... caused by the multipath propagation. In the literature, this small-scale fading has been characterized using the Rayleigh, Rice, Weibull and Nakagami-$m$ distributions [34], [44]."
>
> **Long-Term Fading [40]:** "for displacements of hundred of wavelengths, the received signal suffers slow variations due to the propagation shadowing of the direct path between the transmitter and receiver. These slow variations are the well-known long-term fading or shadowing which have been mainly modeled using the lognormal distribution [42], [49]."
>
> **Composite Fading [38]:** "A composite multipath/shadowing distribution such as Rayleigh-lognormal, Rice-lognormal and Nakagami-lognormal distributions can be expressed as the product of a multipath fading [random variable] and a shadowing [random variable] [45, page 33] ....

Composite fading is undergoing rapid development with many combinations of products and associated estimators [24]:

> "The short-term fading can be observed within short distance with few wavelengths such as $\kappa$-$\mu$, $\eta$-$\mu$, $\alpha$-$\mu$, Rayleigh, Nakagami-$m$ and Weibull, and the long-term fading is usually described by lognormal distribution which can be represented as $\alpha$-$\mu$ distribution (includes special cases e.g. gamma, Nakagami-$m$, negative exponential, Weibull, one-sided Gaussian and Rayleigh)."

These simulations show Shadowed Two-Ray Rician is a credible fading model [28], [39] [41], [19], [9], [10]. Examples of Rician fading, Two-Ray Rician Fading, Shadowed Two-Ray Rician Fading, and Two-Ray Shadowed Rician Fading are presented next.

The definition of Rician fading is *adapted* from Stüber as the complex-valued Gaussian process [48, page 51]

$$h(t) = e^{j2\pi f_D t} \left\{ s_{\mathsf{LOS}} + g(t) \right\},$$

where $f_D$ denotes the Doppler shift, $s_{\mathsf{LOS}}$ is the complex-valued *specular component* and $\{g(t)\}$ is the *diffuse component* consisting of the sum of two real-valued, zero-mean, independent, stationary Gaussian processes $\{g_I(t)\}$ and $\{g_Q(t)\}$ with common variance $\sigma^2$:

$$g(t) = g_I(t) + j g_Q(t).$$

The average power of this Rician fading process $\{h(t)\}$ is the sum of the specular power and the diffuse power [48, page 53]

$$E[|h(t)|^2] = |s_{\mathsf{LOS}}|^2 + 2\sigma^2$$

The Rician $K$ factor is ratio of the specular power to the diffuse power [48, page 53]

$$K = 10 \cdot \log_{10} \left( \frac{|s_{\mathsf{LOS}}|^2}{2\sigma^2} \right) \quad \text{[dB]}.$$

The probability distribution of $\{|h(t)|\}$ is [37, Eq. 2-1-141], [48, Eq. 2.45]

$$p_{|h|}(r) = \frac{r}{\sigma^2} \exp\left( -\frac{r^2 + s^2}{2\sigma^2} \right) I_0 \left( \frac{rs}{\sigma^2} \right),$$

where $I_0(r)$ denotes the modified Bessel function of the first kind.

**Example 1 (Rician Fading)** *Figure 3 shows the amplitude and phase of simulated Rician fading* $\{h(t)\}$ *with* $K = 10$ dB *and* $f_D = 3$ Hz. *The diffuse component* $\{g(t)\}$ *is modeled with the power spectrum [51]:*

$$P_{gg}(f) = \frac{2\sigma^2}{f_N \sqrt{2\pi}} \exp\left( -\frac{f^2}{2 f_N^2} \right), \tag{7}$$

*where* $f_N$ *is the* RMS bandwidth *[3].*

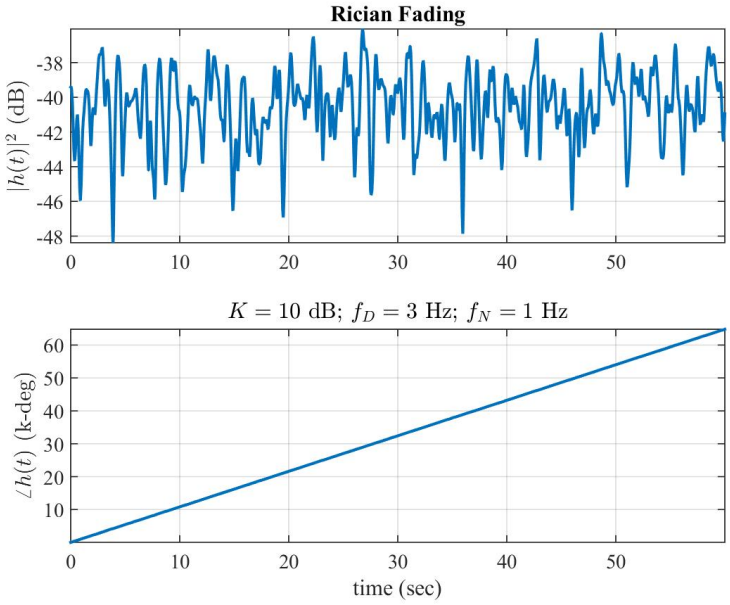


Figure 3. Amplitude and phase of Rician fading.

Rician fading appears in these simulations as a strong ray accompanied by a collection of weaker rays. The fading observed in the simulations is similar to Two-Ray Rician fading [37].

**Example 2 (Two-Ray Rician Fading)** *Figure 4 shows the amplitude and phase of simulated Two-Ray Rician fading* $h(t) = h_1(t) + h_2(t)$. *Because both Rician* $K$ *factors exceed 10 dB, their specular components dominate and the interference pattern with a period of 2 seconds is caused by the difference of 0.5 Hertz between the Doppler shifts.*

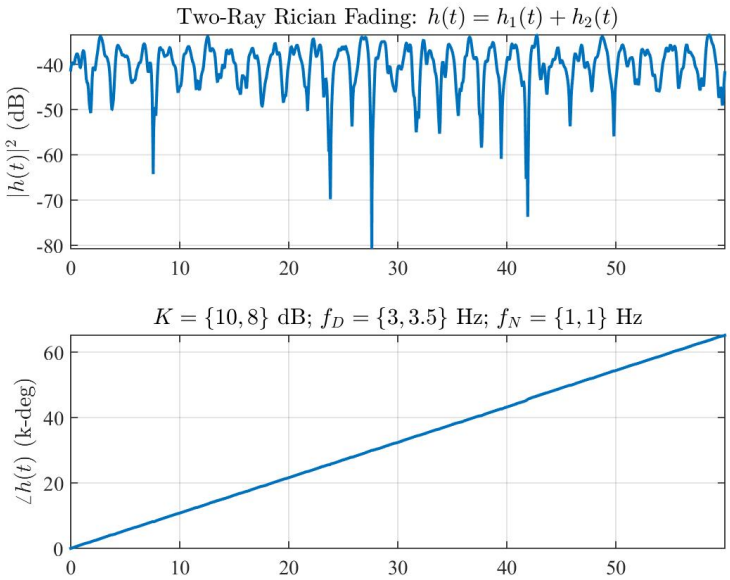


Figure 4. Amplitude and phase of Two-Ray Rician fading.

Fluctuating Two-Ray (FTR) fading generalizes Rician fading by modulating the *specular* components of two Rician processes with the same shadowing. This report *adapts* FTR fading by shadowing two *Rician* processes as [41, Eq. 2]:

$$h_{\mathsf{FTR}}(t) = \zeta(t)\{h_1(t) + h_2(t)\},$$

where $\{\zeta(t)\}$ is a slowly varying Nakagami-$m$ random process with $E[|\zeta(t)|^2] = 1$ that is independent from the Rician processes.

**Example 3 (Shadowed Two-Ray Rician Fading)** *Figure 5 shows the amplitude and phase of Shadowed Two-Ray Rician fading. The Rician fading processes $\{h_1(t)\}$ and $\{h_2(t)\}$ are realized using the parameters of Example 2. Their sum is modulated by the Nakagami fading $\{\zeta(t)\}$ with $m = 2$.*

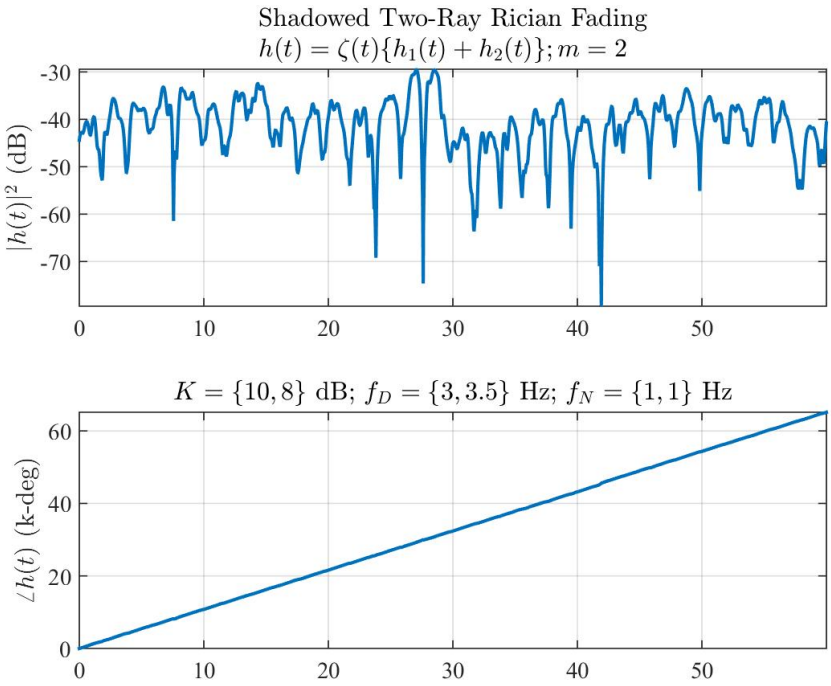


Figure 5. Amplitude and phase of Shadowed Two-Ray Rician fading.

This unity gain of the shadowing process $\{\zeta(t)\}$ and their independence preserves the second-order statistics of the Rician fading processes and their $K$ factors:

$$\begin{aligned} E[|\zeta(t)h_1(t)|^2] &= E[|h_1(t)|^2] = s_1^2 + \sigma_1^2, \\ E[|\zeta(t)h_2(t)|^2] &= E[|h_2(t)|^2] = s_2^2 + \sigma_2^2. \end{aligned}$$

The simulations show the shadowing modulating the Rician processes is caused by different ray bundles arriving at the UAV with relatively small angular separation between the ray bundles. The small angular separation means that buildings could simultaneously shadow the rays or that both rays could arrive at an antenna null.

Fluctuating Beckmann (FB) fading generalizes Rician fading by fluctuating the power of each specular component of multiple Rician processes [39]. The final example of this section *adapts* FB fading by shadowing two *Rician* processes as

$$h(t) = \zeta_1(t)h_1(t) + \zeta_2(t)h_2(t),$$

where $\{\zeta_1(t)\}$ and $\{\zeta_2(t)\}$ are slowly varying Nakagami processes with unit second moment, independent from the Rician processes, and independent from each other.

**Example 4 (Two-Ray Shadowed Rician Fading)** *Figure 5 shows the amplitude and phase of Two-Ray Shadowed Rician fading. The Rician fading processes* $\{h_1(t)\}$ *and* $\{h_2(t)\}$ *are from Example 2. Each process is modulated by Nakagami fading* $\{\zeta_1(t)\}$ *with* $m_1 = 2$ *and* $\{\zeta_2(t)\}$ *with* $m_2 = 0.5$*, respectively. The resulting fading shows most the interference pattern caused by the Doppler shift as in Example 2. The smaller* $m_2$ *causes relatively greater shadowing variations. This boost the weaker fading process* $\{h_2(t)\}$ *and causes some "filling" of the nulls.*

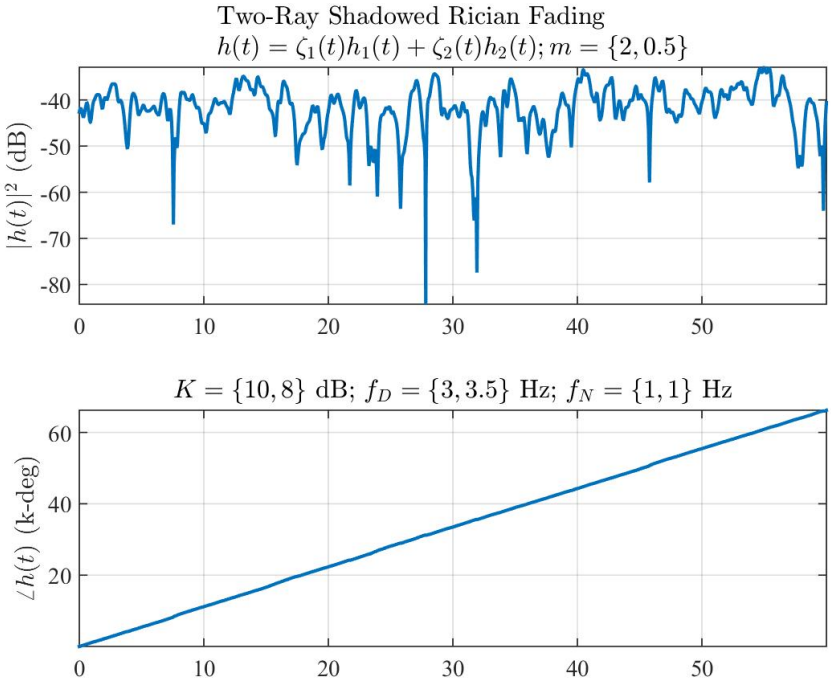


Figure 6. Amplitude and phase of Two-Ray Shadowed Rician fading.

The value of these examples is to recognize the fading produced in the simulations. The two-ray interference pattern is the most recognizable and is caused by ray bundles arriving at the UAV from different angles. Omitted from these examples are the additional effects on the fading caused by the antenna and blocking by buildings. Examples of Shadowed Two-Ray Rician fading and the additional effects are found in Section 5.

# 3. THE UAV PLATFORM

Both this report and the first report employ the *Coyote* as the UAV platform [17]—only the antennas and operating frequencies are different. These two reports demonstrate swapping out the antenna is straightforward. The payoff is that relative performance shifts delivered by the different antenna systems can be compared on the same platform operating over the same urban environment. Section 3.1 details the *Coyote*. Section 3.2 describes the patch antenna that is mounted flush on the underside of the fuselage. Section 3.3 shows the vertical and horizontal antenna patterns that are shaped by the UAV platform. The antenna patterns are placed in the 3-D digital city and carry the UAV's broadcasts to the street-level receivers as computed by NEC-BSC. The deep nulls of these patterns verify that the UAV is correctly placed and oriented in the 3-D simulations.

## 3.1 THE UAV

The Coyote was developed by BAE under an ONR grant for Intelligence, Surveillance, and Reconnaissance (ISR) operations. The typical ISR payloads are Electro-Optical (EO) or Infra-Red (IR) cameras and data transmitters. Figure 7 shows a Coyote used for weather research and the P-3 aircraft that serves as the launch platform. Table 3 details the standard Coyote performance bounds.

Figure 7. Coyote employed for hurricane research; launched from the P-3 in the background [32] (Figure courtesy of NOAA).

Table 3. Coyote performance and specifications.

| Specifications | Performance |
|---|---|
| **Endurance** | 90 minutes ISR collection |
| **Max Altitude** | 20,000 ft AGL |
| **Speed** | 60–85 knots |
| **Weight** | 12–14 pounds |
| **Wing Span** | 58 inches |
| **Length** | 3 feet (approximately) |
| **Control** | line-of-sight radio link (VHF or UHF) |

### 3.2 PATCH ANTENNA

Figure 8 is a solid view of the Coyote model. This model is the basis for the NEC-BSC model.

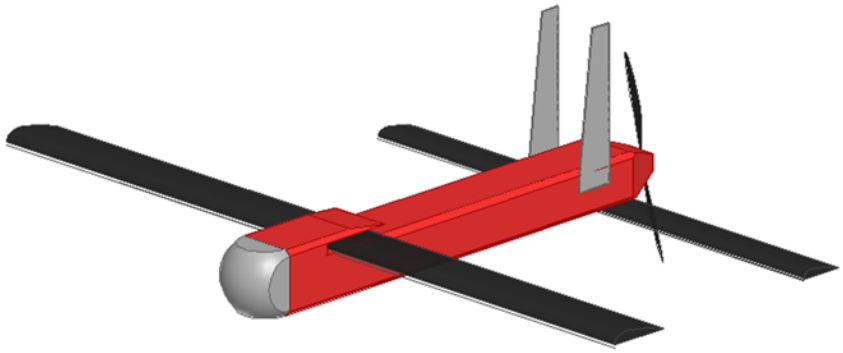

Figure 8. Solid model of the UAV.

Figure 9 shows the Coyote modeled in NEC-BSC. The figure shows the local coordinate system that moves with the UAV. This local coordinate system orients the vehicle in the NEC-BSC simulations. The patch antenna (not shown) is mounted on the underside of the UAV where the $z$-axis intercepts the fuselage. The patch antenna is $0.2'' \times 0.2''$ (inches) and flush with the underside. The next section shows how the UAV platform modifies the free-space pattern of the patch antenna.

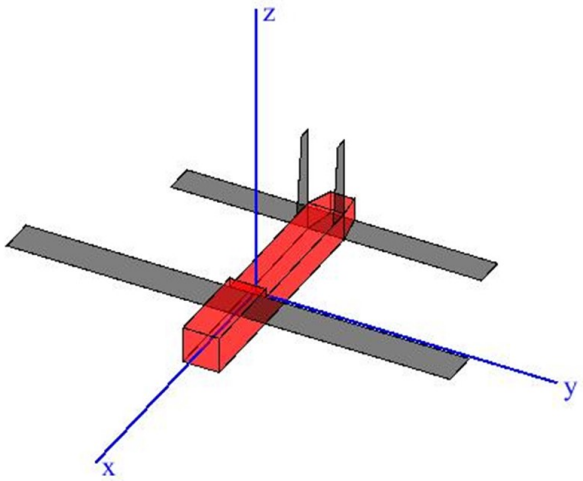


Figure 9. NEC-BSC UAV model and its local $x$-$y$-$z$ coordinate system.

### 3.3 UAV ANTENNA PATTERNS AT 5 GHZ

Figure 10 shows the *azimuth* angle $\phi$ and the *zenith* angle $\theta$ in the local coordinate system on the UAV. The azimuth $\phi$ sweeps from the $x$-axis toward the $y$-axis. The zenith $\theta$ sweeps from the $z$-axis toward the $x$-$y$ plane. If this local coordinate system is aligned with the coordinate system of the simulation, $\theta = 90^\circ$ points in the horizontal and $\theta = 180^\circ$ points straight down. The figure also shows the tangents to these angles that define the electric field of the antenna: $E_\phi$ is the horizontal component electric field; $E_\theta$ is the vertical component of the electric field.

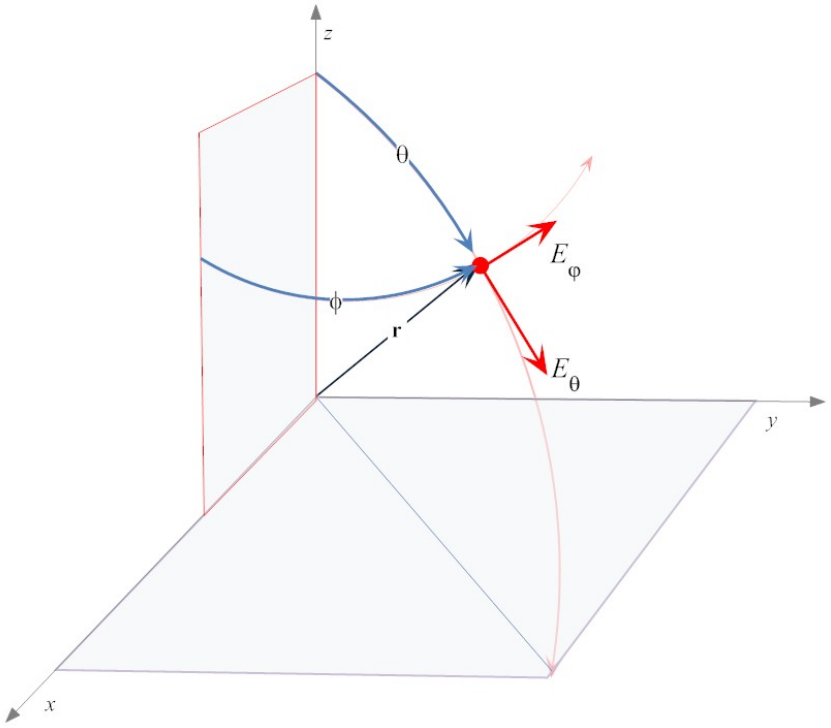


Figure 10. Electric field components in the local coordinates of the UAV.

Figure 11 shows the vertical $E_\theta$ polarization of the electric field produced by the patch antenna mounted on the underside of the UAV. The vertical polarization pattern consists of two downward-pointing lobes: one lobe points out the nose; the second lobe points out the tail. There is a deep null between the lobes that is aligned with the wings.

Figure 12 shows the horizontal $E_\phi$ polarization of the electric field produced by the patch antenna mounted on the UAV. The horizontal polarization pattern consists of two downward-pointing lobes: one lobe points out the right wing; the second lobe points out the left wing. The vertical and horizontal components of the UAV's tail are visible in the $E_\phi$ pattern. There is deep null between the lobes aligned with the fuselage.

Figures 13 and 14 present the 3-D plots of the electric fields $E_\theta$ and $E_\phi$ exceeding $-30$ dB respectively. Both figures orient their antenna patterns in the local $x$-$y$-$z$ coordinates of Figure 9. The UAV is flying horizontally so most of the broadcasts are directed down. The nose of the UAV points to the left in the figures; $E_\theta$ has lobes aligned with the fuselage and nulls aligned with the wings. $E_\phi$ has lobes aligned with the wings and nulls aligned with the fuselage. These nulls in both antenna patterns will be used to verify correct alignment of the UAV in the NEC-BSC simulations.

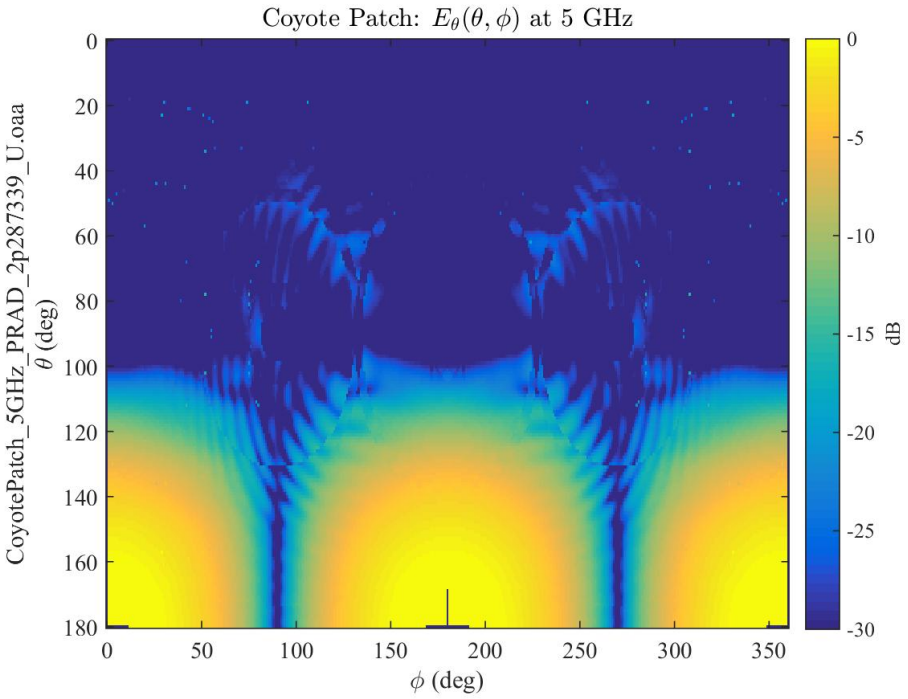


Figure 11. $E_\theta$ pattern for the bottom-mounted patch antenna; zenith angle $\theta$ sweeps from straight up $\theta = 0°$ to straight down $\theta = 180°$.

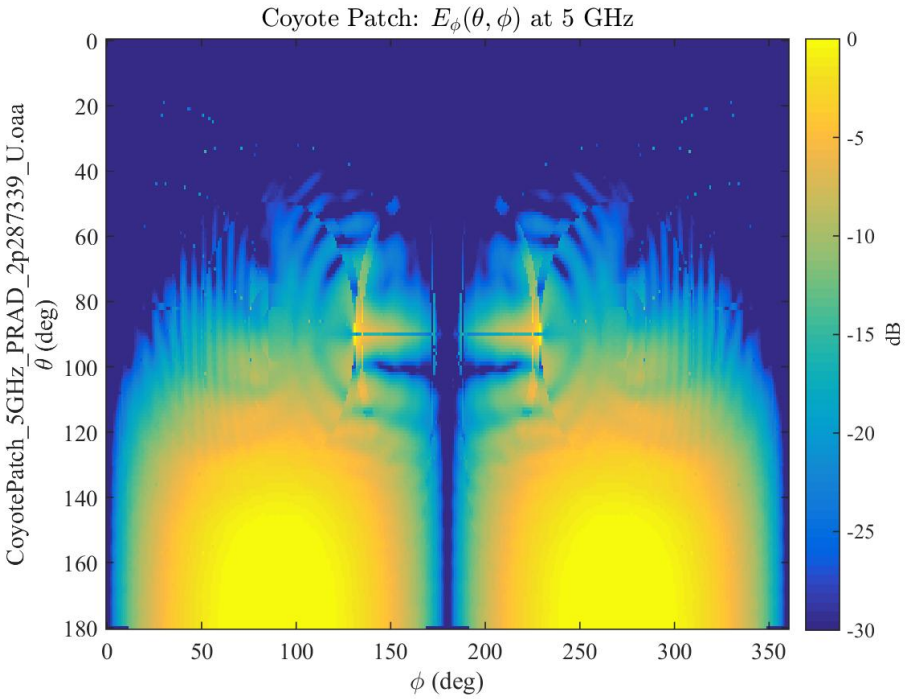


Figure 12. $E_\phi$ pattern for the bottom-mounted patch antenna; azimuth angle $\phi$ sweeps from $x$-axis at $\phi = 0°$ toward the $y$-axis at $\phi = 90°$.

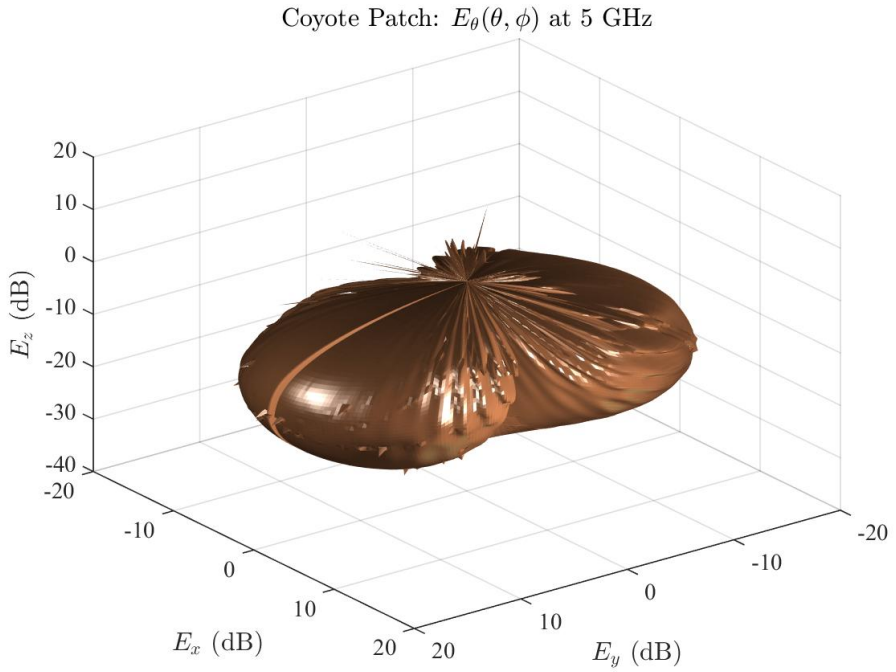


Figure 13. $E_\theta$ pattern for the bottom-mounted patch antenna in the UAV's local coordinate system; Values exceeding $-30$ dB.

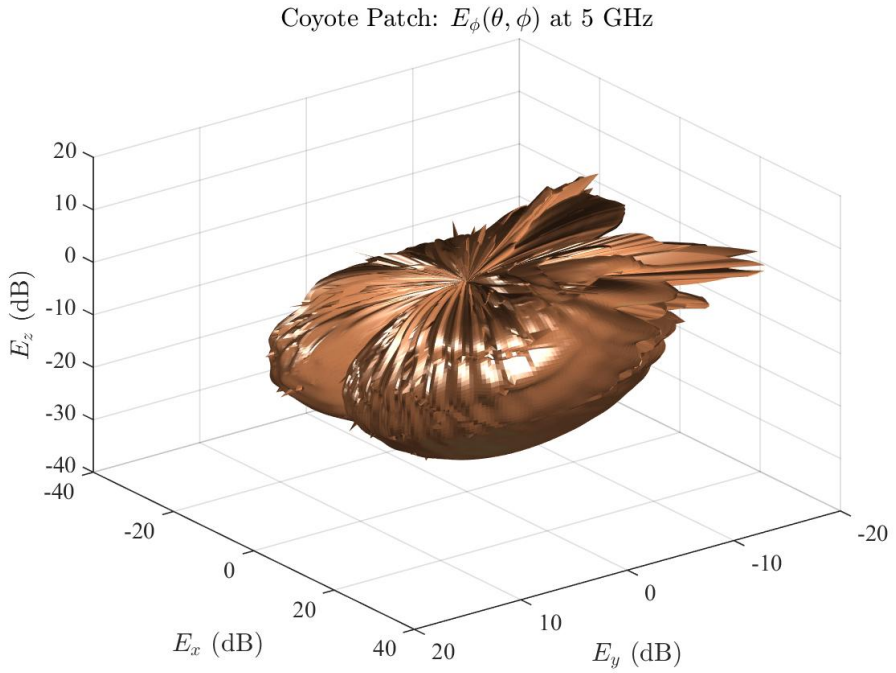


Figure 14. $E_\phi$ pattern for the bottom-mounted patch antenna in the UAV's local coordinate system; Values exceeding $-30$ dB.

# 4. UAV COVERAGE TO STREET-LEVEL RECEIVERS AT 5 GHZ

This section describes the 5-GHz "coverage" that the hovering UAV delivers to street-level receivers. Section 4.1 introduces the 3-D digital city where the UAV transmitter hovers over the origin. Section 4.2 compares the channels from the UAV to street-level receivers. By varying the height of the UAV, the coverage plots show the varying power levels, shadowing effects of the buildings, and the antenna pattern of the UAV. Section 4.3 rotates the UAV to verify the main beams and nulls of the patch antenna. Section 4.4 summarizes the coverage plots and verifies the UAV's antenna pattern is correctly integrated into the NEC-BSC simulations.

## 4.1 THE DIGITAL CITY

Figure 15 shows the 3-D geometry and locates the UAV directly over the origin with the "thumbtack" at $x_T = 0$, $y_T = 0$, and heights $z_T = 50$, 100, 250 meters. The UAV broadcasts into the city to street-level receivers. Moving the street-level receivers around in the city produces the "coverage" plots showing the channel from the UAV to each receiver's location.

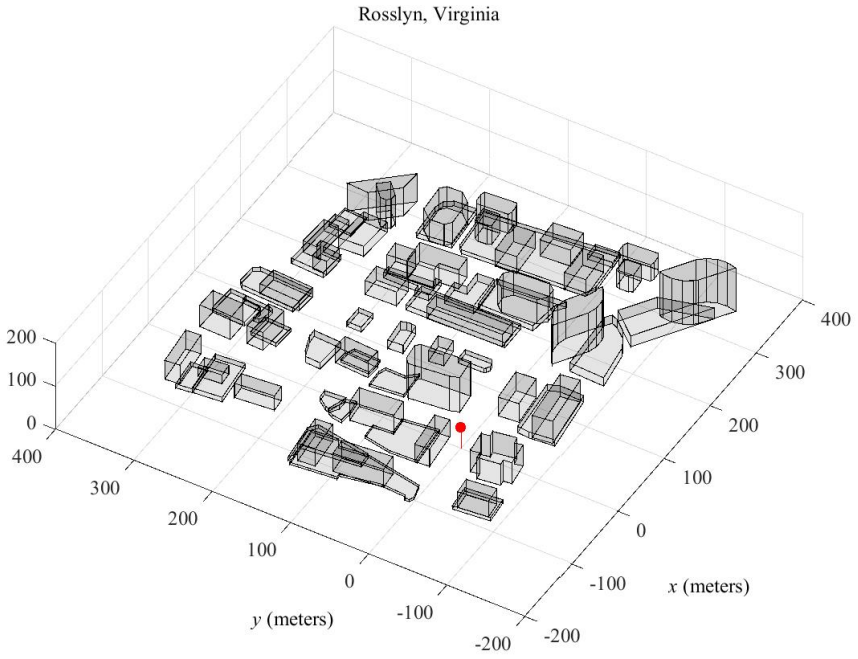


Figure 15. Urban geometry; The "thumbtack" shows the UAV carrying the transmitter hovering 50 meters above the origin.

The broadcasts in this simulated city are modeled by the 3-D propagation code NEC-BSC (Section 2.1). This software approximates the 3-D wave equation by coherently summing multiple reflections and diffractions of the transmitter's broadcast that arrive at the receivers locations. These reflections and diffractions are governed by the dielectrics of the building and the ground listed in Table 4.

Table 4. Dielectrics for the 3-D urban simulation at 5 GHz

| | Slab thickness | Relative Permittivity | Conductivity | References |
|---|---|---|---|---|
| Buildings | 0.3 (m) | 6.0 | 0.01 | [16] |
| Asphalt | Half plane | 2.56 | 0.0011 | [43, 4-30] |

The buildings are modeled with roofs and sides as concrete slabs 0.3 meters thick. Windows, iron reinforcements, building features, foliage, and city clutter is not modeled. The ground plane is modeled as a half-plane of asphalt. Consequently, this 3-D urban model produces *representative* RF environments. These RF environments model large-scale multipath rather than absolute levels [18]. As such, the channels produced by these simulations are best employed to reveal *relative* performance shifts produced by effects of UAV altitude, orientation, frequency, and bandwidth.

Figure 16 is a top view of the propagation environment. The UAV location is marked by the red dot over the origin. The UAV is aligned with the city's coordinate system—the nose of the UAV is parallel to the city's $+x$ axis, the wings of the UAV align with the city's $y$ axis, and the UAV is level. The UAV broadcasts to street-level receivers carrying half-wavelength vertical dipoles operating $z_R = 2$ meters above the street.

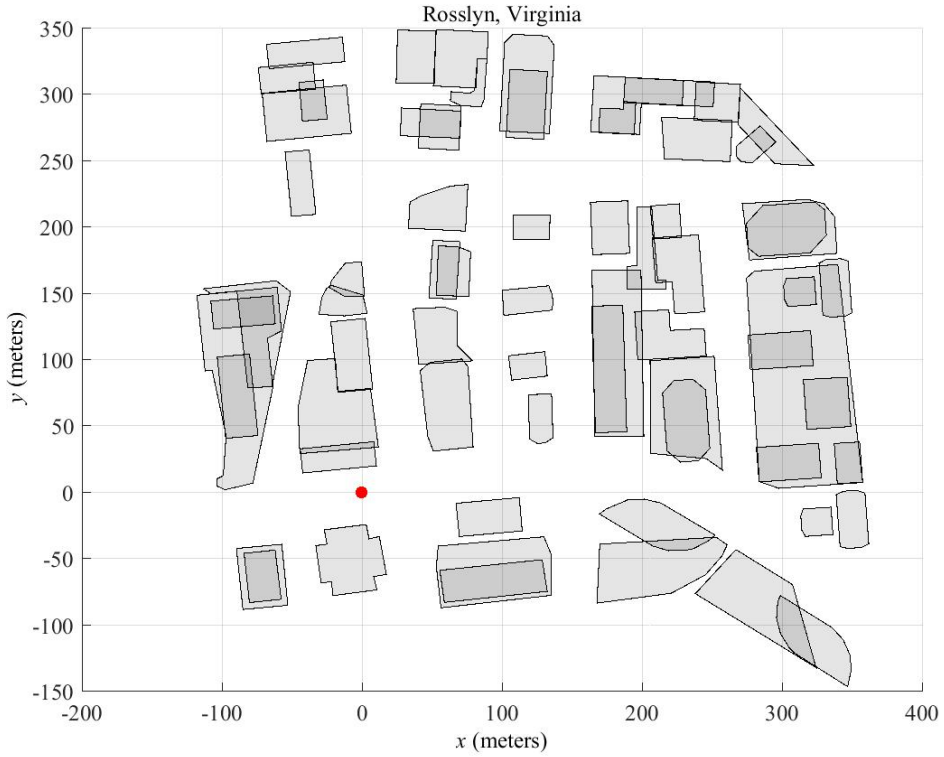


Figure 16. Top view of the 3-D simulation; the UAV is located over the origin at varying heights and transmitting into the city.

Figure 17 marks the *coverage area* of the 3-D simulations as the red patch. This patch is a horizontal rectangular slice in 3-D space placed 2 meters above the street. The UAV transmits to the street-level receivers in the red patch. These receivers employ half-wavelength dipoles at 2 meters height. The following figures plot this "slice" of the electric field intercepted by receivers on this patch.

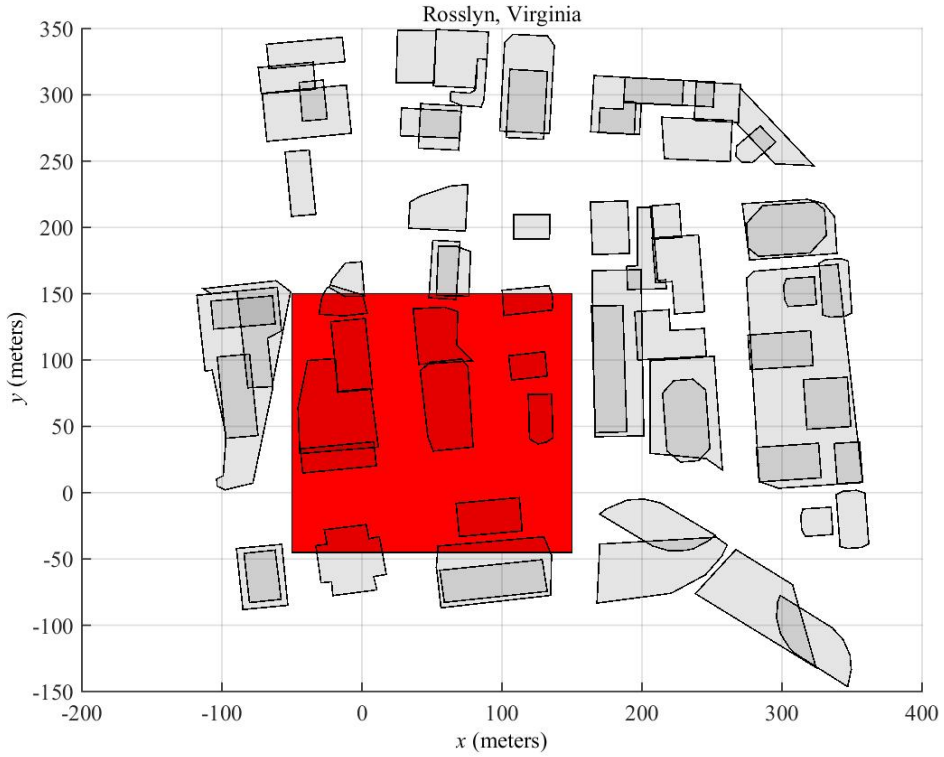


Figure 17. Top view showing the street-level coverage area placed two meters above the street.

### 4.2 COVERAGE AS A FUNCTION OF HEIGHT

Figures 18, 19, and 20 are coverage plots produced by the UAV hovering over the origin and broadcasting to the street-level receivers. Each figure shows the channel magnitude from the UAV at location $\mathbf{r}_T$ to the street-level receivers at the locations $\mathbf{r}_R$:

$$|h(f_C;\mathbf{r}_T,\mathbf{r}_R)|^2 \begin{cases} f_C = 5 & \text{[GHz]}, \\ \mathbf{r}_T = \begin{bmatrix} 0 & 0 & z_T \end{bmatrix}^{\mathsf{T}} & z_T = 50, 100, 150 \ \text{[m]}, \\ \mathbf{r}_R = \begin{bmatrix} x_R & y_R & 2 \end{bmatrix}^{\mathsf{T}} & -50 \le x_R \le 150; -45 \le y_R \le 145 \ \text{[m]}. \end{cases}$$

The channel takes the signal from the input terminals of the patch antenna to the output terminals of the vertical dipole at each street-level receiver location. This receive antenna intercepts the *vertical* component of the local electric field. In a line-of-sight condition, the receive antenna primarily responds to the $E_\theta$ component nulls in azimuth at 90° and 270° as seen in Figure 11. Because the UAV points along the city's $+x$-axis, these nulls are parallel to the city's $y$-axis. As the UAV increases in height, these nulls becomes more visible. Likewise, the main lobes of the UAV illuminate the region along the $x$-axis. Off-axis regions require more altitude to diffract energy into the side streets. These observations provide some verification that the UAV antenna pattern is correctly integrated into NEC-BSC.

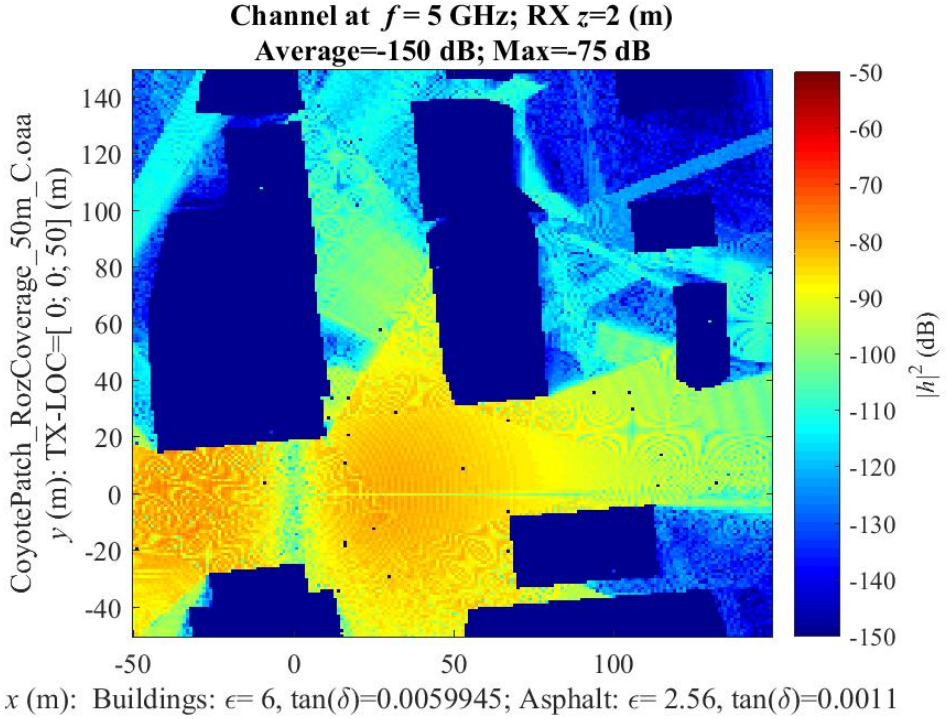


Figure 18. Channel coverage at 5 GHz; UAV 50 meters above the origin.

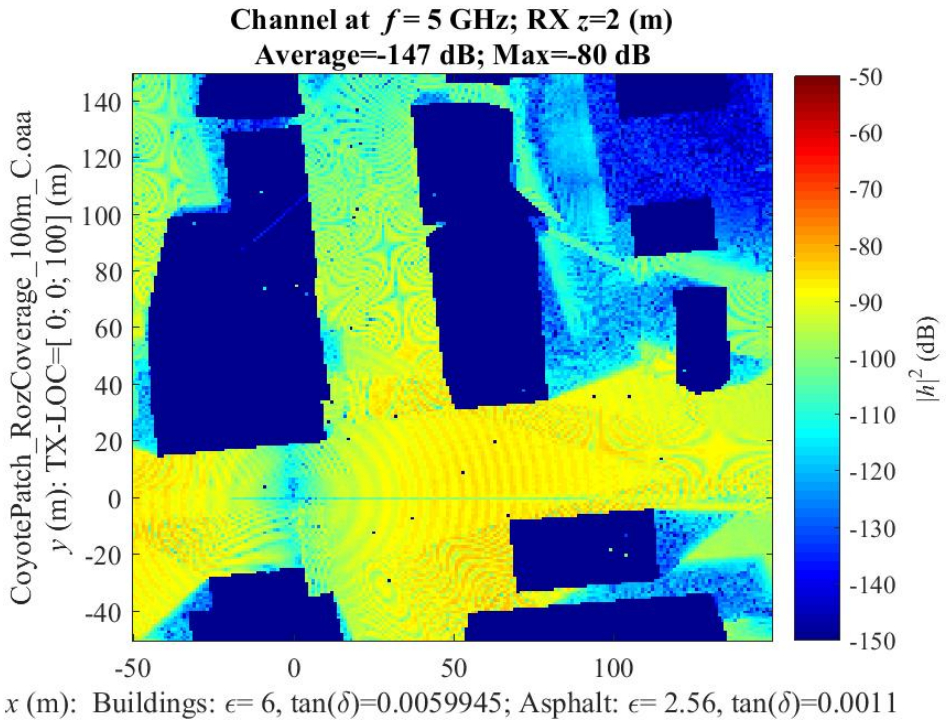


Figure 19. Channel coverage at 5 GHz; UAV 100 meters above the origin.

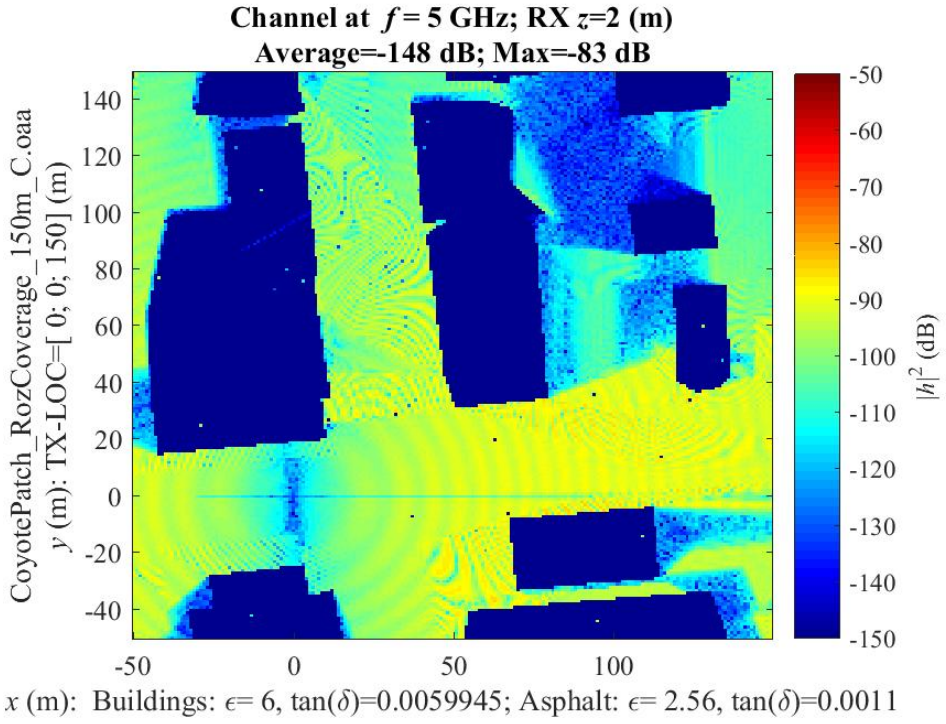


Figure 20. Channel coverage at 5 GHz; UAV 150 meters above the origin.

Figure 21 shows the coverage when the UAV is rotated in azimuth to reveal the $E_\theta$ null:

$$|h(f_C;\mathbf{r}_T,\phi_T;\mathbf{r}_R)|^2 \begin{cases} f_C = 5 & \text{[GHz]}, \\ \mathbf{r}_T = \begin{bmatrix} 0 & 0 & z_T \end{bmatrix}^\mathsf{T} & z_T = 150 \text{ [m]}, \\ \phi_T = 90^\circ. \end{cases}$$

The nulls in the patch antenna now point along the $x$-axis of the scenario. The main lobe now lights up the street parallel to the $y$-axis.

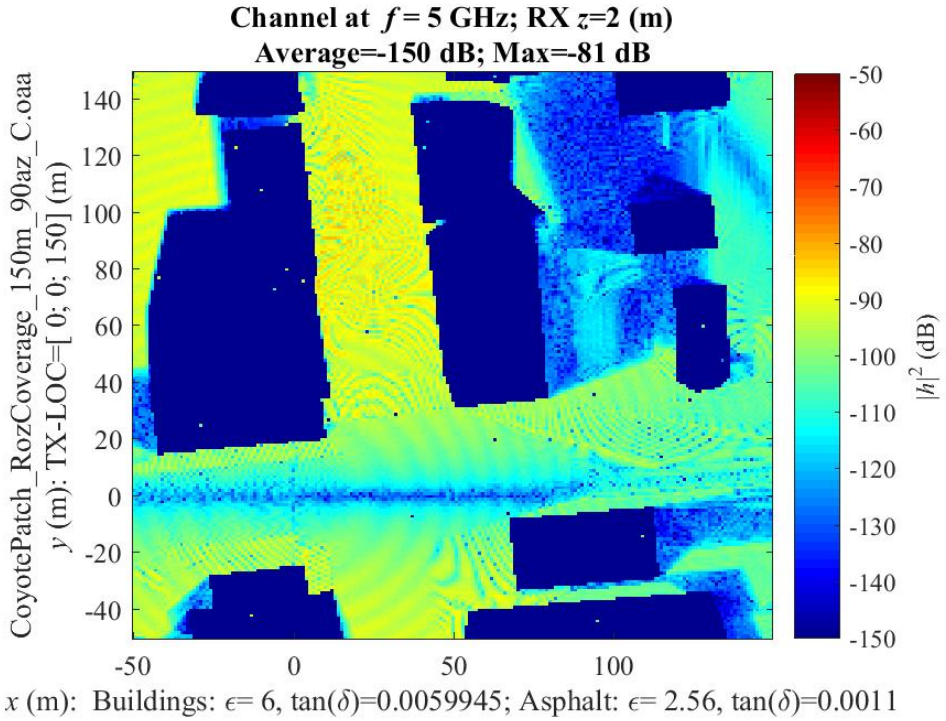


Figure 21. Channel coverage at 5 GHz; UAV transmitter is 150 meters above the origin and aligned with the $y$-axis.

### 4.3 COVERAGE AND PATTERN ROTATIONS

Figure 22 increases the UAV height while aiming the nose of the UAV into the coverage region:

$$|h(f_C; \mathbf{r}_T, \phi_T; \mathbf{r}_R)|^2 \begin{cases} f_C = 5 & \text{[GHz]}, \\ \mathbf{r}_T = \begin{bmatrix} 0 & 0 & z_T \end{bmatrix}^{\mathsf{T}} & z_T = 200 \text{ [m]}, \\ \phi_T = 45^\circ. \end{cases}$$

For this orientation, the main lobe lights up both streets.

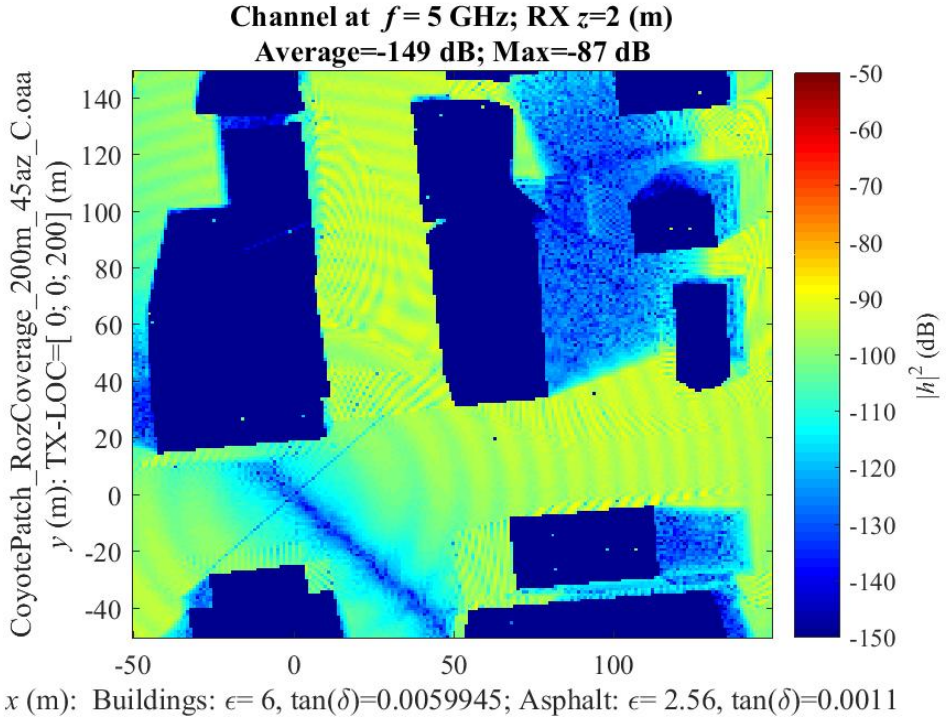


Figure 22. Channel coverage at 5 GHz; UAV transmitter is 200 meters above the origin and rotated $45^\circ$ in azimuth.

Figure 23 increases the UAV height again while aiming the null into the coverage region:

$$|h(f_C; \mathbf{r}_T, \phi_T; \mathbf{r}_R)|^2 \begin{cases} f_C = 5 & \text{[GHz]}, \\ \mathbf{r}_T = \begin{bmatrix} 0 & 0 & z_T \end{bmatrix}^{\mathsf{T}} & z_T = 250 \text{ [m]}, \\ \phi_T = 135^\circ. \end{cases}$$

The figure shows the nulls in the patch antenna limit the coverage in both streets.

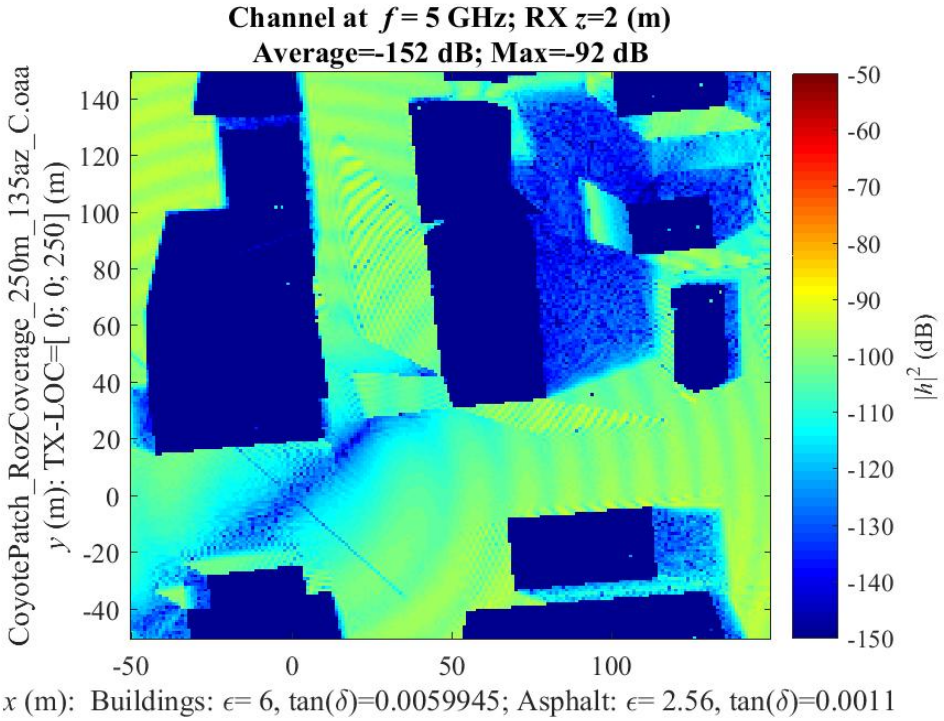


Figure 23. Channel coverage at 5 GHz; UAV transmitter is 200 meters above the origin and rotated $135^\circ$ in azimuth.

### 4.4 SUMMARY

The first observation about the coverage plots is that features of the UAV's antenna patterns support the claim that the UAV or, equivalently, the antenna patterns are correctly placed in the simulations. Assuming correct placement, the second observation is that these coverage plots reveal multiple trade-offs that arise as a function of the UAV height.

**C-1** Coverage depends on the UAV's orientation with respect to the city's geometry

**C-2** The null in the $E_\theta$ pattern increases with UAV height

**C-3** Overall coverage increases with UAV height

These coverage plots assume a stationary UAV broadcasting to the street-level receivers. However, a moving UAV causes the coverage plots to vary. A stationary street-level receiver observes the varying coverage as channel fading. The next section examines such a moving UAV and associated fading at the stationary receiver.

# 5. UAV TRACKS AT 5 GHZ AND 200-MHZ BANDWIDTH

This section presents air-to-ground channels as the UAV flies along tracks parallel to the $y$-axis while broadcasting to a fixed street-level receiver. The channels show a dense multipath and distinct propagation regimes that vary with height. Section 5.1 set out the UAV track geometry. Section 5.2 flies the UAV on the track at 50 meters height to show multiple fading regimes along the track. Section 5.3 raises the track height to 100 meters. The additional height simplifies the fading. Two-Ray Rician fading is credible fading model when there is minimal blockage. Section 5.4 raises the track height to 200 meters. This additional height removes most of the blockage effects, simplifies the fading, and shows the effect of the patch antenna's null. Section 5.5 summarizes these findings—raising the height of the UAV simplifies the air-to-ground channel to Shadowed Two-Ray Rician fading.

## 5.1 GEOMETRY OF THE TRACKS

The UAV flies along tracks parallel to the $y$-axis at 50, 100, and 200 meters height. Figure 24 presents the top view of the UAV tracks. The location $\mathbf{r}_T$ of the UAV on these tracks is

$$\mathbf{r}_T(y_T) = \begin{bmatrix} x_T \\ y_T \\ z_T \end{bmatrix} \begin{cases} x_T = 25 \text{ [m]}, \\ 0 \le y_T \le 300 \text{ [m]}, \\ z_T = 50, 100, 200 \text{ [m]}. \end{cases}$$

The UAV is oriented to fly along this track. Referring to Figure 10, the nose of the UAV is aligned with the $+y$ axis, the wings are aligned with the $x$ axis, and the bottom-mounted patch antenna is horizontal. Figure 24 also marks the street-level receiver equipped with a half-wavelength vertical dipole at location:

$$\mathbf{r}_R = \begin{bmatrix} 150 \\ 100 \\ 2 \end{bmatrix} \quad \text{[m]}.$$

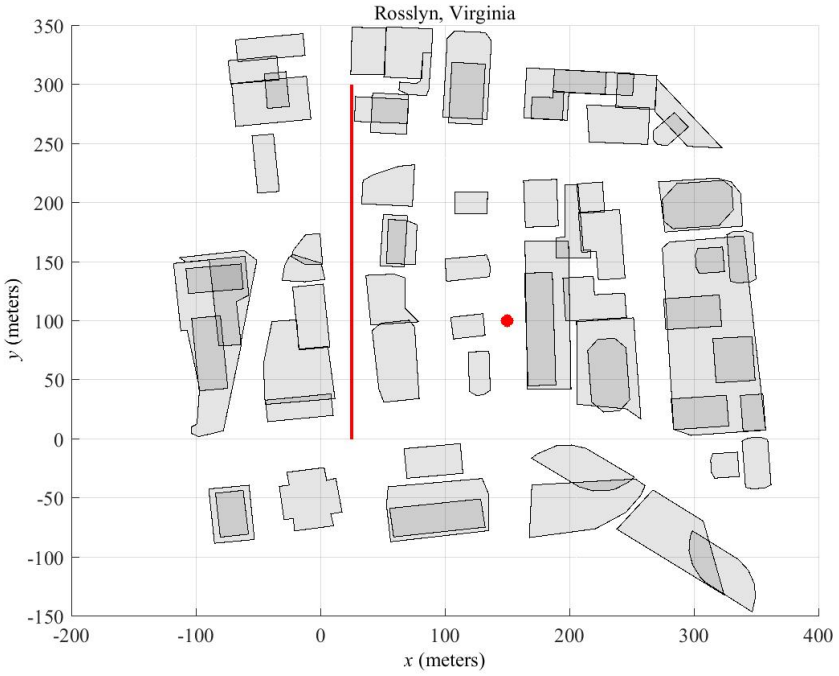


Figure 24. Top view of the UAV's tracks (red line) offset from the $y$-axis by $x_T = 25$ meters; red dot marks the street-level receiver's location.

### 5.2 TRACK AT 50-METER HEIGHT

Figure 25 displays the 200-MHz channel as the UAV flies along the $y$-axis track at 50-meter height. The figure displays the channel

$$\left|\widehat{h}(f;\mathbf{r}_T,\mathbf{r}_R)\right|^2 \quad \begin{cases} \mathbf{r}_T = \begin{bmatrix}25 & y_T & 50\end{bmatrix}^{\mathsf{T}} \text{ [m]} \\ \mathbf{r}_R = \begin{bmatrix}150 & 100 & 2\end{bmatrix}^{\mathsf{T}} \text{ [m]} \end{cases}$$

as a function of the UAV's position $y_T$ and frequency $f$. This representation shows the channel is a collection of transfer functions parameterized by the spacial coordinate $y_T$. This channel formalism as a *space-varying transfer function* is the spatial analog of Bello's *time-varying transfer function* [11]:

$$\widehat{h}(f;\mathbf{r}_T,\mathbf{r}_R) = \int_{-\infty}^{\infty} e^{-j2\pi f\tau} h(\tau;\mathbf{r}_T,\mathbf{r}_R)d\tau,$$

where the "hat" denotes the Fourier transform and $h(\tau;\mathbf{r}_T,\mathbf{r}_R)$ is the spatial analog of Bello's *delay spread function* [11]. The prominent features of this channel in Figure 25 are the horizontal nulls traversing the entire frequency band. Section 6 will show these spectral nulls are caused by shadowing and blockage by the city's buildings. The deep null at $y_T = 100$ meters is caused, in part, by the corresponding null at $\phi = 90°$ in the patch antenna as the UAV flies past the receiver (See Figure 11).

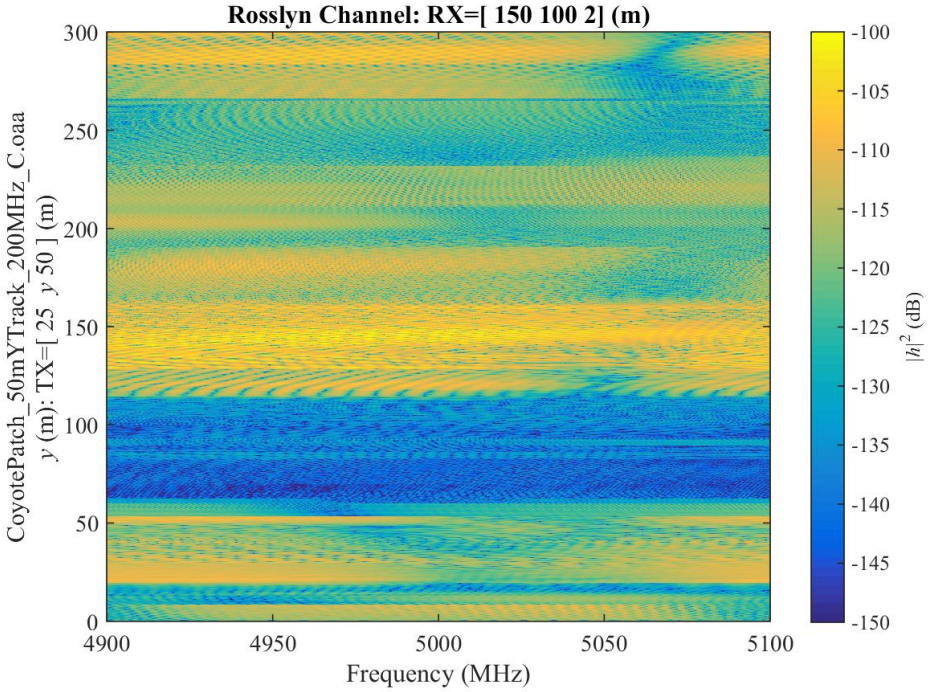


Figure 25. The 200-MHz channel; UAV flying the $y$-axis track at 50-meter height broadcasting to the street-level receiver.

Further understanding of this channel is revealed by the delay spread function:

$$h(\tau;\mathbf{r}_T,\mathbf{r}_R) = \int_{-\infty}^{\infty} e^{+j2\pi f\tau}\widehat{h}(f;\mathbf{r}_T,\mathbf{r}_R)df.$$

However, the space-varying transfer function $\widehat{h}(f;\mathbf{r}_T,\mathbf{r}_R)$ is only known over its 200-MHz bandwidth. Consequently, estimates of the delay spread function are obtained by windowing in the frequency domain:

$$h(\tau;\mathbf{r}_T,\mathbf{r}_R) \approx h(\tau;\mathbf{r}_T,\mathbf{r}_R,w_G) = \int_{-\infty}^{\infty} e^{+j2\pi f\tau} h(f;\mathbf{r}_T,\mathbf{r}_R)\widehat{w}_G(f)df,$$

where $w_G(t)$ is the Gaussian window

$$w(t) = \frac{1}{t_G} \exp\left(-\pi \frac{t^2}{t_G^2}\right).$$

The scaling in the time domain is rigged for unit area:

$$1 = \int_{-\infty}^{\infty} w(t)dt.$$

If the channel is to deliver a time resolution $\Delta t$ at level $w_0$:

$$w_0 = t_G w(\Delta t/2),$$

the time spread $t_G$ is set at

$$t_G = \frac{\Delta t}{2} \sqrt{\frac{-\pi}{\log(w_0)}}.$$

Figure 26 shows the delay spread estimate with the time resolution $\Delta t = 1$ $\mu$s for $w_0 = -20$ dB. This estimate shows the "fat" channel switching on and off as the UAV flies past buildings.

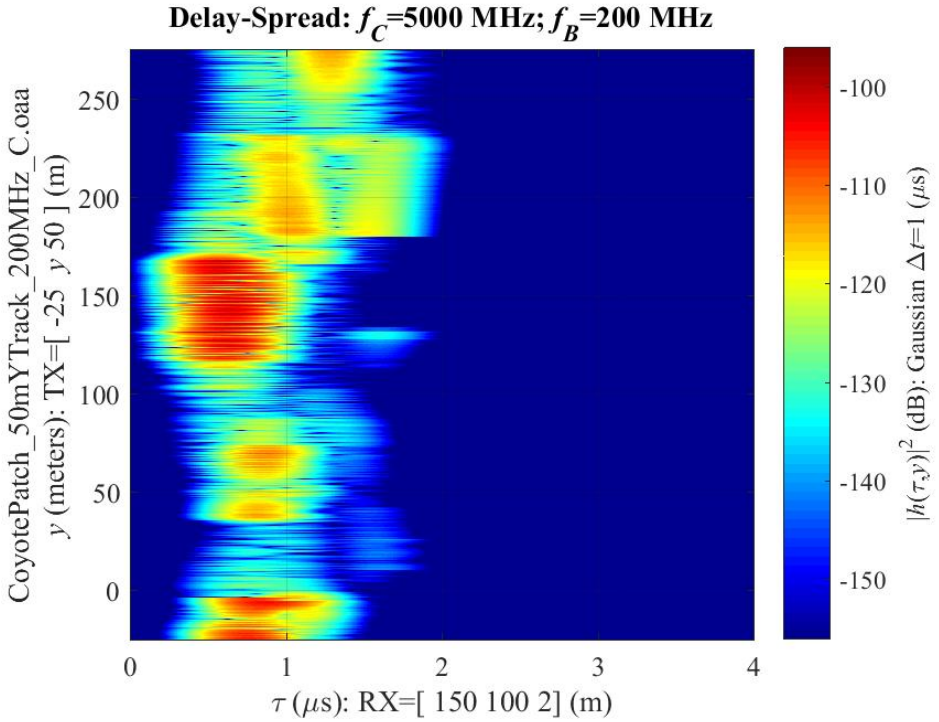


Figure 26. Delay-spread estimate; UAV flying the $y$-axis track at 50-meter height broadcasting to the street-level receiver; Gaussian window with 1-$\mu$s resolution.

Figure 27 employs the Gaussian window with 0.1-$\mu$s resolution. The finer resolution reveals that the "fat" path consists of multiple paths—even in the nulls of the antenna and the blockage. Figure 28 employs the Gaussian window with 0.01-$\mu$s resolution. There are multiple channels that switch on and off as the UAV flies past buildings. Therefore, a credible channel model for this track is a special case of Equation 6

$$h(y_T, \tau) = \sum_{n=1}^{N} h_n(y_T)\delta(\tau - \tau_n(y_T)), \tag{8}$$

where $N = 6$ encompasses the strongest paths on this plot.

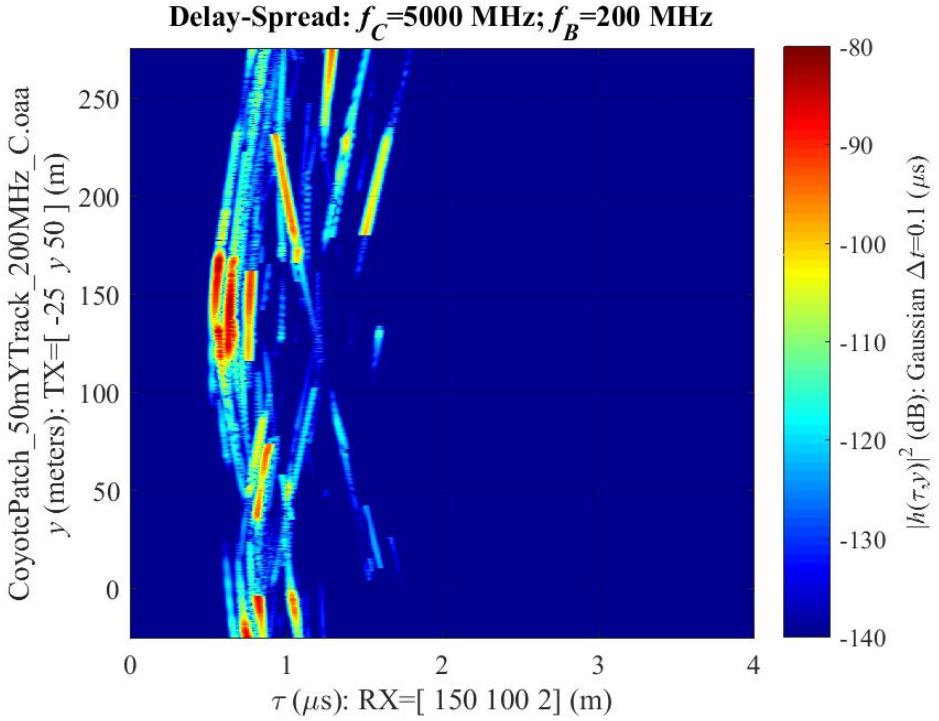


Figure 27. Delay-spread estimate; UAV flying the $y$-axis track at 50-meter height broadcasting to the street-level receiver; Gaussian window with 0.1-$\mu$s resolution.

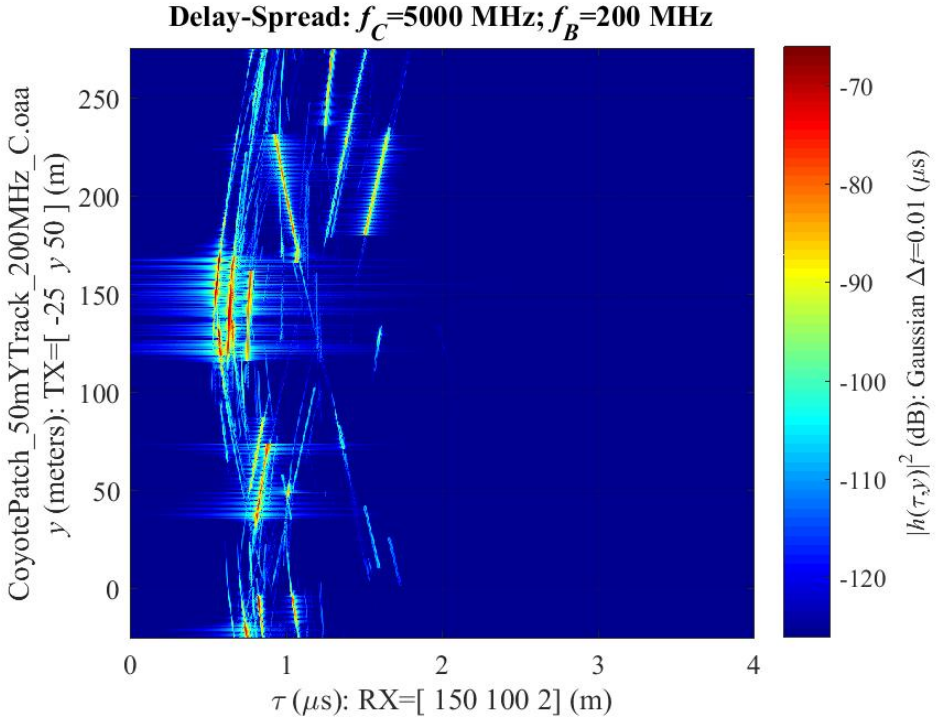


Figure 28. Delay-spread estimate; UAV flying the $y$-axis track at 50-meter height broadcasting to the street-level receiver; Gaussian window with 0.01-$\mu$s resolution.

If the channel is modeled assuming a bandwidth $f_B$ of 1 MHz or less, the paths in the delay region from 0.5 to 1.5 $\mu$s cannot be resolved. Therefore, a narrowband channel approximation to Equation 8 takes the form

$$h_{\mathrm{NB}}(y_T;\tau) = \left\{ \sum_{n=1}^{N} h_n(y_T) \right\} \delta(\tau - \tau_0),$$

where the gross delay is $\tau_0 \approx 0.8$ $\mu$s. Figure 29 plots the magnitude of this channel as a function of the UAV's position along the 50-meter track. This channel is the slice at 5 GHz extracted from the 200-MHz channel in Figure 25.

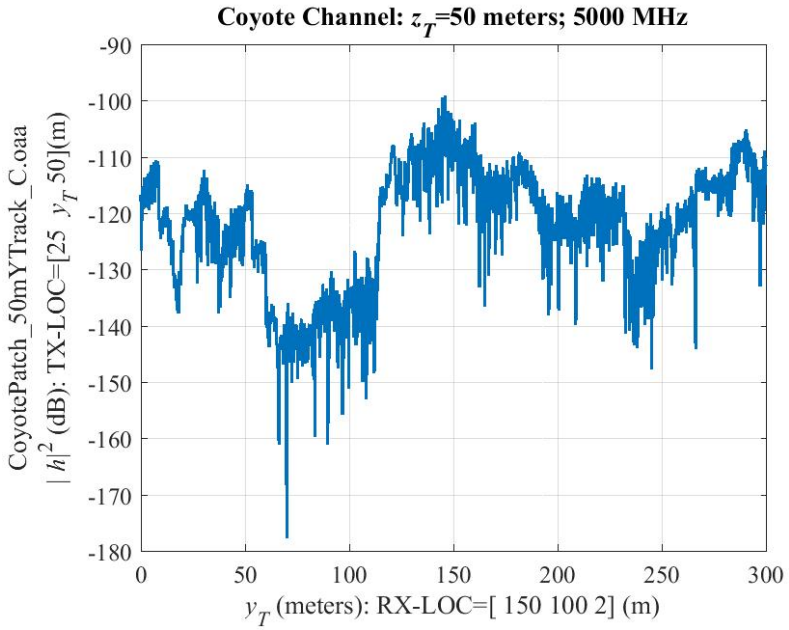


Figure 29. Narrowband channel at 5-GHz; UAV flying the $y$-axis track at 50-meter height; fading is multi-path interference modulated by shadowing and punctuated by blockage.

On a local scale, the channel shows fast fading with a spatial interference pattern with a period of a few meters. Figure 28 shows that this interference pattern is caused by two or three paths. This local fast fading is modulated with a slower fading varying on the 10-meter scale. Viewed over the entire track, this channel shows the local fading is punctuated with deep fades. Consequently, this narrowband channel is best understood using the wideband delay-spread estimates. That is, Figure 28 shows the narrowband channel in Figure 29 is the projection of multiple paths subject to

- shadowing,
- blockage, and
- slowly varying delays.

The following sections will show that the local fading is well modeled as Shadowed Two-Ray Rician (See Example 5) punctuated by a blocking pattern. Therefore, the low-flying UAV channels are best modeled in specific 3-D scenarios rather than the standard stationary fading models.

### 5.3 TRACK AT 100-METER HEIGHT

Figure 30 displays the 200-MHz channel as a function of the UAV's position $y_T$ and frequency $f$ as the UAV flies the $y$-axis track at 100-meter height:

$$|\widehat{h}(f;\mathbf{r}_T,\mathbf{r}_R)|^2 \quad \begin{cases} \mathbf{r}_T = \begin{bmatrix} 25 & y_T & 100 \end{bmatrix}^\mathsf{T} & \text{[m]} \\ \mathbf{r}_R = \begin{bmatrix} 150 & 100 & 2 \end{bmatrix}^\mathsf{T} & \text{[m]} \end{cases} .$$

The channel shows blockage and shadowing by the buildings in the first half of the track ($0 < y_T < 150$). In the second half of the track, multi-path interference appears. The delay-spread function untangles the multiple paths in this region.

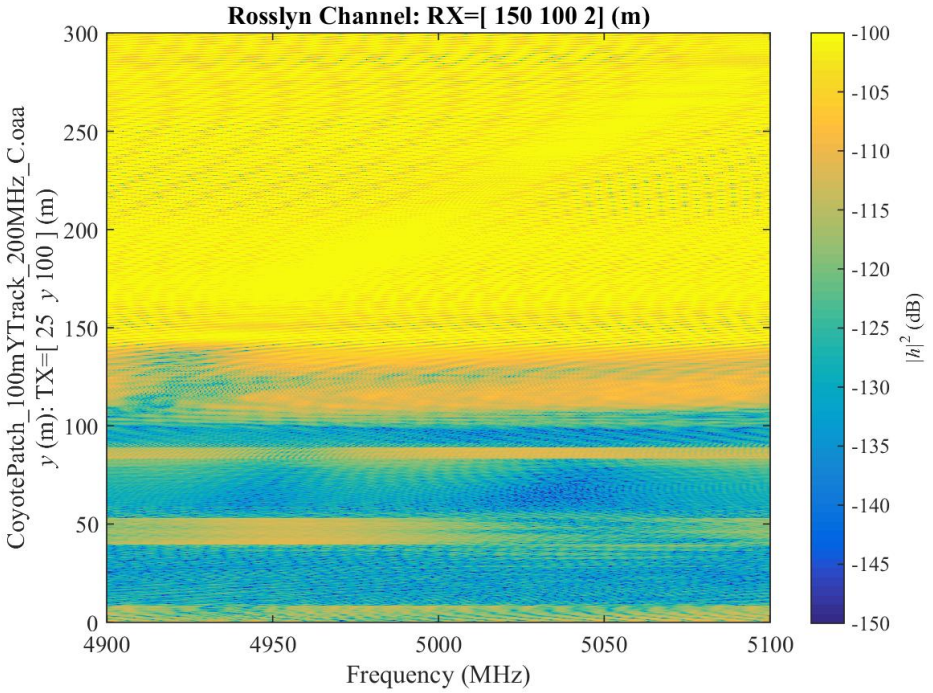


Figure 30. The 200-MHz channel; UAV on the 100-meter track broadcasting to the street-level receiver.

Figure 31 estimates the *delay-spread* function of this channel using the Gaussian window with time resolution $\Delta t = 0.1$ $\mu$s. In the first half of the track, the channel is switching on and off as the UAV flies past buildings. The second half of the track shows two strong paths followed by a weaker third path. Figure 32 shows the narrowband channel at 5 GHz. A local view of the fading shows fast fading caused by the interference between the two strong paths in Figure 30. This fading fading is modulated by a slower shadowing. Finally, this Shadowed Multi-Ray fading is punctuated by the "on-and-off" blockage.

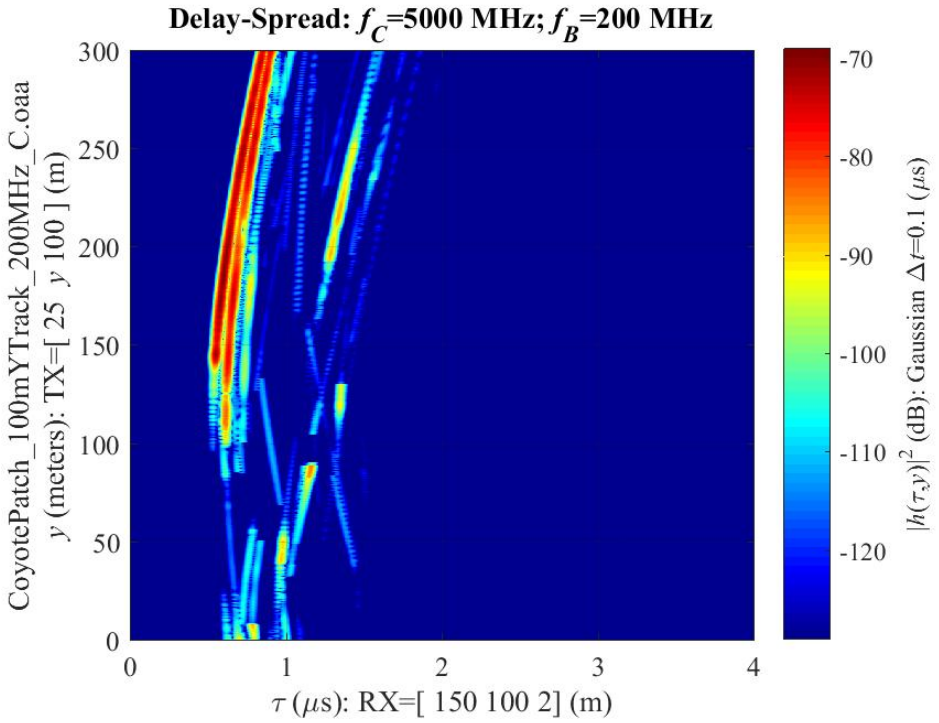


Figure 31. Delay-spread estimate; UAV flying the $y$-axis track at 100-meter height broadcasting to the street-level receiver; Gaussian window with 0.1-$\mu$s resolution.

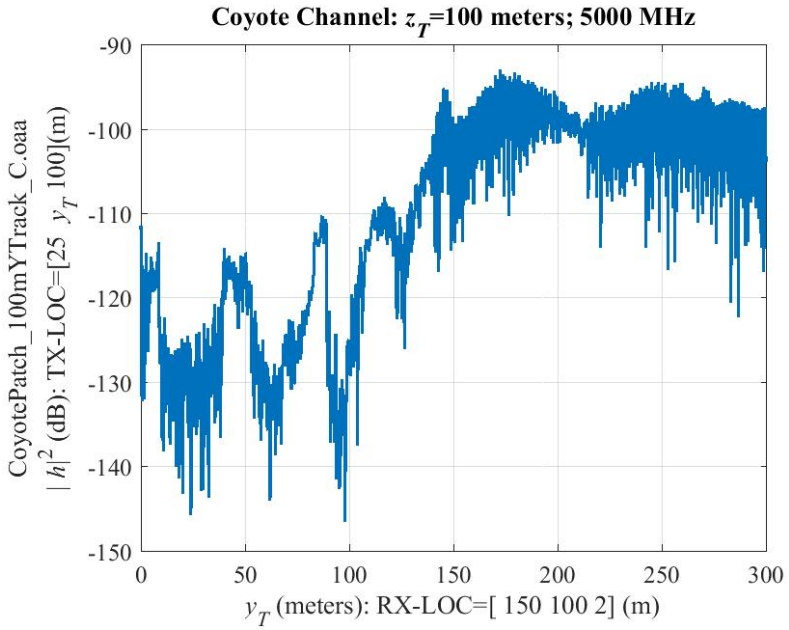


Figure 32. Narrowband channel at 5 GHz; UAV flying the $y$-axis track at 100-meter height; fading is multi-path interference modulated by shadowing and punctuated by blockage.

### 5.4 TRACK AT 200-METER HEIGHT

Figure 33 displays the 200-MHz channel as the UAV flies the $y$-axis track at 200-meter height:

$$|\widehat{h}(f;\mathbf{r}_T,\mathbf{r}_R)|^2 \quad \begin{cases} \mathbf{r}_T = \begin{bmatrix} 25 & y_T & 200 \end{bmatrix}^\mathsf{T} \ \text{[m]} \\ \mathbf{r}_R = \begin{bmatrix} 150 & 100 & 2 \end{bmatrix}^\mathsf{T} \ \text{[m]} \end{cases} .$$

At this height, there is no blockage by the buildings. The deep null at $y_T = 100$ meters is caused by the null in patch antenna as the UAV flies past the receiver (See Figure 11). The delay-spread estimates untangle the multiple paths in this region.

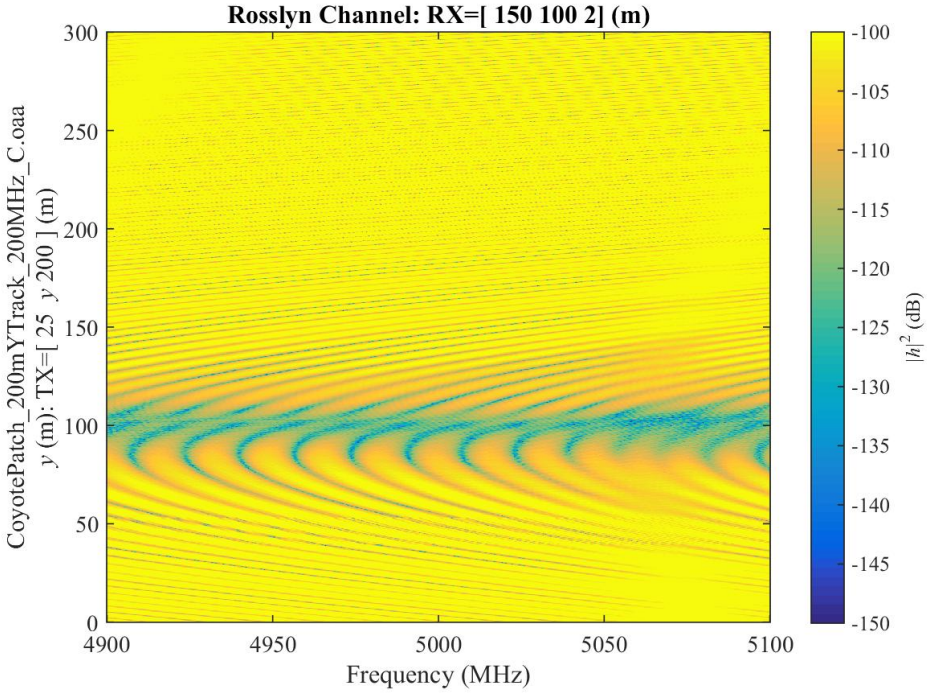


Figure 33. The 200-MHz channel; UAV flying the $y$-axis track at 200-meter height broadcasting to the street-level receiver.

Figure 34 estimates the *delay-spread* function of this channel using the Gaussian window parameterized with the time resolution $\Delta t = 0.1$ $\mu$s. There are two strong paths with the null at $y_T$ that is the UAV's closest approach the receiver. Figure 35 uses the Gaussian window with the time resolution set to $\Delta t = 0.01$ $\mu$s to separate the paths. Therefore, a credible channel model for this track is a special case of Equation 2 where only the two strongest paths are modeled:

$$h(y_T,\tau) = h_1(y_T)\delta(\tau - \tau_1(y_T)) + h_2(y_T)\delta(\tau - \tau_2(y_T)). \tag{9}$$

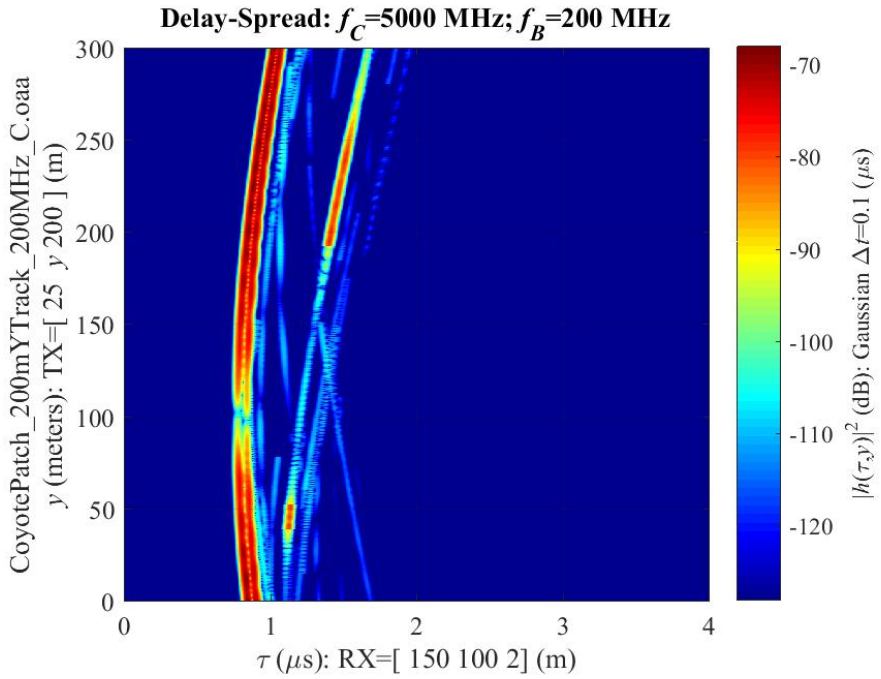


Figure 34. Delay-spread estimate; UAV on the 200-meter track broadcasting to the street-level receiver; Gaussian window with 0.1-$\mu$s resolution.

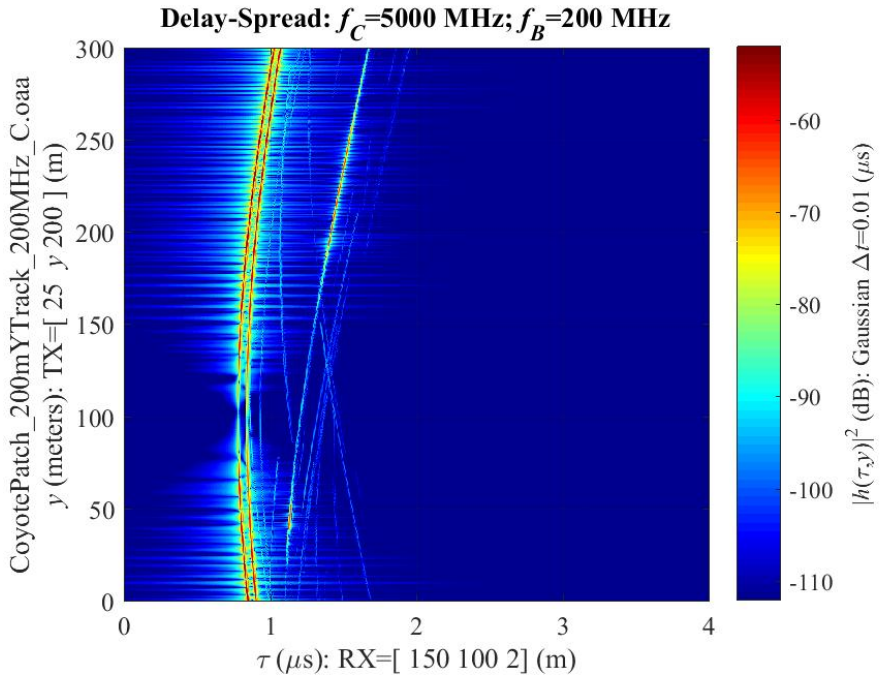


Figure 35. Delay-spread estimate; UAV on the 200-meter track broadcasting to the street-level receiver; Gaussian window with 0.01-$\mu$s resolution.

Figure 36 shows the narrowband channel along the 200-meter track. This channel is the slice at 5 GHz from the 200-MHz channel in Figure 33. The deep null is caused by the patch antenna's null as the UAV flies path the receiver. Outside this null, the fading appears to exhibit the standard two-ray interference. The variation in the interference period is caused by the "bowing" in delay of the paths in Figure 36.

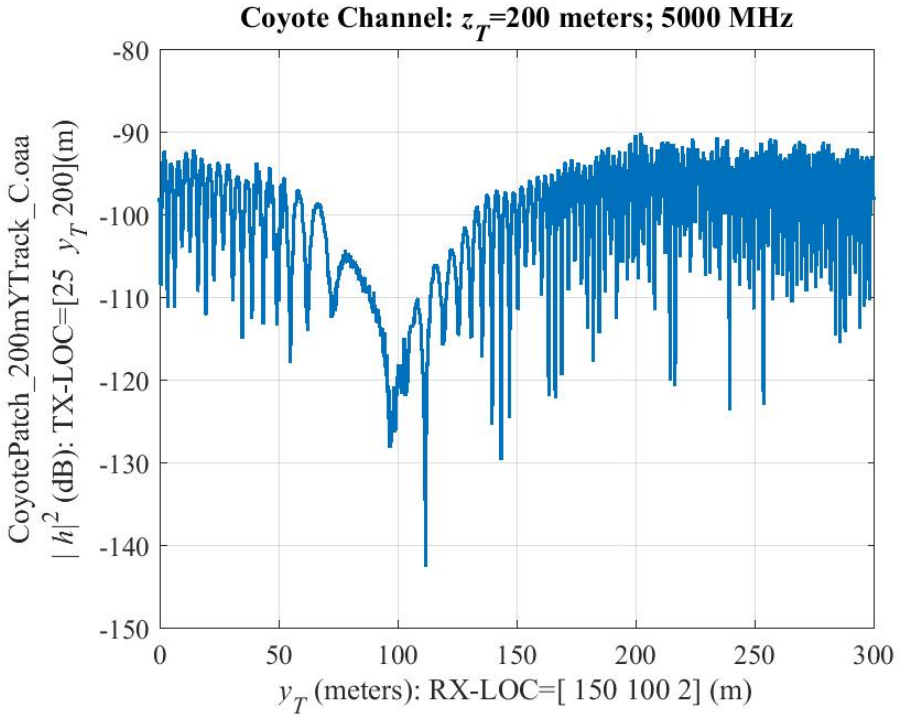


Figure 36. Narrowband channel of the UAV flying the $y$-axis track at 200-meter height; fading is two-path interference with the deep fade caused by the antenna null.

A narrowband approximation to this channel follows from Equation 9 by forcing both paths to arrive at the same time $\tau_0 \approx 0.8 \quad [\mu s]$:

$$h_{\mathrm{NB}}(y_T, \tau) = \{h_1(y_T) + h_2(y_T)\} \ \delta(\tau - \tau_0). \tag{10}$$

The question that arises from this model asks:

*What is the fading on these paths?*

Figure 37 provides one answer by plotting the amplitude of$\{h_1(t)\}$ and $\{h_2(t)\}$. Both fading processes show the action of the antenna null and the compression of the interference pattern as the distance increases between the UAV and the receiver. The local view shows both fading processes exhibit classic "two-ray" interference subject to slight shadowing as in Example 5:

$$\begin{aligned} h_1(t) &= \zeta_1(t)\{h_{1,1}(t) + h_{1,2}(t)\} \\ h_2(t) &= \zeta_2(t)\{h_{1,1}(t) + h_{1,2}(t)\}, \end{aligned}$$

where $\{h_{m,n}(t)\}$ is Rician fading. That is, the fading in Figure 36 admits Four-Ray Rician fading as a local model. However, the fading examples in Section 2.3 argue that Shadowed Two-Ray fading is a credible approximation using fewer fading processes.

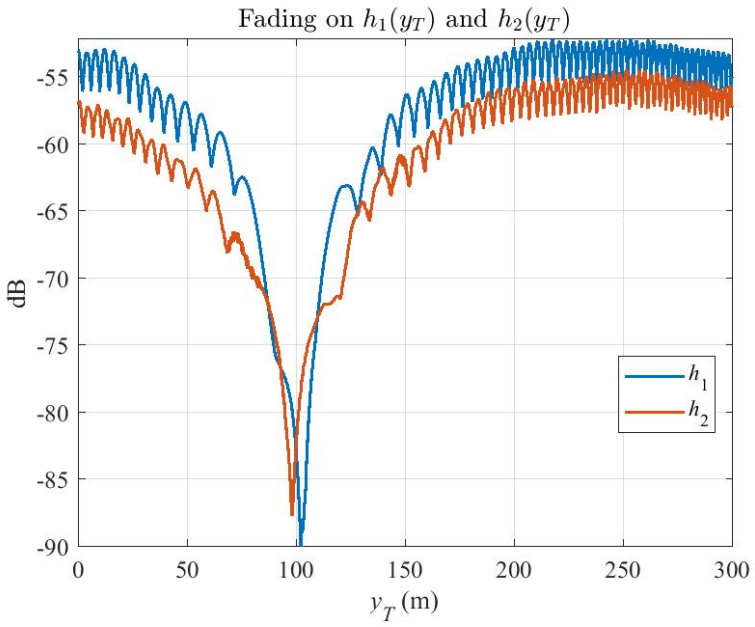


Figure 37. Fading on the two strong paths along the 200-meter track.

### 5.5 SUMMARY

Narrowband UAV channels along these straight-line tracks show fast multipath fading subject to

- Antenna,
- Blockage,
- Shadowing.

Specifically, the delay-spread estimates show these narrowband channels are projections of multiple paths that are approximated by Shadowed Two-Ray Rician fading of the form:

$$h_{\mathrm{NB}}(y_T,\tau) = \overbrace{a(y_T)}^{\text{antenna}}\ \overbrace{b(y_T)}^{\text{blocking}}\ \overbrace{\zeta(y_T)}^{\text{shadowing}}\ \overbrace{\{h_1(y_T)+h_2(y_T)\}}^{\text{multipath}}\ \delta(\tau-\tau_0).$$

One conclusion from this modeling is that the UAV channels are best modeled in specific 3-D scenarios rather than the standard stationary fading models. One caution is that these fading models are specific to this 3-D digital city whereas shadowing and multipath fit into the more general fast- and slow-fading insightfully described by [4]

> The small-scale multipath fading is often modeled using Rayleigh, Rician, or Nakagami distribution. The latter one is versatile enough to encompass the Rayleigh distribution as a special case and to approximate the Rician distribution. The large-scale fading (shadowing) is often modeled using a lognormal distribution ....

A second caution follows from the specificity of these simulations. Fading is also modeled multi-variate Rician [9], [10], [19], or more general composite models [12], [13], [15], [31], [40], [50], [52].

# 6. UAV SPATIAL STRUCTURES AT 5 GHZ

This section examines three vertical $y$-$z$ "slices" of the UAV channels to understand how the $y$-tracks of the preceding section behave as a function of the UAV height. The UAV broadcasts from locations

$$\mathbf{r}_T = \begin{bmatrix} x_T \\ y_T \\ z_T \end{bmatrix} \quad \begin{cases} x_T = 25, -50, -100 \text{ [m]}, \\ 0 \leq y_T \leq 300 \text{ [m]}, \\ 30 \leq z_T \leq 225 \text{ [m]}, \end{cases}$$

through the $0.2'' \times 0.2''$ patch antenna to the street-level receiver at

$$\mathbf{r}_R = \begin{bmatrix} 150 \\ 100 \\ 2 \end{bmatrix} \quad \text{[m]}$$

where the receiver employs a half-wavelength vertical dipole. Shadowing by the city's building has a significant effect on the channels. Figure 38 illustrates the shadowing geometry. For a receiver located a distance $d_R$ from a building $h_B$, that building's shadow height $h_A$ linearly increases as the aircraft's distance increases from the building:

$$h_A = (d_A + d_B)\frac{h_B}{d_B}. \tag{11}$$

Section 6.1 verifies the shadowing is caused by the buildings and follows the linear model of Equation11. Section 6.2 identifies Rician fading in a stationary region common to all slices.

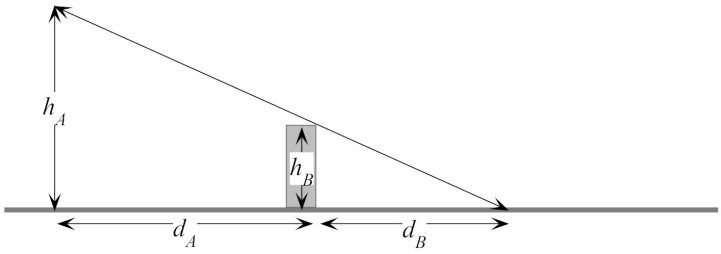


Figure 38. Linear shadowing geometry.

## 6.1 VERTICAL SLICES

Figure 39 reports the resulting channels in the $y$-$z$ plane or the slice at $x_T = +25$ meters. As in the preceding track simulations, the UAV is aligned with the $y$-axis and flying level parallel to the $y$-axis. Figure 40 puts this slice in the city to link the UAV channels to the 3-D geometry. This vertical slice explains the fading in the narrowband channels at 50, 100, and 200 meters height (See Figures 29, 32, 36). The vertical slice shows that the buildings cause multiple shadowing in the first part of the track ($10 < y_T < 60$ m) before blending into the null of the antenna pattern.

Figures 41 and 42 move the slice down the $x$-axis to $x_T = -50$ meters. The blockage by buildings increases and the power level decreases. Figures 43 and 44 slices the UAV channel at $x_T = -100$ meters. The increase in the building shadowing verifies the linear shadow geometry of Figure 38. All these slices show that once the UAV null passes the receiver at $y_T = 100$ meters, the shadowing caused by the building decreases and the remaining interference resembles the classic two-ray pattern.

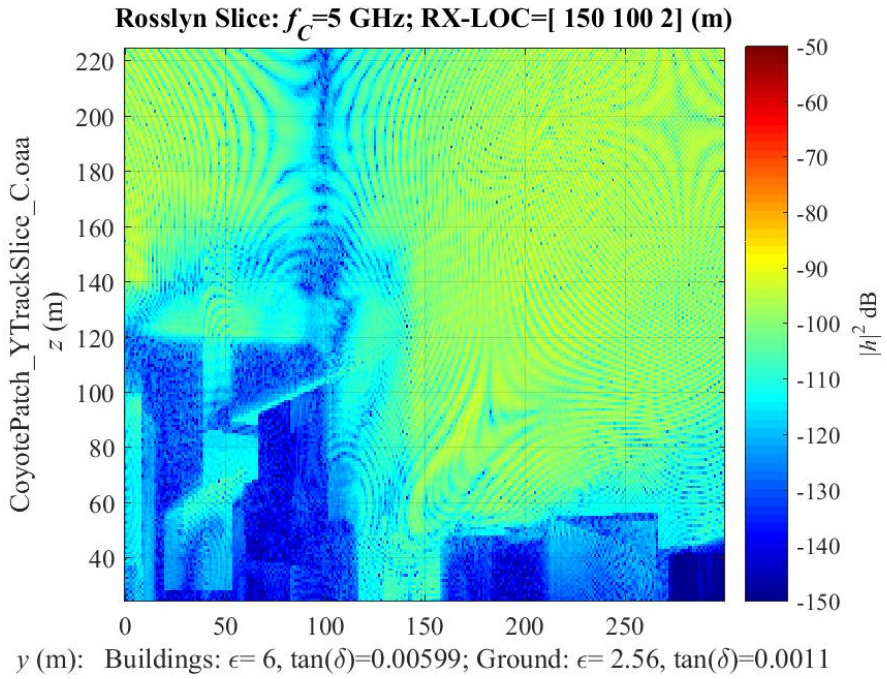


Figure 39. Narrowband channels from the UAV to the street-level receiver; sliced at $x_T = 25$ meters.

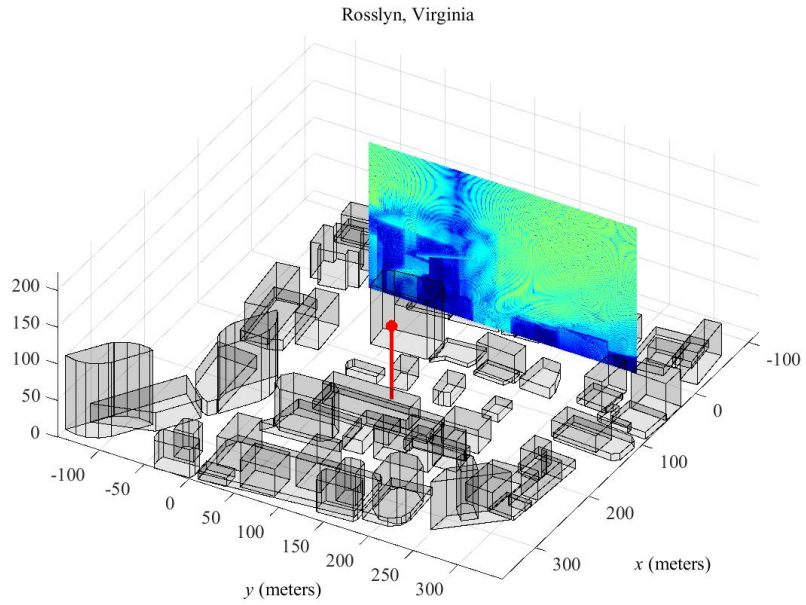


Figure 40. Narrowband UAV channel sliced at $x_T = 25$ m placed in the city; the red stem locates the street-level receiver.

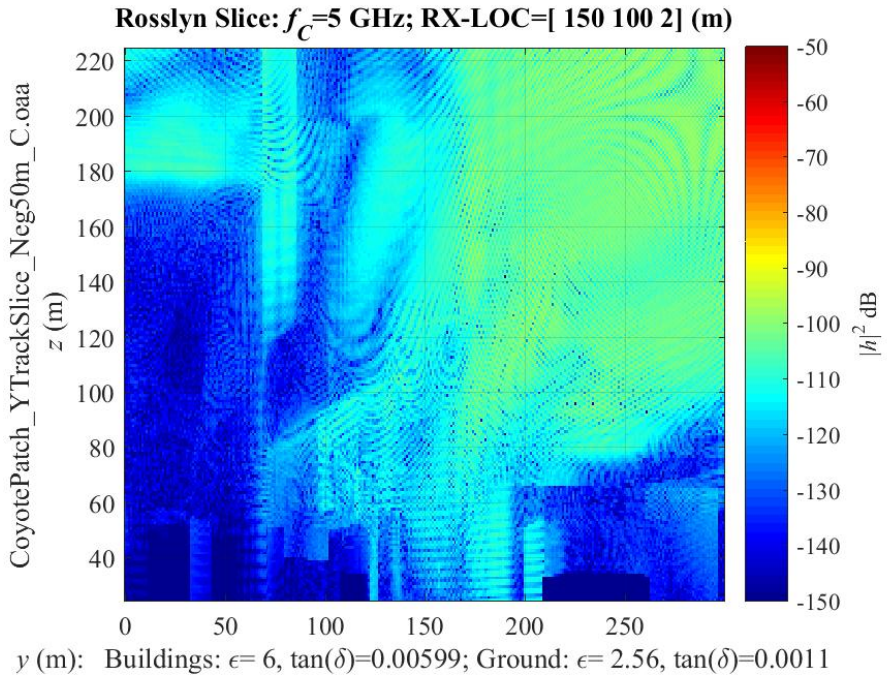


Figure 41. Narrowband channels from the UAV to the street-level receiver; sliced at $x_T = -50$ meters.

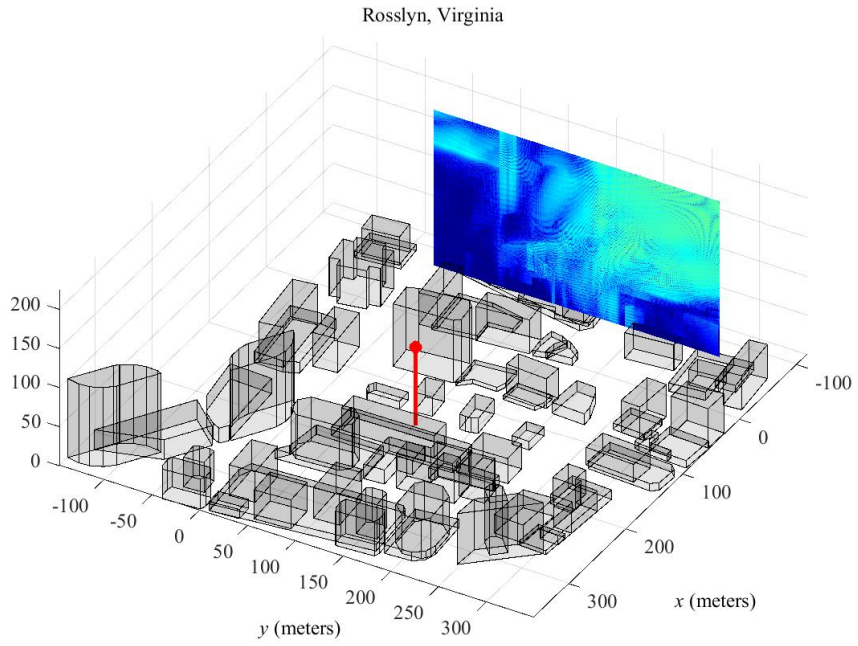


Figure 42. Narrowband UAV channel sliced at $x_T = -50$ m placed in the city; the red stem locates the street-level receiver.

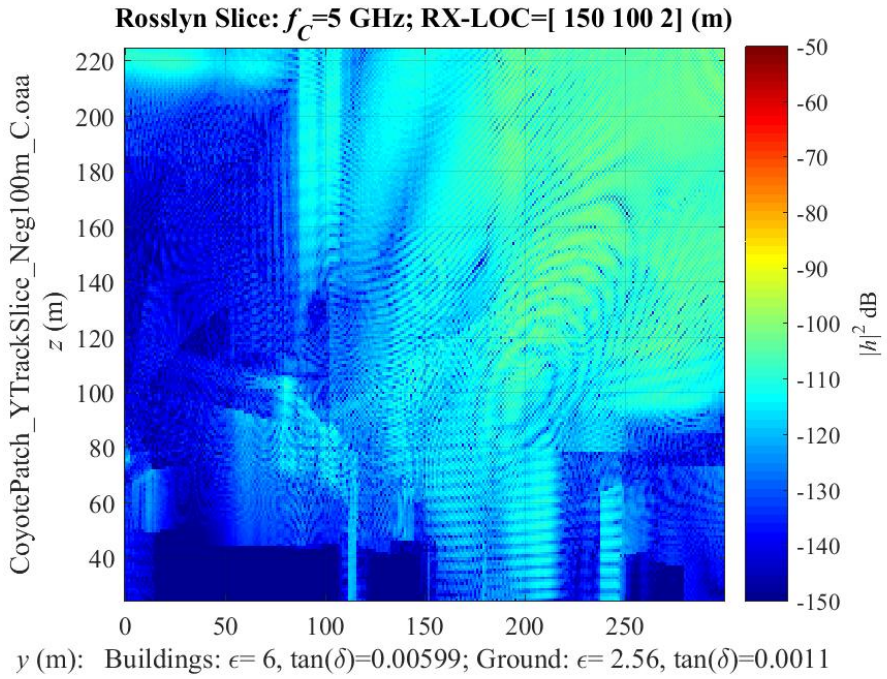


Figure 43. Narrowband channels from the UAV to the street-level receiver; sliced at $x_T = -100$ meters.

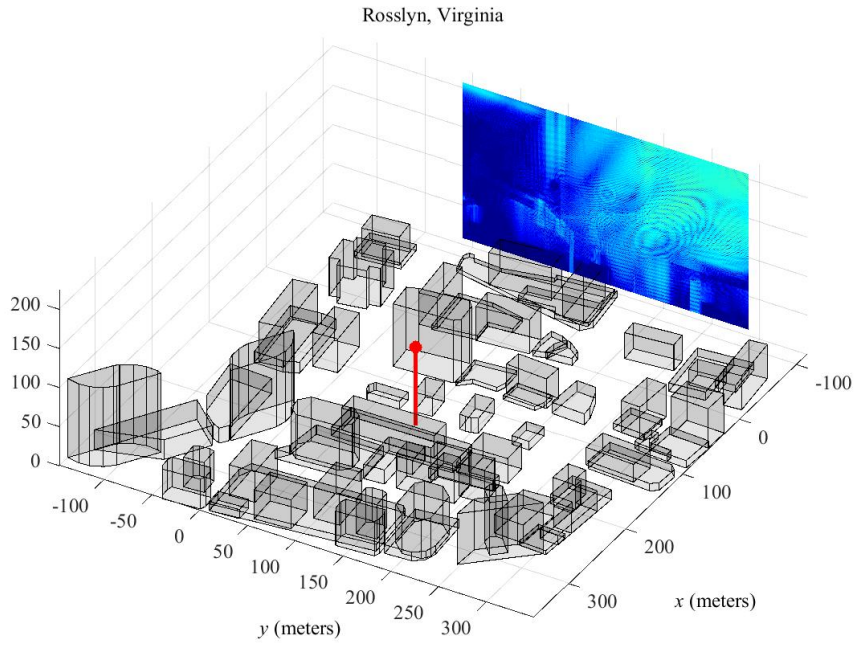


Figure 44. Narrowband UAV channel sliced at $x_T = -100$ m placed in the city; the red stem locates the street-level receiver.

### 6.2 STATIONARY FADING REGION

There is a region where the multipath is relatively stationary across all slices:

$$\begin{cases} 200 < y_T < 300 \\ 100 < z_T < 220 \end{cases} \quad \text{[meters]}.$$

This region does not show the blockage and heavy shadowing caused by the buildings and should be amenable to fading identification. The preceding section shows that a credible model of the fading has the form

$$h_{\mathrm{NB}}(x_T; y_T, z_T, \tau) = \{h_1(x_T; y_T, z_T) + h_2(x_T; y_T, z_T)\} \ \delta(\tau - \tau_0), \tag{12}$$

where $h_1$ and $h_2$ are Two-Ray Rician. This fading confounds the standard Goodness-of-Fit tests and shows a gap in fading identification. Figure 45 presents the histograms of the narrowband UAV channels over the stationary region in the first column. The second column presents Goodness-of-Fit tests in this region and identifies Rician fading with increasing $x_T$. However, the wideband analysis of Section 5 demonstrated this multipath fading is well-modeled by a shadowed Two-Ray Rician fading processes. Thus, the Goodness-of-Fit tests are revealed to be data-sensitive and best employed with a physical model.

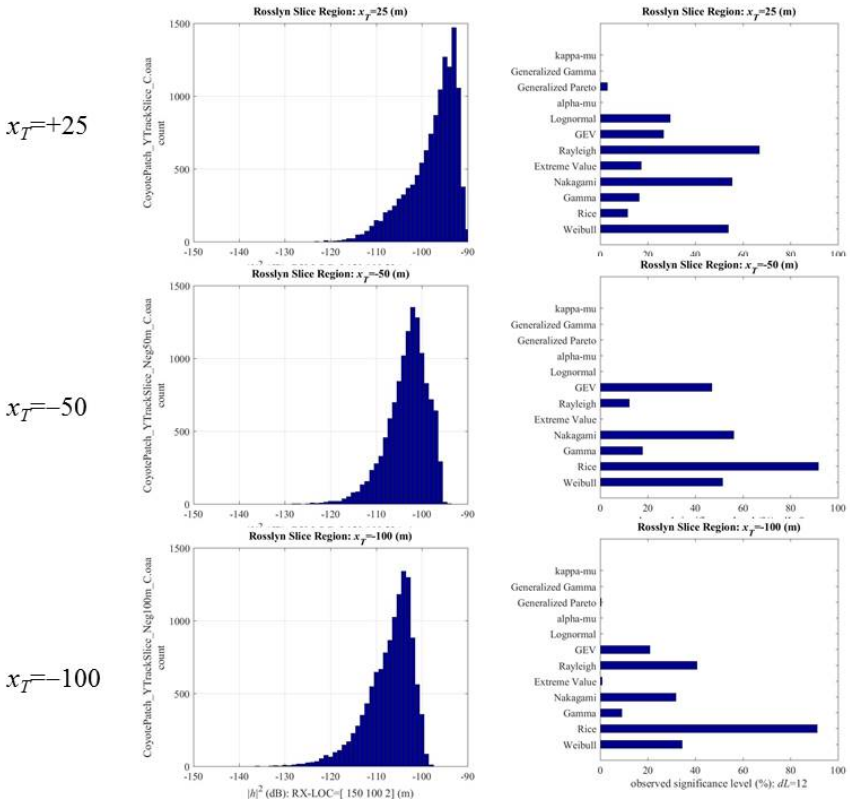


Figure 45. Histograms and Goodness-of-Fit tests of the narrowband UAV channels over the stationary region $200 < y_T < 300$, $100 < z_T < 220$ meters.

### 6.3 SUMMARY

Although single-track analysis is common in vehicular channel modeling, greater insight is obtained by putting these tracks in the context of an *ensemble of tracks*. This section shows that the shadowing geometry of the slices explains the blockage and shadowing of the individual tracks.

# 7. UAV AS A RELAY

This simulation assesses the performance shift that a UAV relay channel delivers over a ground-to-ground channel. Section 7.1 sets out the two ground nodes and computes the ground-to-ground channel gain of $-151$ dB. Section 7.2 estimates the up-link coverage of both nodes. The smallest relay gain over the coverage area is $-117$ dB. This relay gain of 34 dB over the ground-to-ground link is consistent with the average relay gain of 30 dB obtained in the first report [17]. Section 7.3 works a simple relay in urban noise to estimate the throughput gain of relay channel over the ground-to-ground channel. Section 7.4 summarizes the comparisons between the UAV relay and the ground-to-ground channel.

## 7.1 GROUND-TO-GROUND LINK

Figure 46 illustrates the two-node simulation. Two street-level nodes operate at $f_C = 5$ GHz and employ half-wavelength vertical dipoles.

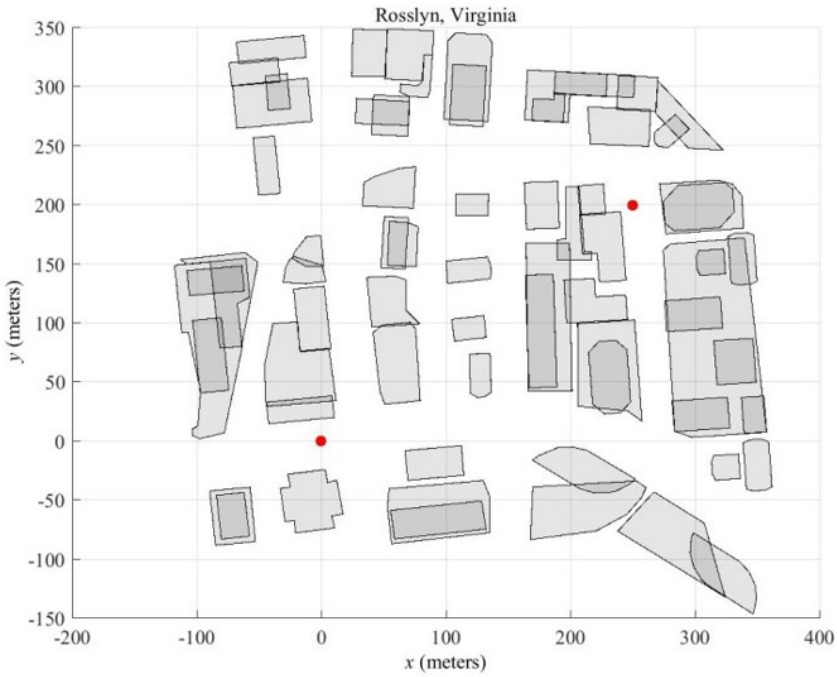


Figure 46. Top view of Node 1 and Node 2.

The channel linking Node 1 and Node 2 is computed by NEC-BSC to be

$$|h(f_C; \mathbf{r}_1, \mathbf{r}_2)|^2 = -151 \quad \text{[dB]}.$$

The flat urban noise model across a $f_B = 200$ MHz band is [26]

$$p_N = -121 \quad \text{[dBW]}.$$

An upper bound on the throughput for this channel is [22, Eq. 4.5]:

$$R_b = f_B \cdot \log_2 \left(1 + |h|^2 \frac{p_T}{p_N}\right) \quad \text{[Mbps]},$$

where $p_T$ is the transmitter's power. Figure 47 plots this upper bound $R_b$ as a function of transmit power $p_T$. The next sections compare this Ground-to-Ground channel to the UAV relay channel between Node 1 and Node 2.

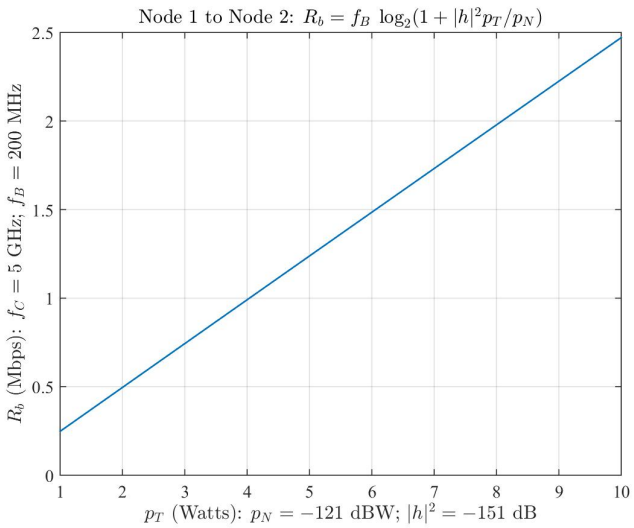


Figure 47. Throughput versus power for the Ground-to-Ground link between Node 1 and Node 2; flat urban noise over the 200-MHz bandwidth at 5 GHz.

### 7.2 GROUND-TO-UAV LINKS

Figure 48 shows the channels from each node to the UAV operating at 150 meters height and aligned parallel to the $y$-axis. Both channels show the characteristic side nulls directly over each transceiver. Node 1 has the smallest average channel gain of approximately $-113$ dB whereas the Ground-to-Ground link has a gain of $-151$ dB. Although relay systems can exploit this difference of approximately 43 dB, especially by reducing RF emissions from the nodes, not all UAV positions deliver this gain.

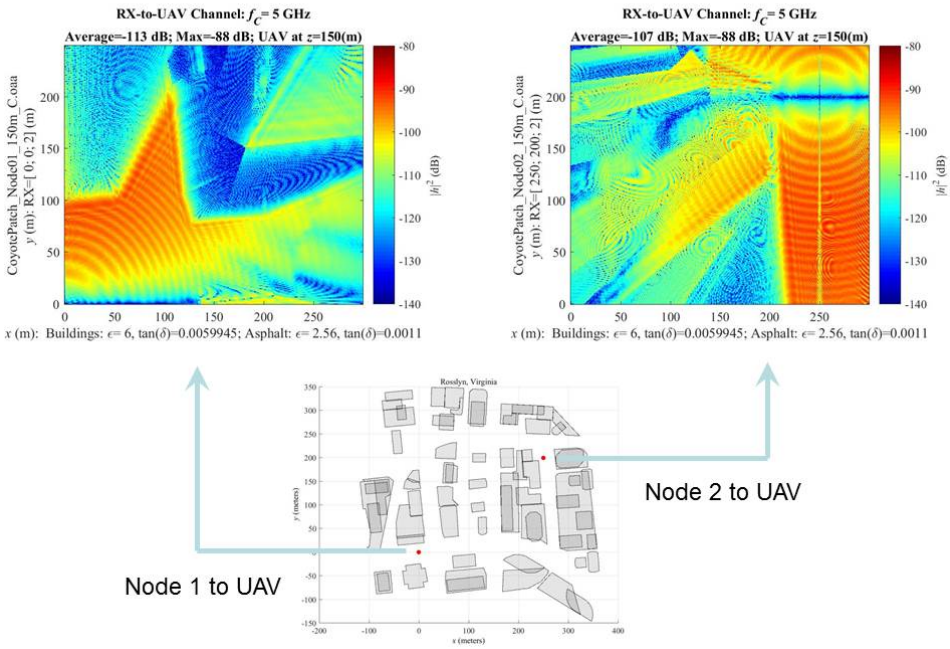


Figure 48. Node-to-UAV channels at 5 GHz.

Figure 49 quantifies this spatially varying UAV channel by plotting the weakest of the two UAV channels. The nulls are visible at both nodes. This plot provides an upper bound for any relay system by requiring the up- and down-links to overcome the weakest channel. Figure 50 is a histogram of these weakest channels showing a close concentration around $-117$ dB and a long tail rolling off to $-170$ dB.

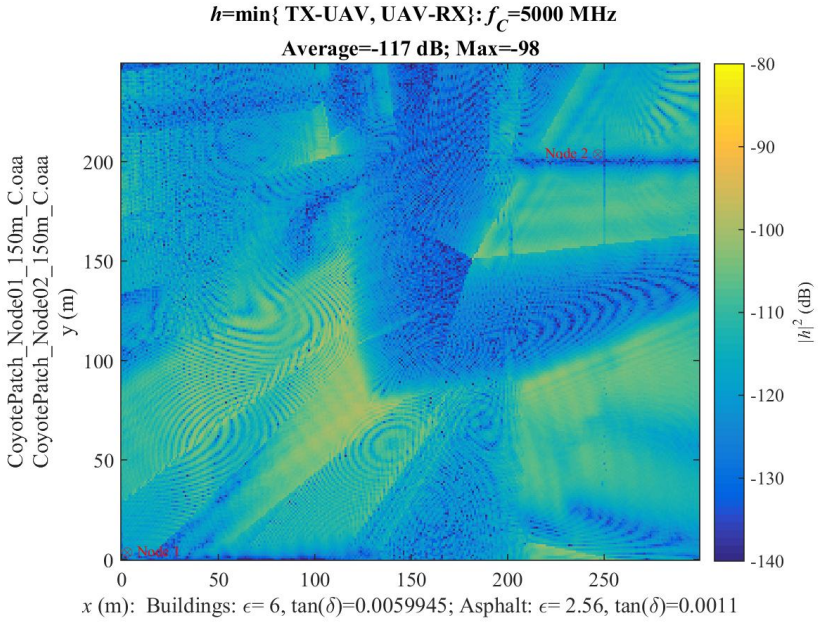


Figure 49. Weakest Node-to-UAV channels at 5 GHz; UAV flies at 150 m height; aligned with the $y$-axis.

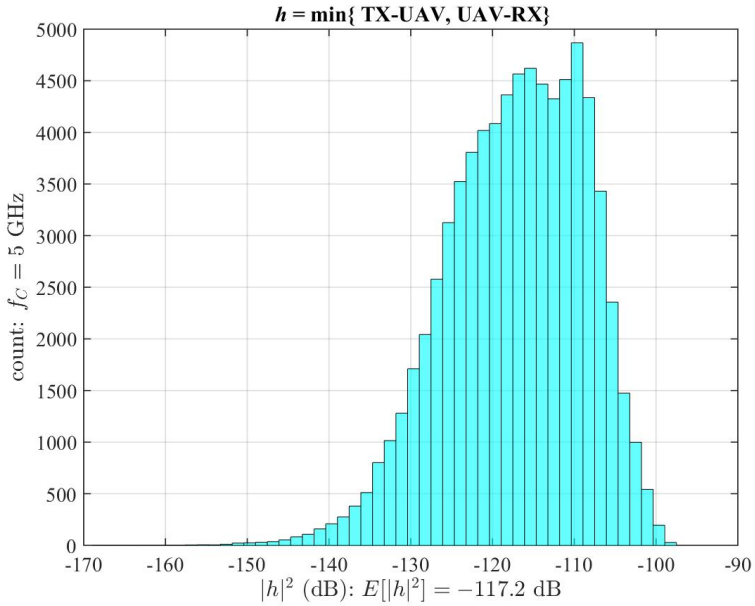


Figure 50. Histogram of the Weakest Node-to-UAV channels at 5 GHz.

### 7.3 A SIMPLE RELAY

Any relay scheme assumes wireless power control, even if the power allocation is set at the outset. A simple power allocation equally divides the total relay power $p_\Sigma$ between the transmitting node's power $p_T$ and the UAV's transmitting $p_{\rm UAV}$:

$$p_\Sigma = p_T + p_{\rm UAV}; \quad p_T, p_{\rm UAV} = p_\Sigma/2 \quad \text{[Watts]}.$$

The associated Shannon rate for this UAV relay—not accounting for latency—is computed at each UAV position using the smallest gain $h_{\rm MIN}$ of the up-link and down-link:

$$R_b(\mathbf{r}_{\rm UAV}) = f_B \cdot \log_2\left(1 + |h_{\rm MIN}(\mathbf{r}_{\rm UAV})|^2 \frac{p_\Sigma/2}{p_N}\right) \quad \text{[Mbps]}.$$

Figure 51 is a histogram of this Shannon rate for for $p_\Sigma = 10$ Watts. At 10 Watts, the Ground-to-Ground link delivers approximately 2.5 Mbps. In comparison, the UAV relay at 10 Watts delivers an average 795 Mbps and exceeds 25 Mbps over 98% of the time.

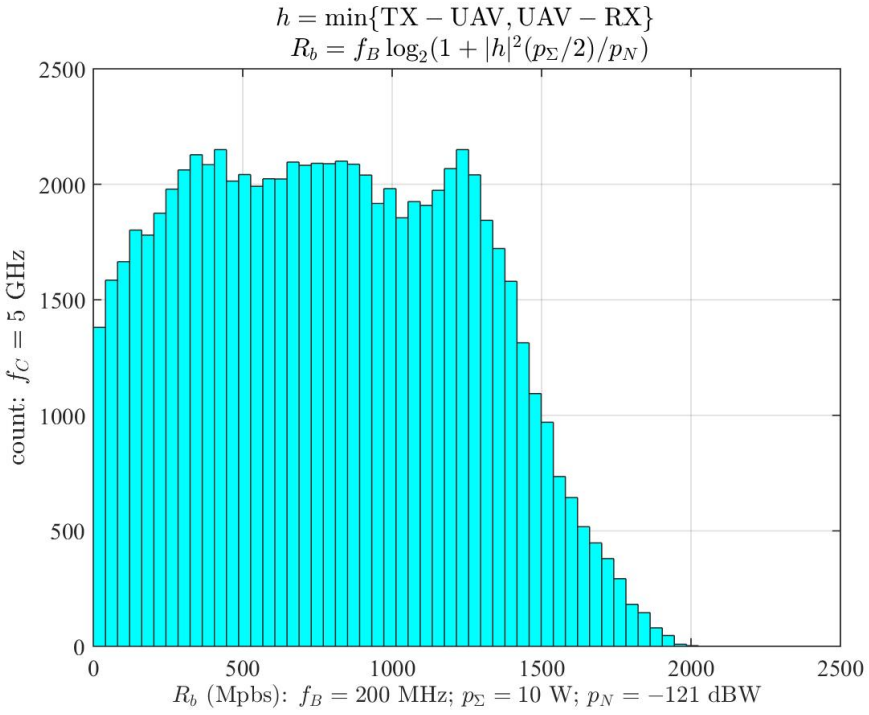


Figure 51. UAV relay rate at 150 meters altitude; $f_B = 200$ MHz; $p_\Sigma = 10$ W.

Figure 52 is a histogram of Shannon rate at $p_\Sigma = 1$ Watt. The UAV relay delivers an average 332 Mbps and exceeds 5 Mbps 98% of the time. Figure 47 reports the Ground-to-Ground link delivers approximately 0.5 Mbps at 1 Watt.

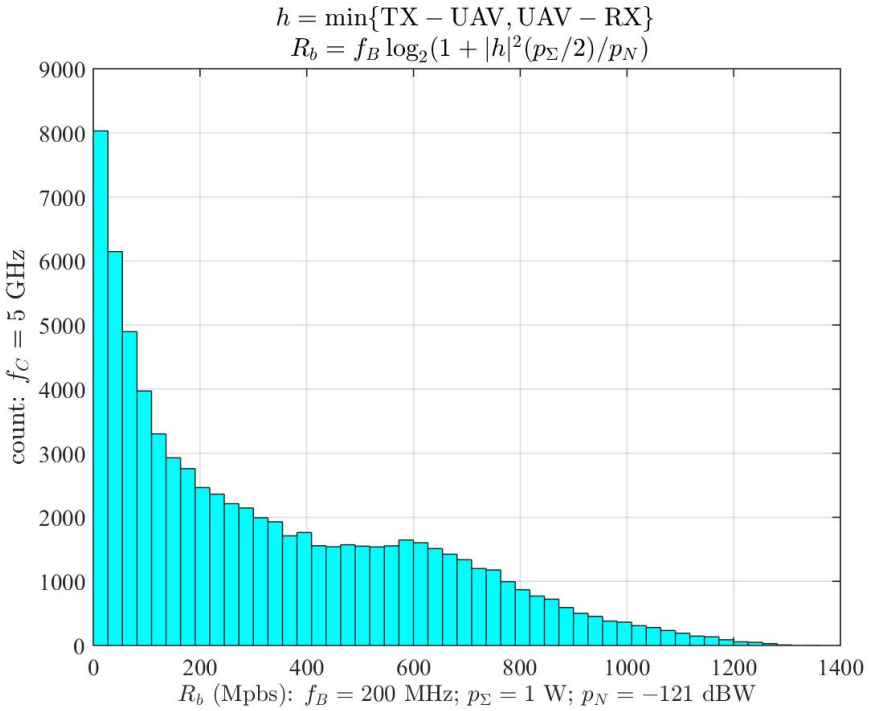


Figure 52. UAV relay rate at 150 meters altitude; $f_B = 200$ MHz; $p_\Sigma = 1$ W.

### 7.4 SUMMARY

Table 5 compares the Ground-to-Ground throughput to the UAV relay operating at 150 meters height over the two ground nodes. The Ground-to-Ground channel is stationary so that throughput is only a function of the transmit power (See Figure 47). The UAV relay channel varies with position so that UAV throughput exhibits the distributions in Figures 51 and 52. Although the average UAV throughput exceeds the Ground-to-Ground throughput, a better measure of UAV performance is the throughput exceeded by 98% of the UAV relay channels. Table 5 shows that the UAV relay, using only the simplest wireless power control, delivers $\times 10$ throughput over the ground link at 98% of the UAV locations. More advanced wireless power control algorithms could trade the substantial gain in the UAV relay channel to reduce power while maintaining an acceptable dropout rate.

Table 5. Comparing the Ground-to-Ground Channel to the UAV Relay Channel using equal power on up- and down-link; UAV at 150 meters altitude; 5 GHz with a 200-MHz bandwidth.

| Power | Ground-to-Gound | Relay Average | Relay 98% |
|---|---|---|---|
| 10 Watts | 2.5 Mbps | 795 Mbps | 25 Mbps |
| 1 Watt | 0.5 Mbps | 332 Mbps | 5 Mbps |

Table 5 only compares the channels using Node 1 and Node 2 at their fixed locations (See Figure 46) while the UAV loiters at 150 meters height. Therefore, an excellent point-of-departure for future comparisons is assessing the UAV relay channels over ground-to-ground channels while varying node locations and UAV height. Finally, Table 5 only reports throughput. Latency is omitted and the effect of channel dropouts is omitted. Latency and dropout effects are specific to the radio, waveform, and application. Simulations encompassing these effects could still employ these channels.

# 8. PATH-LOSS MODELING

NEC-BSC models of the wireless channels between the UAV's position to street-level radio nodes. These channel ensembles capture both path loss and fading and are suitable for porting into network emulators such as the *Extendable Mobile Ad-hoc Network Emulator (EMANE)* [21]. More abstract wireless channel modeling processes these channel ensembles to produce general path-loss models—without fading. This section converts several NEC-BSC simulations into the European *Cooperation in the Field of Scientific and Technical Research (COST)* framework. Although the UAV channels are simulated at 5 GHz while the COST 231 Models are limited to 2 GHz, the positive result is that the COST 231 still provide bounds for the simulated UAV channel gains. These bounds are useful for link budgets but cannot model channel fading effects.

## 8.1 COST MODELS

COST introduced several mobile wireless models starting in the mid 1980's to establish reference models for path loss estimation. An excellent review of the COST model histories is found in [14]. The *COST 231 Hata* model is a basic model of path loss [48, Eq. 2.238]

$$L_p^{\mathrm{CH}} = A + B\log_{10}(d) + 20\log_{10}(f_C) + C \quad [\mathrm{dB}], \tag{13}$$

employing the following path-loss functions parameterized in Table 6:

$$\begin{aligned} A &= 46.3 + 33.9\log_{10}(f_C) - 13.82\log_{10}(h_b) + a(h_m) \\ B &= 44.9 - 6.55\log_{10}(h_b) \\ C &= \begin{cases} 0 & \text{medium city or suburban areas; moderate tree density} \\ 3 & \text{metropolitan centers} \end{cases} . \end{aligned}$$

Stüber observes that this model [48, Section 5.2.1] "should not be used to predict path loss in urban canyons" nor "used for smaller ranges" ($d < 1$ km).

Table 6. COST 231 Hata Parameters.

| Parameter | Description | Range |
|---|---|---|
| $f_C$ | $1.5 \le f_C \le 2.0$ (GHz) | Carrier frequency |
| $d$ | $1 \le d \le 20$ (km) | Ground range |
| $h_b$ | $30 \le h_b \le 10$ (m) | Main station antenna height |
| $h_m$ | $1 \le h_m \le 10$ (m) | Base station antenna height |

The *COST 231 Walfisch-Ikegami* model generalizes mobile wireless loss to street canyons by modeling LoS and NLoS path loss [48, Section 5.2.2], [14]. An assessment of the COST 231 Walfisch-Ikegami modeling over-the-air measurements at 3.5 GHz showed that this model produced an upper bound on the signal power [6]. The *LoS propagation* in the COST 231 Walfisch-Ikegami model is [48, Eq. 2.239]

$$L_p^{\mathrm{CWI}} = 42.6 + 26\log_{10}(d) + 20\log_{10}(f_C) \quad [\mathrm{dB}] \tag{14}$$

with the model parameters delimited by Table 7. Figure 53 illustrates the geometry for the non-LoS model. The *non-LoS propagation* in the COST 231 Walfisch-Ikegami model is [48, Eq. 2.240]

$$L_p = L_0 + (L_{\mathrm{rts}} + L_{\mathrm{msd}})_+ \quad [\mathrm{dB}] \tag{15}$$

that sums the "free-space loss"

$$L_0 = 32.4 + 20\log_{10}(d) + 20\log_{10}(f_C) \quad [\mathrm{dB}]$$

with $(\circ)_+$ denoting the positive part of the sum of the rooftop-to-street diffraction loss $L_{\mathrm{rts}}$ and the multi-screen diffraction loss $L_{\mathrm{msc}}$.

Table 7. COST 231 Walfish-Ikegami Parameters.

| Parameter | Description | Range |
|---|---|---|
| $f_C$ | $1.5 \le f_C \le 2.0$ (GHz) | Carrier frequency |
| $d$ | $0.02 \le d \le 5$ (km) | Ground range |
| $h_b$ | $30 \le h_b \le 200$ (m) | Main station antenna height |
| $h_m$ | $1 \le h_m \le 10$ (m) | Base station antenna height |

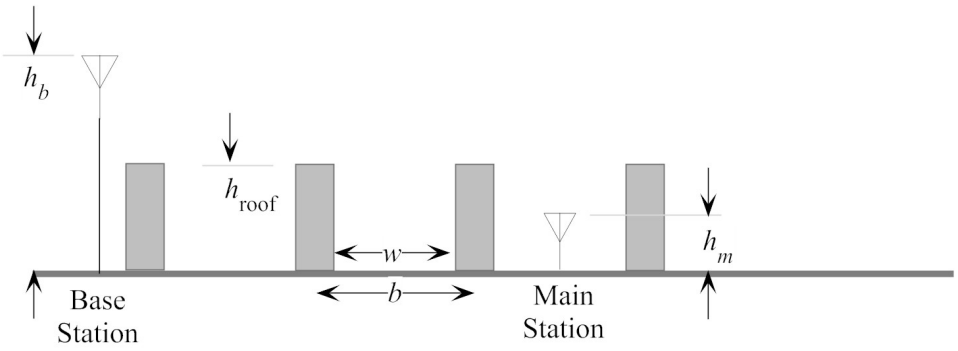


Figure 53. COST 231 Walfisch-Ikegami geometry.

Assuming the roofs are always above the main station ($h_{\text{roof}} > h_m$), the rooftop-to-street diffraction loss is [48, Eq. 2.241]

$$L_{\text{rts}} = -16.9 - 10\log_{10}(w) + 10\log_{10}(f_C) + 20\log_{10}(h_{\text{roof}} - h_m) + L_{\text{ori}}(\phi) \quad [\text{dB}],$$

where the orientation loss [48, Eq. 2.242]

$$L_{\text{ori}}(\phi_{\text{ori}}) = \begin{cases} -10 + 0.354\phi_{\text{ori}} & 0^\circ \le \phi_{\text{ori}} \le 35^\circ \\ 2.5 + 0.075(\phi_{\text{ori}} - 35^\circ) & 35^\circ \le \phi_{\text{ori}} \le 35^\circ \\ 4.0 - 0.114(\phi_{\text{ori}} - 55^\circ) & 55^\circ \le \phi_{\text{ori}} \le 90^\circ \end{cases}$$

is a function of the angle $\phi_{\text{ori}}$ between the road orientation and the direct radio path. Assuming the UAV is always above the roofs ($h_b > h_{\text{roof}}$), the multi-screen diffraction loss is [48, Eq. 2.243]

$$L_{\text{msd}} = L_{\text{bsh}} + k_a + k_d\log_{10}(d) + k_f\log_{10}(f_C) - 9\log_{10}(b) \quad [\text{dB}],$$

where base station shadowing loss is [48, Eq. 2.244]

$$L_{\text{bsh}} = -18\log_{10}(1 + (h_b - h_{\text{roof}})) \quad [\text{dB}],$$

when the base station is above the rooftops sets [48, Eqs. 2.245, 2.246, 2.247] $k_a = 54$, $k_d = 18$, and

$$k_f = -4 + (f_C/925 - 1)\begin{cases} 0.7 & \text{medium city} \\ 1.5 & \text{metropolitan area} \end{cases}.$$

Stüber observes that this model [48, Section 5.2.2] "works best for $h_b \gg h_{\text{roof}}$" and "is poor for $h_b \ll h_{\text{roof}}$ because ... wave guiding in street canyons and diffraction at street corners" is not in the model. The remainder of this section applies the LoS and non-LoS models to the UAV-to-street channels.

### 8.2 UAV-TO-STREET MODELS

Figure 54 shows several coverage plots. Each coverage plot holds the UAV over $x_T = 100$ and $y_T = 100$ meters while varying the UAV height $z_T = 50$, 150 200 meters and orientation $\phi_T = 0°$, $30°$ and $60°$. These plots show that antenna null does increase with UAV height, as previously observed in Section 4, this null has a relevantly small effect on the overall coverage. Likewise, the UAV orientation has a relatively small effect on the coverage. However, UAV height shows a significant threshold between 50 and 100 meters where the lower heights exhibit more shadowing.

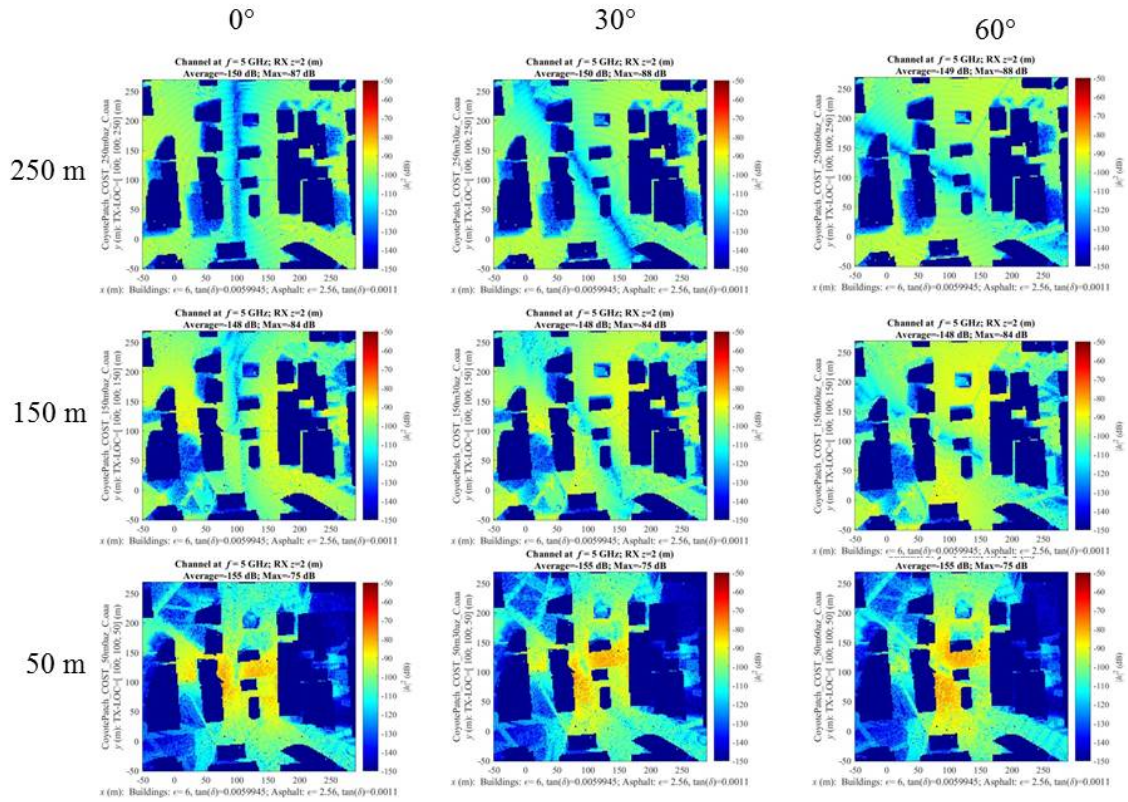


Figure 54. UAV coverage at 5 GHz to street-level receivers as a function of UAV height $z_T = 50$, 150, and 250 meters and azimuth $\phi_T = 0°$, $30°$, and $60°$.

Figure 55 confirms these observations by plotting the corresponding histograms of the channel gain. The UAV orientation has negligible effect in comparison to the effects caused by UAV height. The histograms above 50 meters show a bimodal distribution with the LoS components creating a narrow peak for height gain and the non-LoS components filling out the "fat" tail over the low channel gains. Following the COST modeling that distinguishes between the LoS and the non-LoS, the channel gain is fitted with a Gaussian Mixture Model (GMM) of two mixtures. The fit is excellent above the 50-meter height and confirms the COST approach. The GMM fit is reported on each plot. Table 8 reports the percentage of the LoS component of the GMM. The LoS component is approximately 61% of the channel gain above 50 meters height. Table 9 reports the mean power in the LoS component. Above 50 meters height, the LoS power is $-99$ dB. More details of these LoS components are described in the next figure.

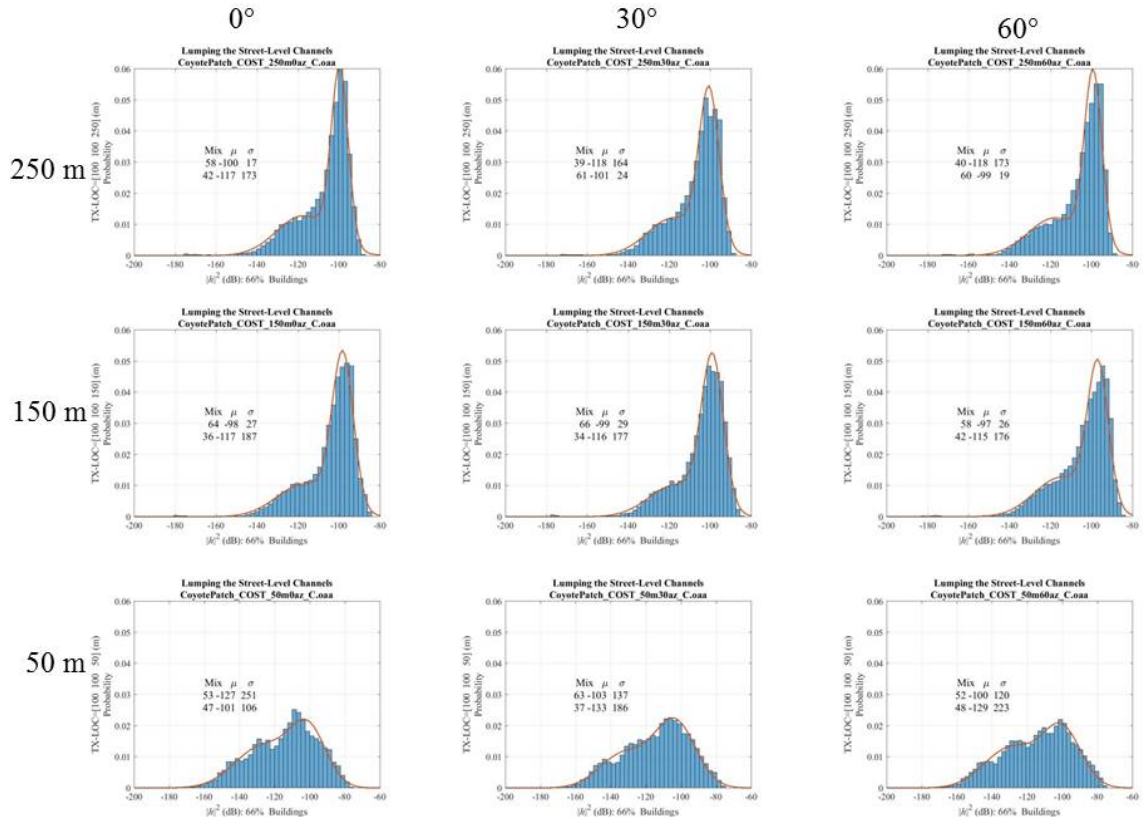


Figure 55. Histograms of the channel gain as a function of UAV height and azimuth; GMM estimates are the solid lines and tabulated on the plots.

Table 8. LoS percentage in the GMM.

| **LoS Mixture** | $\varphi_T$=0° | $\varphi_T$=30° | $\varphi_T$=60° |
|---|---|---|---|
| $z_T$=250 m | 58% | 61% | 60% |
| $z_T$=150 m | 64% | 66% | 58% |
| $z_T$=50 m | 47% | 63% | 52% |

Table 9. LoS power in the GMM

| LoS Mean | $\varphi_T$=0° | $\varphi_T$=30° | $\varphi_T$=60° |
|---|---|---|---|
| $z_T$=250 m | −100 dB | −101 dB | −99 dB |
| $z_T$=150 m | −98 dB | −99 dB | −97 dB |
| $z_T$=50 m | −101 dB | −103 dB | −100 dB |

Figure 56 brings these coverage plots and histograms into the COST model by plotting the 2-D histogram of channel gain $|h|^2$ and distance $d$. The vertical axis is channel gain and is the same on all plots. The horizontal axis is distance and varies with UAV height to better show the estimated 2-D distribution. The histograms are normalized to be a probability density rather than a bin count. The "No Buildings" means that the interior of the buildings is omitted from these histograms. Consistent with the previous observations, there is relatively small variation with UAV orientation. There is a relatively large variation the LoS component below 50-meters height.

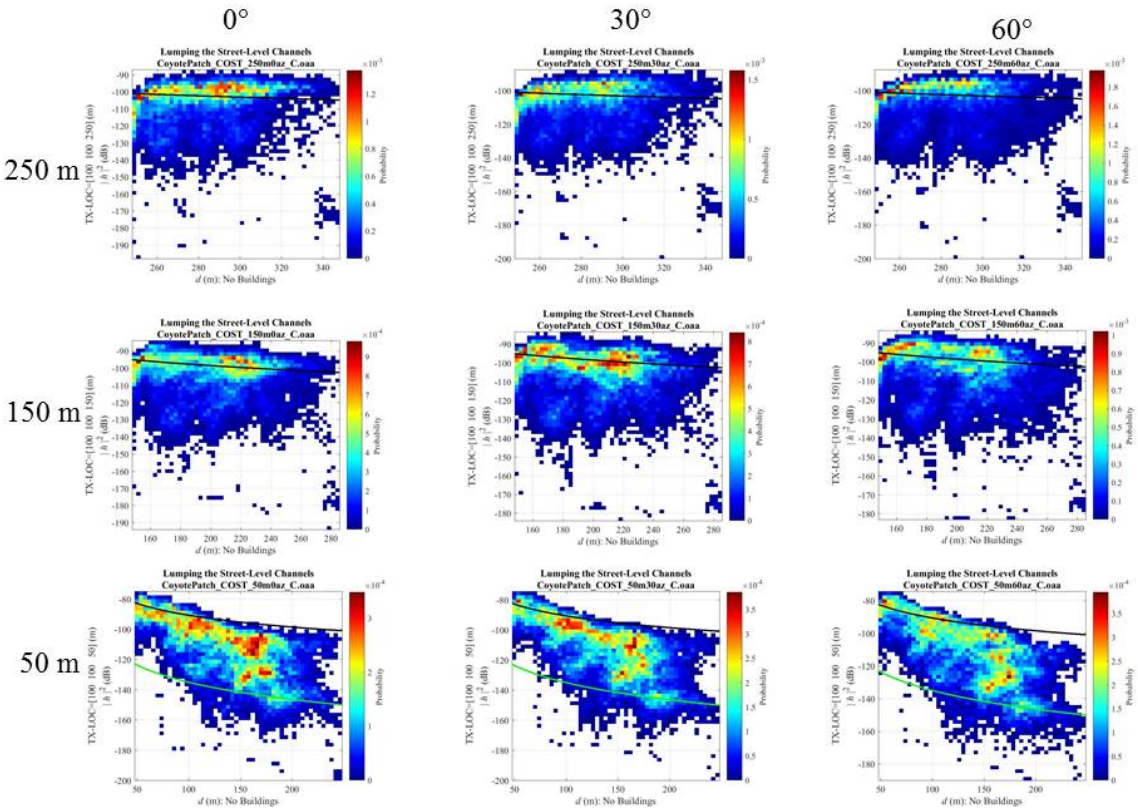


Figure 56. Coverage distributions as a function of UAV height and azimuth; solid lines are the COST 218 Walfisch-Ikegami LoS and non-LoS bounds.

The COST 231 Walfisch-Ikegami models are also plotted. The black line on distributions is the LoS model of Equation 14. The fit at $z_T = 150$ meters is remarkable and provides the interpretation that the LoS model is describing the mean of the channel gain (See Figure 55). The LoS fit at $z_T = 50$ meters verifies the observation, obtained from over-the-air measurements, that the LoS model is an upper bound on the channel gain when the base station is relatively low with respect to the roofs [6].

The green line on the 50-meter row in Figure 56 is the non-LoS model of Equation 15. This non-LoS model provides remarkable lower bound. The street width ($w$) and the building separation ($b$) are not well-defined for this heterogeneous urban area (See Figure 24), and the roof heights ($h_{\text{roof}}$) range from 11 to 100 meters with substantial variations in roof area (See Figure 15). Despite the gross

approximations $w \approx 29$ meters, $b \approx 72$ meters, $h_{\text{roof}} \approx 30$ meters, the non-LoS model provided a relatively "tight" lower bound.

The LoS for $z_T = 250$ meters is problematic. First, this height exceeds the base station height ($h_b$) bounds in Table 7. Second, the simulated channel shows the null of the street-level antenna at the minimal distances. These vertical dipoles have a null pointing straight up that limits channel gain directly below the UAV. Moving out from under the UAV actually boosts channel gain. The simulations show this effect whereas the LoS model predicts decreasing channel gain with increasing distance. The COST models do not include antenna patterns but apparently make the implicit assumptions that both the main and base stations use vertical dipoles. The assumption of ground-to-ground channels precludes the main station being directly below the base station. Thus, UAV operating over ground forces requires an extension to the COST model.

### 8.3 SUMMARY

Although the 5-GHz frequency is outside the COST domain (Table 4), the predicted LoS channel gain aligns well with the simulated mean gain at $z_T = 150$ meters. At the low end of the applicable height $z_T = 50$, the LoS and non-LoS predictions bound the channel gains, despite the fact that the city's roof height is estimated to be $h_{\text{roof}} \approx 30$ meters whereas the city's building range from 10 to 100 meters in height. Thus, this section verifies that COST modeling for this UAV provides bounds on the channel gain. These bounds are useful for link budgets but cannot model channel distributions or fading effects.

# 9. CIRCULAR TRACKS

Flying the UAV around a circular track illustrates the opportunities afforded by UAV "loitering" schemes. Section 9.1 sets out the geometry of the circular track and the street-level receiver. Section 9.2 flies the UAV around the circular track with wings are level and antenna vertical. Section 9.3 flies the UAV around the circular track with the UAV rolled at $45°$. Section 9.4 compares the fading on both tracks. Rolling the UAV points a null in UAV's antenna into the city and reduces the overall gain by 11 dB. This result is consistent with the first report that also pointed a null into the city and observed reduced channel gain [17].

## 9.1 CIRCULAR TRACK AT 400 METERS

Figure 57 is a 3-D view of the city showing the circular track of the UAV. The circular track is 400-meters in diameter, raised to a height of 200 meters, and centered at the offset origin $\mathbf{r}_0 = [100,\ 100,\ 200]^{\mathsf{T}}$ meters. One parametrization of the circular track uses the azimuth angle $\phi$ measured from this offset origin:

$$\mathbf{r}_T(\phi) = \begin{bmatrix} 100 \\ 100 \\ 200 \end{bmatrix} + 200 \begin{bmatrix} \cos(\phi) \\ \sin(\phi) \\ 0 \end{bmatrix} \quad [\mathrm{m}]. \tag{16}$$

The UAV broadcasts to a street-level receiver fixed at $x_R = 150$, $y_R = 100$ meters.

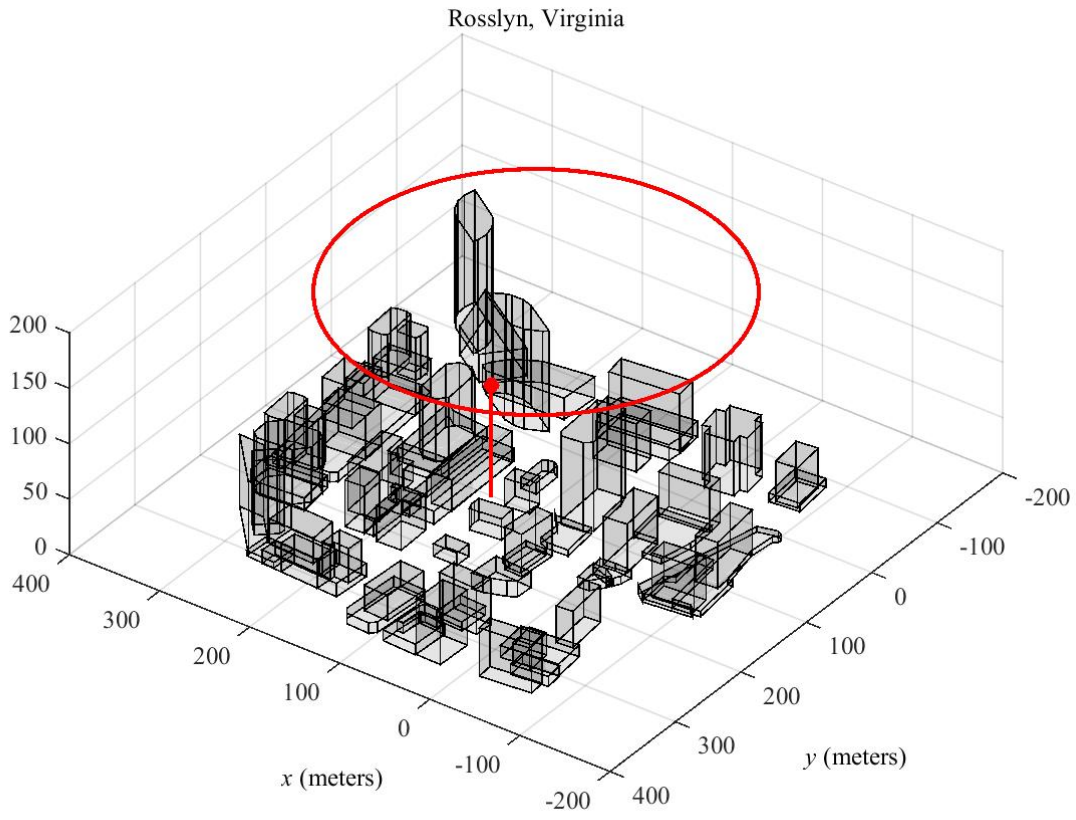


Figure 57. Circular track and the receiver; the large "thumbtack" marks the location of the street-level receiver.

Figure 58 is a top view of this geometry clarifying the relation between the circular track and the street-level receiver at location

$$\mathbf{r}_R = \begin{bmatrix} 150 \\ 100 \\ 2 \end{bmatrix} \quad [\text{m}] \tag{17}$$

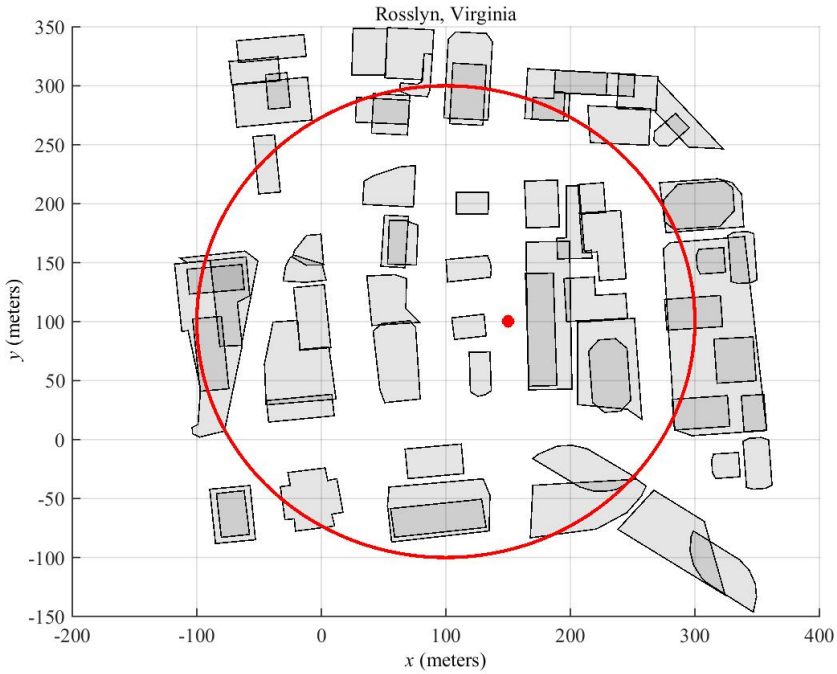


Figure 58. Top view of the circular track and the street-level receiver.

### 9.2 NO ROLL

The orientation of the UAV is determined by its location along the circular track. Referring to Figure 9, unit vector $\widehat{\mathbf{x}}$ points out the nose of the UAV and is alinged with the tangent vector to the circular track, unit vector $\widehat{\mathbf{y}}$ is parallel to the wings and is orthogonal to the track and horizontal, and $\widehat{\mathbf{z}}$ is the cross product of $\widehat{\mathbf{x}}$ and $\widehat{\mathbf{y}}$. Thus, the UAV flies the circular track with zero roll. Figure 61 shows a cross section of the UAV's track looking along the $y$-axis as the UAV has flown halfway around the circle or when $\phi = 180°$ in Equation 16.

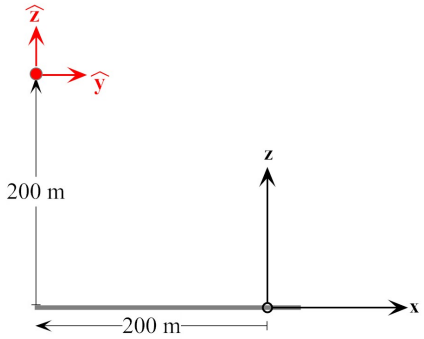


Figure 59. Vertical cross section of the circular track at azimuth $\phi = 180°$ showing the UAV's orientation; $\widehat{\mathbf{x}}$ points out of the paper.

The vertical and horizontal antenna patterns of Figures 11 and 12 orient their spherical coordinates to this local $\widehat{\mathbf{x}}$-$\widehat{\mathbf{y}}$-$\widehat{\mathbf{z}}$ coordinate system attached to the UAV. Figure 60 shows the channels from the UAV location $\mathbf{r}_T(\phi)$ in Equation 16 to the street-level receiver at $\mathbf{r}_R$ in Equation 17. This circular track should exhibit a deep null at $\phi = 180°$ similar to the deep null observed in the linear tracks (See Figure 36). The nulls in the linear tracks are caused by the null in $E_\theta$ (See Figure 11). A similar geometry holds at $\phi = 180°$ where the $E_\theta$ response is measured near the zenith angle $\theta \approx 129°$. Figure 60 registers a null at $\phi = 180°$ accompanied by the interference of the UAV structure seen in $E_\theta$. This null provides some verification that the antenna pattern is correctly integrated onto the circular track.

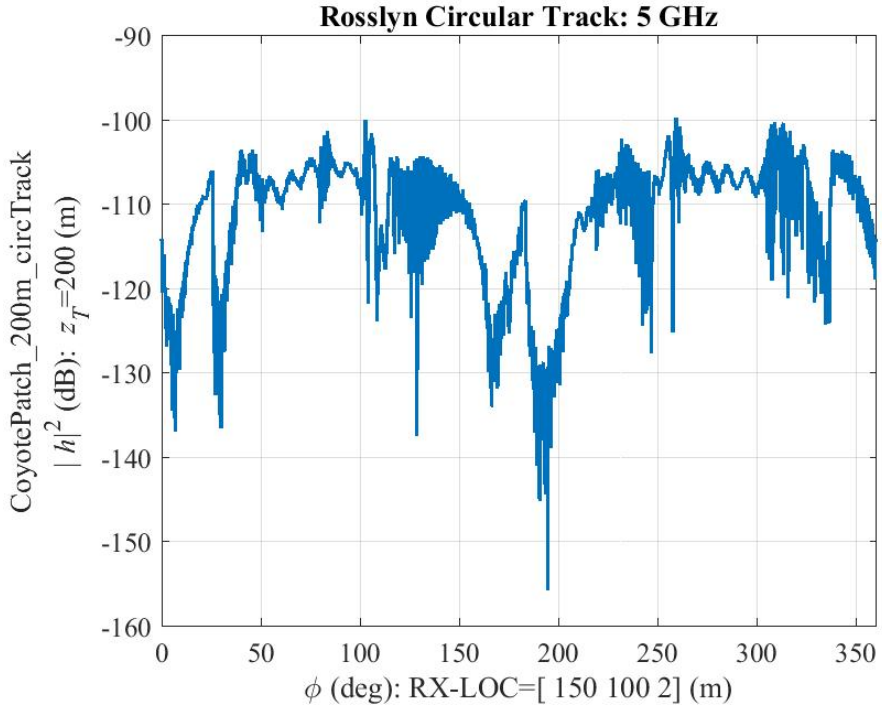


Figure 60. Channel on the circular track.

### 9.3 45° ROLL

The final simulation flies the UAV with a constant roll around the circular track. Figure 61 shows the cross section of the UAV's track viewed along the $y$ axis when the UAV has completed half the circle flying with a constant roll of $45°$. The nose or the unit vector $\widehat{\mathbf{x}}$ points out of the page. The wings or the unit vector $\widehat{\mathbf{y}}$ is orthogonal to the flight and points the ground at the center of the circle track. The unit vector $\widehat{\mathbf{z}}$ is tilted $45°$ off the $z$-axis and rotates around this axis. The vertical and horizontal antenna patterns of Figures 11 and 12 orient their spherical coordinates to this coordinate system.

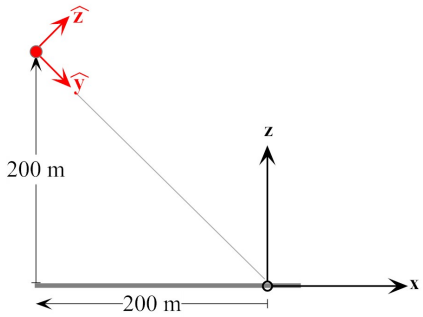


Figure 61. Vertical cross section of the circular track at azimuth $\phi = 180°$ showing the UAV flying with a constant roll of $45°$; $\widehat{\mathbf{x}}$ points out of the paper.

Figure 62 shows that rolling the UAV by $45°$ reduces the channel gain over the non-rolled channel of Figure 60. When the UAV is flying the circular track with zero roll, the antenna points at the street-level receiver with zenith $129° < \theta < 143°$ to slice the antenna patterns $\mathbf{E}_\theta$ and $\mathbf{E}_\phi$ in regions of relatively strong response. When the UAV is rolled $45°$, the antenna points at the street-level receiver with zenith $\theta \approx 90°$ or where both patterns are rolling off (See Figures 13 and 14). This shift in the gain caused by the roll provides another verification that the antenna pattern is correctly integrated onto the circular track.

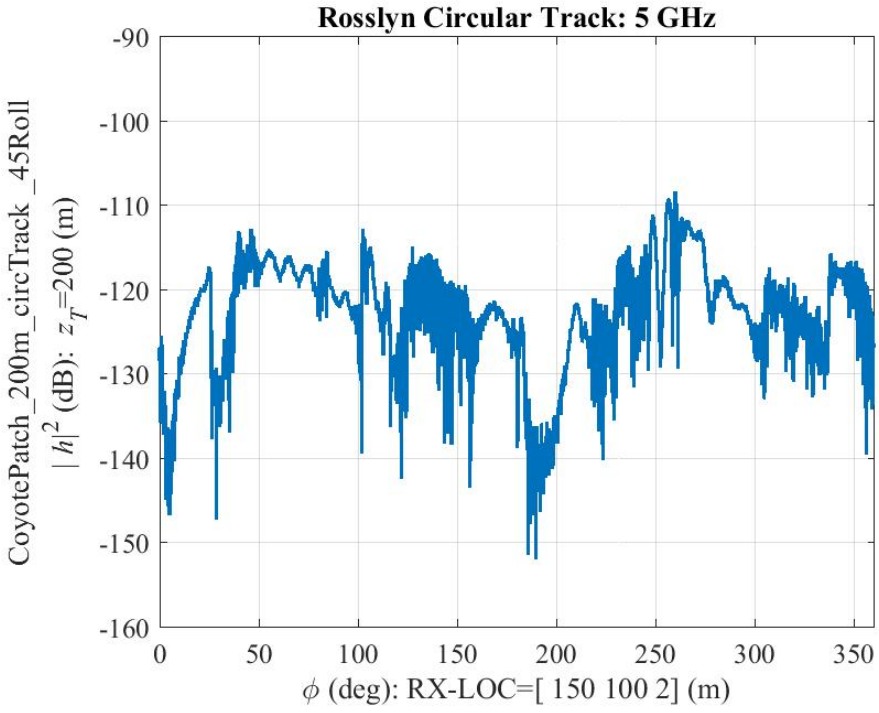


Figure 62. Channel on the circular track.

### 9.4 SUMMARY

Figure 63 compares the channel of the UAV flying horizontal to the UAV flying with the $45°$ roll. The figure shows the UAV's flat flight delivers an average of 11 dB more channel gain than over the rolled flight. This result is the opposite obtained in the first report that employed a whip antenna [17]. In that report, rolling the UAV produced a 10 dB increase over horizontal flight. Both effects are caused by the antenna patterns on the UAV. Regardless of the roll of the UAV, when the UAV flies a circular track or more complicated "loitering" pattern, a stationary ground-level receiver could "learn" the UAV channels shown in Figures 60 and 62. Once the periodic channel is known, the receiver can adapt to the rapid switching between the fading regimes.

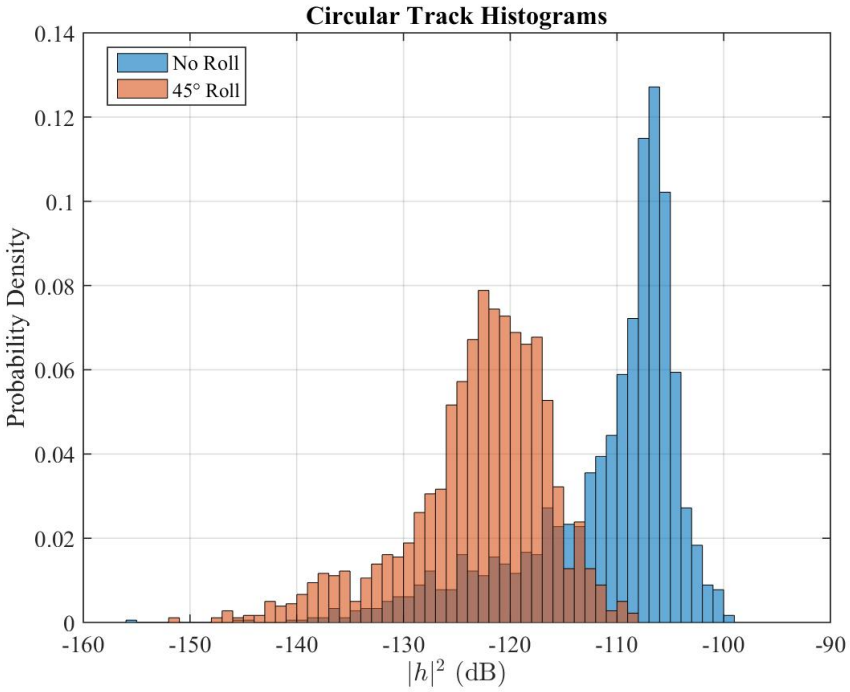


Figure 63. Comparing channels of the UAV flying horizontal to the UAV flying with a $45°$ roll.

# 10. EXTENDING THE UAV CHANNEL ANALYSIS

These UAV simulations quantify the coverage, fading and throughput of the UAV Relay channels interacting with mobile ground forces—assuming the bottom-mounted patch on the UAV, the half-wavelength vertical dipoles used by all ground-level nodes, and the operating frequency of 5 GHz. Even under these specific assumptions, general observations are obtained:

- Antenna patterns affect coverage and fading (Sections 4, 5, 6, 8, 9).
- City geometry, particularly building height, when coupled with the UAV height governs blockage and shadowing (Sections 5 and 6).
- City geometry causes abrupt switching between fading regimes as the UAV flies along its path, particularly at the lower heights or along a circular track.
- Shadowed Two-Ray Rician fading is a credible model for systems employing 1 MHz or less of bandwidth (Section 5).
- The UAV relay simultaneously increases capacity and decreases transmission power, at a cost of employing a spatially varying channel (Section 7).
- When the UAV loiters along a fixed track, stationary ground nodes can "learn" the periodic fading and adapt to the rapid switching between the fading regimes (Section 9).

Incorporating the simulated UAV channels into networking simulations where multiple street-level nodes are connected by a UAV relay is a natural next step to assess network performance [21]. However, the report quantified throughput using the Shannon bound. Credible network simulations quantify throughput at the packet level when the radios are contending against the fading and latency on the up- and down links. This gap between theory and the "packet" counting in the network simulation provides an engineering assessment of the performance of the UAV as a relay. Because UAV movement increases channel variations, the network simulations also set a bound on UAV motion (i.e., UAV hovering versus flying a pattern). The following recommendations start with the UAV channel models, move to UAV antennas, and conclude with the UAV relay tested in network simulations to assess trade-offs between power, throughput, and "stealth":

**UAV-1** Assess Shadowed Two-Ray Rician fading as a "reasonable" approximation to the narrowband fading of the UAV channels [39], [41], [40].

**UAV-2** Assess Gamma fading for modeling the heavy blockage in the UAV channels [7], [13], [36].

**UAV-3** Incorporate these fading models to estimate network performance for a UAV relay supporting multiple nodes [1], [46], [27], [24].

**UAV-4** Determine the payoff by equipping the UAV with multiple antennas [5].

**UAV-5** Assess network performance between a hovering UAV versus a loitering UAV supporting multiple ground nodes [53]. The loitering could encompass the UAV flying a gradient ascent to maximize network performance while limited to only the relay information on the UAV.

**UAV-6** Extend these urban simulations to model a standoff UAV detecting wireless operations.

**UAV-7** Undertake large-scale simulations in rural scenarios.

The following list organizes the reported propagation models along their radio system performance estimates to conclude this report:

**Channel Bounds:** COST modeling bounds the channel gain of a low-flying UAV using only city statistics. These bounds are useful for a rapid estimate of a link budget but cannot model channel distributions or fading effects. (Section 8).

**Channel Distributions:** Coverage plots encompass the UAV antenna, the UAV height, and the city's geometry (Section 4). The resulting channel distributions produce statistically significant assessments of performance shifts under the assumption that the radios systems perfectly compensate the channel fading (Section 7).

**Time-Varying Channels:** Flying the UAV along a track through either the coverage plots (Section 6) or a loitering pattern (Section 9) tests the radio's adaptation to the fast fading and deep shadowing.

Regardless of the allocation of tasking, all these efforts require specifying the antenna on the UAV, the antennas on the ground receivers, and recognition that tactical link design includes LPI/LPD objectives.

# References


1. Abdi, Ali; Mostafa Kaveh [2000] Comparison of DPSK and MSK Bit Error Rates for $K$ and Rayleigh-Lognormal Fading Distributions, *IEEE Communication Letters*, 4(4).

2. Abdi, A.; W. Lau; M.-S. Alouini; M. Kaveh [2003] A New Simple Model for Land Mobile Satellite Channels: First- and Second-Order Statistics, *IEEE Transactions on Wireless Communications*, 2(3).

3. Abramson, Norman [1963] Bandwidth and Spectra of Phase-and-Frequency-Modulated Waves, *IEEE Transactions on Communications Systems*, 11(4).

4. Al-Ahmadi, Saad & Halim Yanikomeroglu [2010] On the Approximation of the Generalized-$K$ Distribution by a Gamma Distribution for Modeling Composite Fading Channels, *IEEE Transactions on Wireless Communications*, 9(2).

5. Allen, Jeffery C. [2013] MIMO Channel Research 6.2, *Office of Naval Research (ONR) Code 30 C4 Technical Interchange Review*, May 7–9, 2013.

6. Alqudah, Yazan A. [2013] On the performance of Cost 231 Walfisch Ikegami model in deployed 3.5 GHz network, *The International Conference on Technological Advances in Electrical, Electronics and Computer Engineering (TAEECE)*.

7. Atapattu, Saman; Chintha Tellambura; Hai Jiang [2011] A Mixture Gamma Distribution to Model the SNR of Wireless Channels, *IEEE Transactions on Wireless Communications*, 10(12).

8. `http://brahmand.com/news/CoyoteThe-electric-powered-UAV/2975/1/30.html`

9. Beaulieu, Norman C. & Kasun T. Hemachandra [2011] Novel Representations for the Bivariate Rician Distribution, *IEEE Transactions on Communications*, 59(11).

10. Behnad, Aydin; Norman C. Beaulieu; Kasun T. Hemachandra [2012] Correction to "Novel Representations for the Bivariate Rician Distribution", *IEEE Transactions on Communications*, 60(6).

11. Bello, Philip A. [1963] Characterization of Randomly Time-Variant Linear Channels, *IEEE Transactions on Communications Systems*, CS-11, pages 360–393.

12. Bithas, Petros S.; P. Takis Mathiopoulos; Stavros A. Kotsopoulos [2007] Diversity Reception over Generalized-$K$ $(KG)$ Fading Channels, *IEEE Transactions on Wireless Communications*, 6(12).

13. Bithas, Petros S. [2009] Weibull-gamma composite distribution: alternative multipath/shadowing fading model, *Electronics Letters*, 45(14).

14. Correia, Luis M. [2009] A View of the COST 231-Bertoni-Ikegami Model, *Third European Conference on Antennas and Propagation*, 23-27 March 2009.

15. da Costa, Daniel Benevides; José Cândido Silveira Santos Filho; Michel Daoud Yacoub; Gustavo Fraidenraich [2008] Second-Order Statistics of $\eta$-$\mu$ Fading Channels: Theory and Applications, *IEEE Transactions on Wireless Communications*, 7(3).

16. Daly, Michael P. [2012] *Physical-Layer Encryption Using Fixed and Reconfigurable Antennas*, Ph.D Thesis, Electrical Engineering Department, University of Illinois at Urbana-Champaign.

17. Daly, Michael; Jeffery Allen; John Meloling [2021] *UAV Urban Channels Part I: Bottom-Mounted Whip at 500 MHz*, Technical Report 3253, NIWC Pacific, San Diego, CA.

18. Daly, Michael P.; Ontiveros, Marcos; J. Allen; K. Buchanan, Diana Arceo [2015] Measured $2 \times 2$ MIMO UHF Channels in an Urban Environment, *2015 IEEE International Symposium on Antennas and Propagation*, July 19–25, 2015 Vancouver, BC, Canada.

19. Dharmawansa, K. D. P.; R. M. A. P. Rajatheva; K. M. Ahmed [2006] On the Bivariate and Trivariate Rician Distributions, *IEEE Vehicular Technology Conference*, Montreal, Quebec.

20. Garrity, Thomas A. [2015] *Electricity and Magnetism for Mathematicians*, Cambridge University Press, New York, NY.

21. Galgano, Steven M.; Kaushik B. Patel; Eric Schreiber [2013] *EMANE User Manual 0.8.1*, Adjacent Link LLC, 9 Kiser Lane, Bridgewater, NJ 08807.
Rev. 2 cs.itd.nrl.navy.mil/work/emane

22. Goldsmith, Andrea [2005] *Wireless Communications*, Cambridge University Press, New York, NY.

23. Har, Dongsoo; Alix M. Watson; Anthony G. Chadney [1999] Comment on Diffraction Loss of Rooftop-to-Street in COST 231-Walfisch–Ikegami Model, *IEEE Transactions on Vehicular Technology*, 48(5).

24. He Huang, Chaowei Yuan [2017] On the Ergodic Capacity of Composite Fading Channels in Cognitive Radios with the Product of $\kappa$-$\mu$ and $\alpha$-$\mu$ Variates, arXiv:1712.04124 [cs.IT].

25. Kaiser, James F. & Ronald W. Schafer [1980] On the Use of the $I_0$-Sinh Window for Spectrum Analysis, *IEEE Transactions On Acoustics, Speech, and Signal Processing*, ASSP-28(1).

26. Kim, J. C. & E. I. Muehldorf [1995] *Naval Shipboard Communications Systems*, Prentice Hall, Englewood Cliffs, NJ.

27. Kumar, Suman & Sheetal Kalyani [2017] Outage Probability and Rate for $\kappa$-$\mu$ Shadowed Fading in Interference-Limited Scenario, *IEEE Transactions on Wireless Communications*, 16(12).

28. Lopez-Fernandez, J. ; J.F. Paris; E. Martos-Naya [2017] Bivariate Rician Shadowed Fading Model, arXiv:1701.02981v1 [cs.IT].

29. Marhefka, Ronald J. [2002] *Numerical Electromagnetics Code-Basic Scattering Code, (NEC-BSC 4.2) User's Manual*, Department of Electrical Engineering, Ohio State University, Columbus Ohio.

30. Meloling, John H. [1994] *A Caustic-Corrected Uniform Geometrical Theory of Diffractions for Evaluating High-Frequency Electro-Magnetic Fields Near the Cusp of the Caustic Caused by the Curvature of an Edge*, Ph.D Thesis, The Ohio State University.

31. Moreno-Pozas, Laureano; F. Javier Lopez-Martinez; José F. Paris; Eduardo Martos-Naya [2015] The $\kappa$-$\mu$ Shadowed Fading Model: Unifying the $\kappa$-$\mu$ and $\eta$-$\mu$ Distributions, arXiv:1504.05764v1 [cs.IT].

32. Mosley, Caroline [2015] Since Katrina: A Decade of NOAA Hurricane Research, *NOAA Research Communications*, National Oceanic and Atmospheric Administration.

33. Papoulis, A. [1983] *Probability, Random Variables, and Stochastic Processes*, McGraw-Hill, New York, NY.

34. Parsons, J. D. [2000] *Mobile Radio Propagation Channel*, second edition, John Wiley & Sons, New York, NY.

35. Paris, J. F. [2015] Statistical Characterization of $\kappa$-$\nu$ Shadowed Fading, *IEEE Transactions on Vehicular Technology*, 63(2).

36. Peppas, K.P.; G.C. Alexandropoulos; C.K. Datsikas; F.I. Lazarakis [2011] Multivariate Gamma–Gamma Distribution with Exponential Correlation and its Applications in Radio Frequency and Optical Wireless Communications, *IET Microwaves, Antennas & Propagation*, 5(3).

37. Proakis, [1983] *Digital Communications*, third edition, McGraw-Hill Inc., New York, NY.

38. Rajan, Adithya; Cihan Tepedelenlioğlu; Ruochen Zeng [2017] A Unified Approach for Modeling Fading Channels Using Infinitely Divisible Distributions, *IEEE Transactions on Vehicular Technology*, 66(11).

39. Ramirez-Espinosa, Pablo; F. Javier Lopez-Martinez; JoséF. Paris; Michel D. Yacoub; Eduardo Martos-Naya [2017] An Extension of the $\kappa$-$\mu$ Shadowed Fading Model: Statistical Characterization and Applications, `arXiv:1706.09314v1 [cs.IT]`.

40. Reig, Juan & Lorenzo Rubio [2013] Estimation of the Composite Fast Fading and Shadowing Distribution Using the Log-Moments in Wireless Communications, *IEEE Transactions on Wireless Communications*, 12(8).

41. Romero-Jerez, Juan M.; F. Javier Lopez-Martinez; José F. Paris; Andrea J. Goldsmith [2016] The Fluctuating Two-Ray Fading Model: Statistical Characterization and Performance Analysis, `1611.05063v1 [cs.IT]`.

42. Salo, J.; L. Vuokko; H. M. El-Sallabi; P. Vainikainen [2007] An Additive Model as a Physical Basis for Shadow Fading, *IEEE Transactions on Vehicular Technology*, 56.

43. Sams, Howard W. [1977] *Reference Data for Radio Engineers* (Sixth Edition), International Telephone and Telegraph Corporation.

44. Saunders, S. R. & A. Aragón-Zavala [2007] *Antennas and Propagation for Wireless Communication Systems*, second edition, John Wiley & Sons, New York, NY.

45. Simon, M. & M.Alouini [2000] *Digital Communication Over Fading Channels*, Wiley–IEEE Press, New York, NY.

46. P.M. Shankar [2005] Outage Probabilities in Shadowed Fading Channels Using a Compound Statistical Model, *IEE Proc.-Commun.*, 152(6).

47. Stefanovic, Hana; Vladimir Stefanovic; Aleksandra Cvetkovic; Jelena Anastasov; Dimitrije Stefanovic [2008] Some Statistical Characteristics of a New Shadowed Rician Fading Channel Model, *The Fourth International Conference on Wireless and Mobile Communications*, IEEE Computer Society.

48. Stüber, Gordon L. [2001] *Principles of Mobile Communication*, second edition, Kluwer Academic Publishers, Boston, MA.

49. Turin, G. L.; F. D. Clapp; T. L. Johnston; S. B. Fine; D. Lavry, [1972] A Statistical Model of Urban Multipath Propagation, *IEEE Transactions on Vehicular Technology*, 21(1).

50. Wang, Xiao-Dong; Guo-Sheng Rui; Hao-Yu Xu; Zhi-Yong Bu [2007] Delay Spread Statistics in a Two-Path Distributed Antenna System with Gamma-Lognormal Fading Channels, *IEEE Communications Letters*, 11(8).

51. Watterson, C.C.; J.R. Juroshek; W.D. Bensema [1970] Experimental Confirmation of an HF Channel Model, *Proceedings of the IEEE*, 18(6).

52. Yacoub, Michel Daoud [2007] The $\kappa$-$\mu$ Distribution and the $\eta$-$\mu$ Distribution, *IEEE Antennas and Propagation Magazine*, 49(1).

53. Zhang, Shuowen; Yong Zeng; Rui Zhang [2018] Cellular-Enabled UAV Communication: Trajectory Optimization Under Connectivity Constraint, *2018 IEEE International Conference on Communications (ICC)*.